

Nitrotetrazolium Blue Exclusion Assay (NBTx)

Demonstration of a novel assay to quantify
cytochrome *c* oxidase deficiency



Inaugural-Dissertation

zur

Erlangung des Doktorgrades

der Mathematisch-Naturwissenschaftlichen Fakultät

der Universität zu Köln

vorgelegt von

Marie-Lune Simard

aus

Montreal, Kanada

Berichterstatter: Prof. Dr. Jan Riemer
Prof. Dr. Rudolf Wiesner

Tag der mündlichen Prüfung: 5. September 2018

“Science is built up with facts, as a house is with stones. But a collection of facts is no more science than a heap of stones is a house.”

Jules Henri Poincaré

TABLE OF CONTENTS

Abstract.....	ix
Zusammenfassung.....	x
Acknowledgements	xii
List of publications.....	xiv
List of abbreviations.....	xv
INTRODUCTION.....	1
1.1 The origin of the mitochondrion	1
1.2 Mitochondrial structure.....	2
1.3 Mitochondrial genome.....	3
1.4 Mitochondrial function.....	8
1.4.1 Oxidative phosphorylation.....	8
1.4.2 Metabolic pathways within the mitochondria	10
1.4.3 Control of mitochondrial activity	11
1.4.4 Cell signalling pathways and modulation of cellular response	13
1.4.5 Cell death through apoptosis	14
1.5 Mitochondrial diseases	15
1.6 Enzyme histochemistry	20
AIMS OF THIS STUDY.....	23

MATERIALS AND METHODS	24
3.1 Ethics statement	24
3.2 Preparation of incubation media.....	24
3.3 NBTx assay.....	24
3.4 Inhibiting the respiratory chain.....	25
3.5 Mouse tissues.....	26
3.6 Human tissues	26
3.7 Fruit flies, <i>Drosophila melanogaster</i>	26
3.8 Hypoxic conditions	27
3.9 COX/SDH assay.....	27
3.10 Succinate dehydrogenase activity.....	27
3.11 DAB histochemistry	28
3.12 Laser microdissection and quantitative pyrosequencing	28
3.13 Statistical analyses.....	29
3.14 Image acquisition, processing and analysis.....	29
3.15 Quantitative analysis of skeletal muscle	29
RESULTS	30
4.1 Competing biochemical reactions.....	30
4.2 COX-deficient mitochondria in mouse models.....	37
4.3 Quantification of COX deficiencies.....	40
4.4 MtDNA heteroplasmy in heart tissues.....	45
4.5 NBTx assay in the brain	50
4.6 The application of the NBTx assay to study <i>Drosophila melanogaster</i>	60
4.7 NBTx Assay in Human Diagnostics	61
DISCUSSION	64

References.....	68
Appendix.....	79
Appendix A Fiji Macro for NBTx Quantitative Analysis	80
Appendix B Raw Data.....	84
Appendix C NBTx Protocol.....	89
Erklärung.....	94
Curriculum Vitae.....	Error! Bookmark not defined.

Abstract

Respiratory chain impairment, interfering with energy production in the cell, is a major underlying cause of mitochondrial diseases. Yet, the surprising variety of clinical symptoms and the wide gap between ages of onset, as well as the involvement of mitochondrial impairment in ageing and age-related diseases continues to challenge our understanding of the pathogenic processes. The explanation for this complexity likely lays in the multiple roles of mitochondria in cellular function, a unique set of requirements for each cell types, and a convergence of a complex dual genetic predispositions and environmental factors. As the defined gene defect poorly predicts clinical manifestations in humans it remains essential to carefully assess the etiopathology of mitochondrial diseases. Given the heterogeneity of mitochondrial activity in cells and their functional relevance, clarifying the contribution of mitochondrial metabolic dysfunction at the cellular level is fundamental. For this purpose, we developed a novel enzyme histochemical method that enables precise quantification of COX deficiency in fresh-frozen tissues. I demonstrate that the loss of oxidative activity is detected at very low levels – an achievement unequaled by previous techniques and opens up new opportunities for the study of early disease processes or comparative investigations. Moreover, human biopsy samples of several genotypic origins were used and the successful detection of COX-deficient cells suggests a broad application for this new method. Lastly, the assay can be adapted to a wide range of tissues in the mouse and extends to other animal models, illustrated here with the fruit fly, *Drosophila melanogaster*. Overall, the new assay enables the quantification and precise mapping of single cells presenting impaired COX activity with the full extent of COX deficiency in tissues being made visible. This work makes the demonstration that the new enzyme histochemistry assay is a reliable tool for exposing COX-deficient cells and thereby expands new possibilities for future investigation.

Zusammenfassung

Schädigungen der Atmungskette, welche die zelluläre Energiegewinnung beeinträchtigen, sind eine zentrale Ursache mitochondrialer Erkrankungen. Unser Verständnis der zugrundeliegenden pathogenen Prozesse wird jedoch durch die überraschende Vielfalt klinischer Symptome und das unterschiedliche Manifestationsalter mitochondrialer Erkrankungen sowie durch die Beeinträchtigung mitochondrialer Funktionen während des Alterungsprozesses und bei altersbedingten Erkrankungen fortwährend in Frage gestellt. Eine mögliche Erklärung für die Komplexität mitochondrialer Erkrankungen liegt möglicherweise in den vielfältigen Aufgaben der Mitochondrien und den einzigartigen metabolischen Anforderungen bestimmter Zelltypen begründet. Des Weiteren spielt vermutlich das Zusammenspiel von genetischen Faktoren zweier Genome, bestimmten Prädispositionen und Umweltfaktoren eine Rolle. Da genetische Defekte klinische Manifestationen im Menschen nur bedingt prognostizieren, ist es von zentraler Bedeutung, den Krankheitsverlauf mitochondrialer Erkrankungen sorgfältig einzuschätzen und zu beurteilen. Da die Aktivität der Mitochondrien und deren funktionelle Bedeutung abhängig vom Zelltyp sehr heterogen ist, ist es von fundamentalem Interesse, das Ausmaß einer mitochondrialen metabolischen Dysfunktion auf zellulärer Ebene aufzuklären. Aus diesem Grund haben wir eine neuartige enzymhistochemische Methode entwickelt, die eine präzise Quantifizierung der COX-Defizienz in frischeingefrorenen Geweben ermöglicht. Der Verlust der oxidativen Aktivität kann dabei bereits bei einem geringen Schweregrad nachgewiesen werden – die hier beschriebene Sensitivität der Methode übertrifft alle bisher beschriebenen Techniken und eröffnet neue Möglichkeiten, die frühen Stadien mitochondrialer Erkrankungen zu analysieren und vergleichende Untersuchungen zu machen. Darüber hinaus wurden humane Biopsien unterschiedlicher genotypischer Herkunft untersucht und die erfolgreiche Detektion COX-defizienter Zellen weist auf eine breite Anwendungsmöglichkeit dieser neuartigen Methode hin. Zusätzlich dazu kann diese

Methode für eine Reihe unterschiedlicher Gewebe angepasst werden und auch in anderen Tiermodellen, wie hier in der Fruchtfliege *Drosophila melanogaster* gezeigt, angewendet werden. Insgesamt gesehen ermöglicht diese neue Färbemethode die genaue Quantifizierung und die präzise Zuordnung einzelner COX-defizienter Zellen und macht somit das volle Ausmaß der COX-Defizienz im Gewebe sichtbar. Diese Arbeit demonstriert, dass die hier beschriebene neue enzymhistochemische Färbemethode eine verlässliche Technik darstellt, um COX-defiziente Zellen mit hoher Sensitivität zu identifizieren und bietet somit neue Anwendungsmöglichkeiten für zukünftige Analysen.

Acknowledgements

Firstly, I would like to express my sincere gratitude to my supervisor Dr. James B. Stewart for his support and encouragements. It was mere chance and happy coincidences that brought us to work together in Cologne but it was through his trust and his unusual laissez-faire philosophy that I was able to seize this exciting project and make it my own. Thank you, Jim, for the long and passionate talks, for your knowledge, which you generously shared with me, and for pushing me to take my time and stay critical. With all the nuances and flaws that we are made of, I could not have imagined a better suited, more supportive supervisor for my PhD study.

A very special gratitude goes to Dr. Arnaud Mourier who offered his support from the first observation I made and all the way to the end of this project. His general enthusiasm was contagious and very energizing. I am thankful for his knowledge of the mitochondrial biochemistry which has been indispensable, and his supervision throughout.

I was privileged to be invited to try my new method on human biopsy samples and for this I would like to acknowledge the generosity of Dr. Laura C. Greaves and Prof. Robert W. Taylor at the Wellcome Center for Mitochondrial Research, in Newcastle University. I would like to thank them for their continuing support and valuable contribution to the peer reviewed publication. I am also very grateful for the technical help I received while in Newcastle and later on, when extra images of human tissues were needed to complete the project. I thank in particular Gavin Falkous and Anna Smith for technical assistance with obtaining the histochemical images of human tissue sections.

I would also like to thank the members of my thesis committee: Prof. Rudolf Wiesner and Prof. Jan Riemer who offered guidance and support during my studies. I am grateful for the time they gave me and for the valuable advice I received. The lab members of Prof. Wiesner should also be mentioned as they have greatly contributed

to the exploration and adaptation of the NBTx assay to brain and skin tissue. Special thanks to Kai Faehrmann, Konrad Ricke and Oliver Baris.

Many thanks as well to the group of Nils-Göran Larsson at the Max Planck Institute with whom I was lucky to share all of the common lab space. The NGL lab contributed in many ways to enrich my environment throughout my PhD. I am very grateful to Timo Kauppila and Ana Bratic who helped me with the fly work. Also, a shout-out to my office team: Min, Sara, Johanna and Timo with whom I could always have a good discussion.

This work was made possible by the generous accessibility to leading edge equipment and valuable technical support of the FACS & Imaging Core Facility at the Max Planck Institute for Biology of Ageing as well as the CECAD Imaging Facility (University of Cologne, Cluster of Excellence in Ageing Research). In addition, I would like to acknowledge the contribution of Peter Zentis from the CECAD Imaging Facility for the Fiji macro which enabled all of the quantitative analysis.

A very special thank should also go to Sara and Marita who have been there during the ups and downs and did not hesitate to offer me a hand when I needed. I will always smile at the thought of our burger and caipirinha's night; thank you for opening up and being yourselves!

And finally a special mention to my children, Emma and Miriam, who will certainly remember those days when I sat in the living room and worked my way through this PhD thesis. Thank you for quietly falling asleep on the couch and letting me work a little longer! You give me endless joy and because of you I found the courage to be that person that I want to be.

List of Publications

PART OF THIS WORK WAS ORIGINALLY PUBLISHED ONLINE IN WILEY ONLINE LIBRARY;
THE JOURNAL OF PATHOLOGY, 2018 WITH AN OPEN ACCESS AGREEMENT:

Simard M.L., Mourier A., Greaves L.C., Taylor R.W., Stewart J.B., 2018. A novel histochemistry assay to assess and quantify focal cytochrome *c* oxidase deficiency. *The Journal of Pathology.*, 245(3), pp.311-323.

OTHER PUBLICATIONS RELEVANT TO THIS WORK:

Gammage P.A., Viscomi C., **Simard M.L.**, Costa A.S.H., Gaude E., Powell C.A., Van Haute L., McCann B.J., Zhang L., Rebar E.J., Larsson N.G., Zeviani M., Frezza C., Stewart J.B., Minczuk M., 2018. Genome editing in mitochondria corrects a pathogenic mtDNA mutation *in vivo*. *Nature Medicine*, DOI: 10.1038/s41591-018-0165-9.

Kaupila J.H.K., Baines H.L., Bratic A., **Simard M.L.**, Freyer C., Mourier A., Stamp C., Filograna R., Larsson N.G., Greaves L.C., Stewart J.B., 2016. A phenotype-driven approach to generate mouse models with pathogenic mtDNA mutations causing mitochondrial disease. *Cell Reports*, 16, pp.2980-2990.

Matic S., Jiang M., Nicholls T.J., Uhler J.P., Dirksen-Schwanenland C., Polosa P.L., **Simard M.L.**, Li X., Atanassov I., Rackham O., Filipovska A., Stewart J.B., Falkenberg M., Larsson N.G., Milenkovic D., 2018. Mice lacking the mitochondrial exonuclease MGME1 accumulate mtDNA deletions without developing progeria. *Nature Communications*, 9, p.1202.

List of Abbreviations

AAV	Adeno-associated virus
ADP	Adenosine diphosphate
ALA	Alanine
AMP	Adenosine monophosphate
AMPK	AMP kinase
ATP	Adenosine triphosphate
ATP6, ATP8	ATP synthase F0 subunit 6 and 8
Ca ²⁺	Calcium ion
CO1, CO2, CO3	Cytochrome c oxidase subunit I, II, III
COX	Cytochrome c oxidase
CYTB	Cytochrome b
DAB	3-3' diaminobenzidine
DNA	Deoxyribonucleic acid
DOA	Dominant optic atrophy
Drp1	Dynamin-related protein 1
ETC	Electron transport chain
FAD	Flavin adenine dinucleotide
FADH	Reduced FAD
GTP	Guanosine triphosphate
H ⁺	Hydron
HCl	Hydrogen chloride
HS	Heavy strand
HSP	HS promoter
IM	Inner membrane
IMS	Intermembrane space
LECA	Last eukaryotic common ancestor
LH	Light strand
LHON	Leber hereditary optic neuropathy
Lrp _{prc}	Leucine-rich pentatricopeptide repeat containing protein
LSP	LS promoter
M	Matrix
MCU	Mitochondrial calcium uniporter
Mfn 1, 2	Mitofusin 1 and 2
mNCX	Mitochondrial Na ⁺ /Ca ²⁺ exchanger
mtDNA	Mitochondrial DNA
mtZFN	Mitochondrial zinc finger nuclease

List of Abbreviations

Na ⁺	Sodium ion
NAD	Nicotinamide adenine dinucleotide
NADH	Reduced NAD
NaOH	Sodium hydroxide
NBT	Nitrotetrazolium blue chloride
NBTx	Nitrotetrazolium blue exclusion assay
NCR	Non-coding region
ND1-4, 4L, 5, 6	NADH dehydrogenase subunit 1-4, 4L, 5, 6
OD	Optical density
OM	Outer membrane
OPA-1	Optic atrophy 1
OriH	Origin of replication, heavy strand
OriL	Origin of replication, light strand
OXPHOS	Oxidative phosphorylation
PBS	Phosphate-buffered saline
PCR	Polymerase chain reaction
Pi	Inorganic phosphate
PMS	Phenazine methosulfate
RNA	Ribonucleic acid
rRNA	Ribosomal RNA
SDH	Succinate dehydrogenase
TCA	Tricarboxylic acid
Tfam	Mitochondrial transcription factor A
tRNA	Transfer RNA
TTFA	Thenoyltrifluoroacetone

Nitrotetrazolium Blue Exclusion Assay (NBTx)

INTRODUCTION

1.1 The origin of the mitochondrion

The endosymbiosis event of an oxygen consuming bacteria inside a primitive eukaryote cell was a defining event in the history of life as we know it today (Sagan 1967; Koonin 2010; O'Malley 2015). The small organelle known as the mitochondrion (plural: mitochondria) was once, billions of years ago, a free-living bacteria. The endosymbiosis idea took roots in the early observations of this organelle through the lens of a microscope as its resemblance to bacteria – rod-shaped structures with a double membrane –captured attention (Ernster & Schatz 1981). But it was through the discovery of small circular DNA inside the organelle that ultimately led the way to ascertain its bacterial ancestral origin (Nass & Nass 1963; Gray 2012).

Through the development of DNA isolation methods and more advanced sequencing techniques, mitochondrial DNA (mtDNA) fragments from eukaryotes were aligned to sequences across all three domains of life (bacteria, archaea and eukaryota); mtDNA matches most closely the phylogenetic group of the α -proteobacteria genome, whereas the nuclear genome traces back to the archaea (Martin 2005; Gray 2012; Gray 1999; Cedergren et al. 1988). Although the exact process by which eukaryotic cells have evolved and acquired the features observed today is still a matter of debate (Gray et al. 2001; Gray 2017; Martin et al. 2015), it is fairly accepted that the endosymbiosis of proteobacteria has enabled the last eukaryotic common ancestor (LECA) to develop both in size and in complexity; an evolutionary breakthrough attributable to the increase in energy resources conveyed by the mitochondria (Lane & Martin 2010). In mammals, it is estimated that more than 90% of cellular adenosine triphosphate (ATP) is produced by aerobic respiration in the mitochondria, a process known as the oxidative phosphorylation (OXPHOS) pathway.

1.2 *Mitochondrial structure*

Mitochondria are found in multiple copies within the cytoplasm of eukaryotic cells, enclosed by an outer and inner membrane. The outer membrane is porous to ions diffusion and small uncharged molecules easily enter through porin channels. On the other hand, the inner membrane is impermeable and many times folded, forming mitochondrial cristae, and isolating the matrix; the inner most compartment of the mitochondria (**Figure 1.1**). The distinct areas provide the structural support for the coordination and regulation of several enzymatic reactions that define mitochondrial function (Green & Beinert 1955). Protein translocases on both membranes ensure the distribution of proteins assembled in the cytosol to be sorted within the right compartments of the mitochondria.

Contrary to the porous nature of the outer membrane, the inner membrane selectively transports ions and protons across, thereby maintaining an electrochemical membrane potential of ~ 180 mV. This membrane potential is the result of coordinated efforts from specialized ion channels as well as from the movement of electrons and protons through the electron transport chain (ETC): a group of 4 complexes composed of reducing and oxidizing enzymes and electron carrying proteins such as heme- and flavo- proteins (reviewed in O'Rourke 2007). This highly controlled flux of ions is fundamental for mitochondrial response to energy demands and for ATP generation through the use of the proton-motive force by the ATP synthase. In the mitochondrial inner most compartment (the matrix), important enzymatic reactions take place, such as the tricarboxylic acid (TCA) cycle, fatty acid β -oxidation, steroids synthesis and the urea cycle. Furthermore, the matrix is home to the mitochondrial genome - packed in small nucleoli - and is the site of mtDNA transcription, replication and translation.

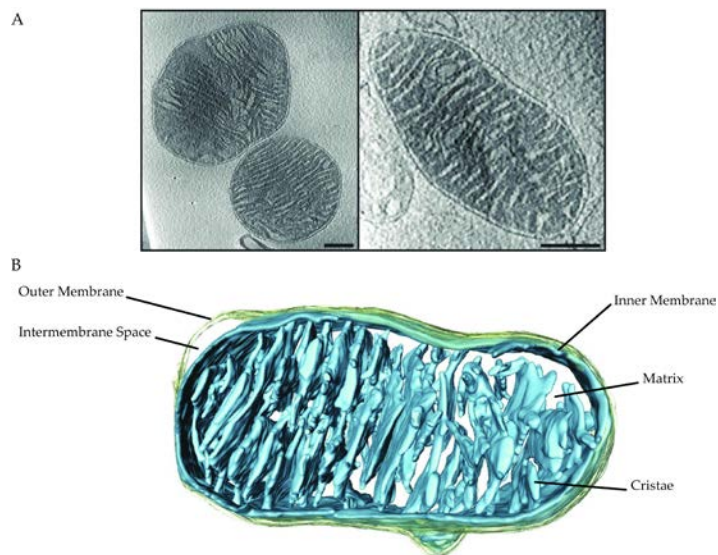


Figure 1.1 | The mitochondrion and its structure. **(A)** Electron cryotomography showing mitochondria in heart tissue of young (20 weeks) mice. **(B)** 3D reconstruction of typical heart mitochondria in mice. Outer membrane is shown in yellow and the inner membrane and cristae in blue. Scale bars, 250 nm. Image adapted from Brandt et al. 2017, eLife (Open Access).

1.3 Mitochondrial genome

The mitochondrial genome universally encodes for proteins necessary for mitochondrial function. Proteins encoded within the animal mtDNA consist of subunits of the electron transport chain (Complex I, II, III and IV) as well as Complex V (ATP synthase). The translational components are also partly found in the mtDNA, namely ribosomal RNAs (rRNAs, 12S and 16S subunits), sometimes also the 5S rRNA, as well as complete or partial set of transfer RNAs (tRNAs) (Gustafsson et al. 2016; Gray 2012). Despite similarities across species, sequence analysis of full mitochondrial genome from diverse organisms has revealed that there exist a notable variability in size, gene content and arrangement across eukaryotes (reviewed in Gray et al. 1999). Mitochondrial genome size can be as small as 6 kilobase pairs (kbp) in the human malaria parasite (*Plasmodium falciparum*) or up to more than 200 kbp in a plant (*Arabidopsis thaliana*). In humans, as well as other mammals such as the common laboratory mouse *Mus musculus*, the circular double stranded mtDNA is ~ 16-17 kbp and encodes 37 genes

which consist of 13 proteins (polypeptides), 2 rRNAs (small and large subunit) and 22 tRNAs (**Figure 1.2**). Under the control of the nucleus are more than 1000 additional proteins which make up the mitochondrial proteome (Calvo et al. 2016) - among them are proteins of the respiratory chains, regulatory proteins involved in mtDNA transcription and maintenance and part of the translation machinery such as ribosomal proteins (reviewed in Gustafsson et al. 2016). It is unclear why primarily genes encoding for the OXPHOS system have been retained in the organellar genome along with rRNAs and tRNAs. It is speculated that a local control of gene expression could be linked to changes in membrane potential and/or redox state and act as regulatory mechanism for metabolic needs (Allen 2015). The reasons for mitochondrial genome differences across species and the evolutionary driving force which led to gene loss or gene transfer to the nucleus remain unclear.

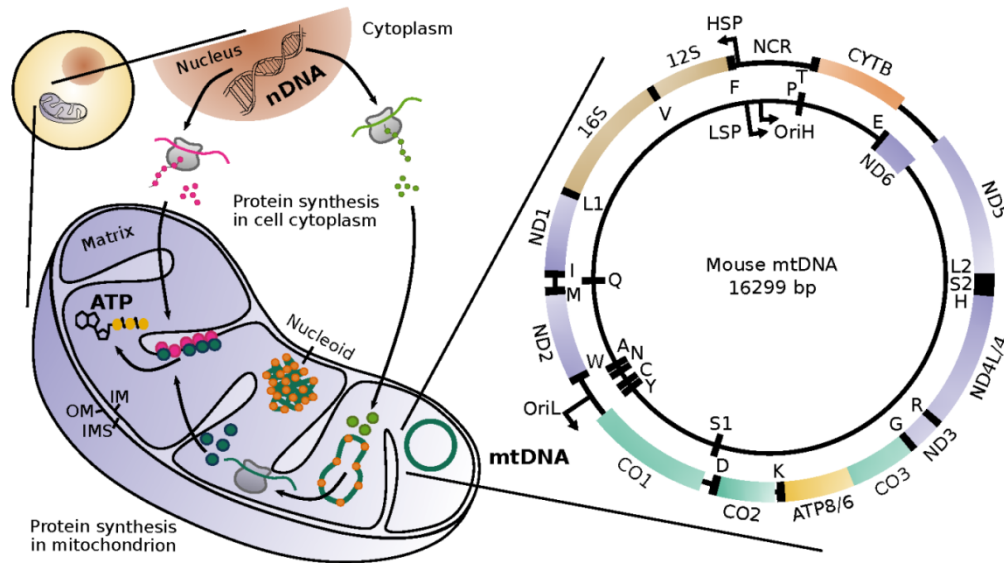


Figure 1.2 | Illustration of the dual genome regulation of mitochondrial protein synthesis and the mouse mtDNA organization. Most mitochondrial proteins are encoded in the nucleus and are synthesized in the cytoplasm, subsequently imported inside the mitochondria (mitochondrial outer membrane (OM), inner membrane (IM) and intermembrane space (IMS)). A Schematic representation of the double-stranded mtDNA molecule showing the heavy strand (HS) and light strand (LS), the origin of replication (OriH, OriL), two promoters (HSP, HSL) and the non-coding region (NCR). Genes are represented by colored rectangles including 22 tRNA genes (black rectangle, each tRNA is identified with a corresponding capital letter), 2 rRNAs (12S, 16S) and 13 mRNAs (CYTB, cytochrome b; CO1-3, cytochrome c oxidase subunit I-III; ND1-4, 4L, 5-6, NADH dehydrogenase subunit 1-4, 4L, 5-6; ATP6 and 8, ATP synthase F0 subunit 6 and 8). Illustration used with permission from Isokallio, M., 2017. The source and fate of mitochondrial DNA mutations using high-sensitivity next-generation sequencing technologies. (PhD Dissertation), Retrieved from Universitäts- und Stadtbibliothek Köln.

Genes encoding for proteins necessary for mitochondrial function are therefore found on either the mitochondrial or the nuclear genome and spread across several chromosomes, including the X chromosome. A particularity of the mitochondrial genome is that, unlike the nuclear DNA who is confined in the nucleus with two copies of each gene compacted into chromosomes, multiple copies of mtDNA reside within a mitochondrion (2-10 mtDNA molecules, depending on the type of cell or tissue) and several hundreds of mitochondria are found within each mammalian cell (Boghenagen

& Clayton 1974). This impressive amount of mtDNA within a given cell enables mutations and sequence variations to be tolerated given that a certain threshold for energy production is not reached. Phenotypic expression of mitochondrial disease caused by mtDNA defect depends on the proportion of mutated mtDNA to the amount of wild-type mtDNA within a cell and segregation of mutant mtDNA across tissues partially explains the variation in clinical features typically observed in mitochondrial diseases (Turnbull & Rustin 2016). The term homoplasmy refers to cells or tissues where nearly all mtDNA molecules are identical, whereas heteroplasmy describes a situation where more than one mtDNA variant, which usually contains a deletion or a point mutation, is found within one organism (Larsson & Clayton 1995). Homoplasmic mtDNA deletions or point mutations that drastically impair the electron transport chain or the ATP synthase are embryonic lethal but at a low heteroplasmy level the mutated mtDNA molecules remain in the pedigree of families with asymptomatic individuals until a critical threshold is reached. Because of the biological mechanisms defining mtDNA inheritance, heteroplasmy levels can change drastically between generations. In addition, every offspring of a mother carrying low levels of a heteroplasmic mutation will inherit the mutant mtDNA with an unpredictable variation in heteroplasmy levels between siblings (Taylor & Turnbull 2005).

Inheritance of mitochondrial genome is normally strictly maternal; mitochondria from sperm are greatly outnumbered by the oocyte mitochondrial content and quickly eliminated after fecundation (Sato & Sato 2013). The term mitochondrial genetic bottleneck was given to the process by which segregation of mutated mtDNA randomly occurs during oogenesis giving rise to offspring with different load of mutant mtDNA (Laipis et al. 1988; Brown et al. 2001; Upholt & Dawid 1977; Olivo et al. 1983). Germline cells develop into mature oocytes that contain an impressive amount of mitochondria per cell – on average approximately 100,000 mitochondria are found in human oocytes (Chen et al. 1995) – but it was shown that primordial germ cells first divide into primary oocytes without mitochondrial biogenesis, thereby reducing the total amount of

mitochondria per cell and randomly distributing mutant and wild-type mtDNA molecules between immature oocytes (Wai et al. 2008, **Figure 1.3**).

The complexity of mitochondrial genetic and the dual genetic control of mitochondrial functions are important fields of research which aim to better predict clinical outcome, to estimate the risk of maternal transmission of pathologic mtDNA mutation, and developing efficient treatment strategies.

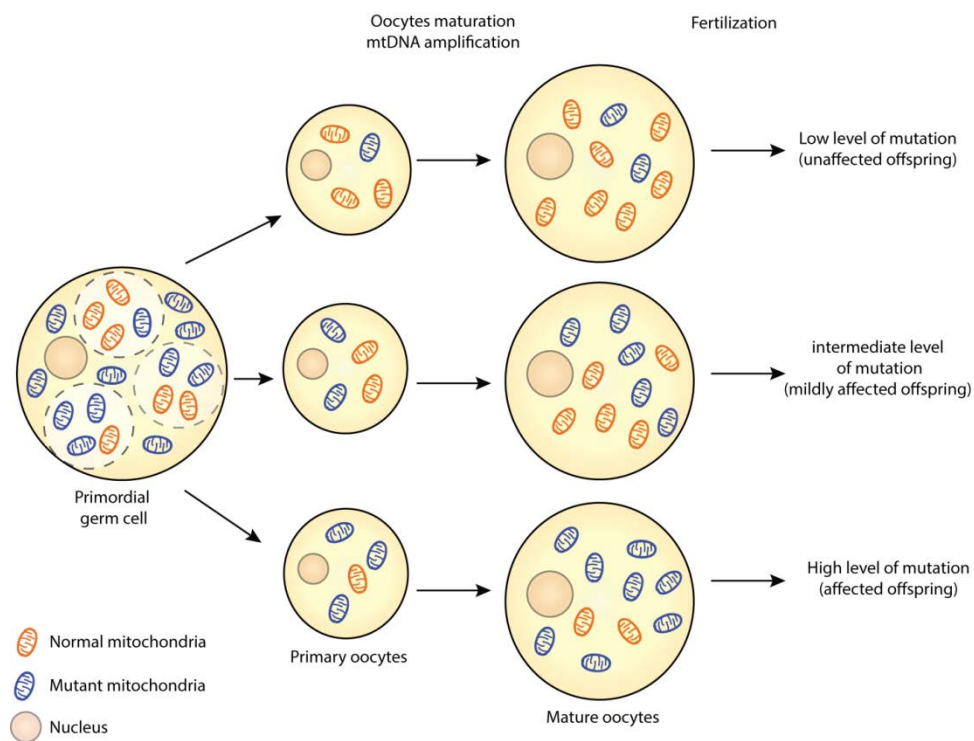


Figure 1.3 | Oocyte development and the bottleneck effect. Primordial germ cells divide in smaller primary oocytes where only a fraction of the mitochondria are randomly distributed, creating what is known as the bottleneck effect. This causes an unpredictable segregation of mutant mtDNA per oocyte and explains the variation in mutational load between generations and among offspring of a mother carrying low levels of pathogenic mtDNA mutations. Illustration adapted by permission from RightsLink Permissions Springer Customer Service Center GmbH: Springer Nature, Nature Reviews Genetics, (Mitochondrial DNA mutations in human disease, Taylor and Turnbull), COPYRIGHT, 2005.

1.4 Mitochondrial function

Mitochondria are an integral part of eukaryote cells and as such are essential participants in several of the cell basic functions. Predominantly, mitochondria are specialized energy producing organelles (in the form of ATP molecules) but their role expands beyond that of ATP production to a more intricate coordination of basic cellular function. Mitochondria are involved in cell cycle events, cell signalling pathways, modulation of cellular response, regulation of metabolism and cell death through apoptosis (reviewed in Kasahara & Scorrano 2014; McBride et al. 2006).

1.4.1 Oxidative phosphorylation

Energy production in the form of ATP molecules is tightly regulated within the inner membrane of the mitochondria. The OXPHOS pathway is composed of enzymes within the inner membrane which effectively move protons (hydrogen atoms, H^+) across and transfer electrons in a series of redox reaction ending with the reduction of oxygen to water molecules. The accumulation of protons in the intermembrane space creates a pH gradient and an electrical potential which drives the ATP synthase activity (Complex V). The mitochondrial respiratory chain produces the majority of ATP molecule; only a small fraction comes from anaerobic glycolysis in the cell cytoplasm. The electron transport chain takes place in four distinct complexes: Complex I, nicotinamide adenine dinucleotide (NADH) dehydrogenase; Complex II, succinate dehydrogenase, SDH; Complex III, cytochrome bc_1 complex and Complex IV, cytochrome c oxidase, COX (**Figure 1.4**). Being at the center of mitochondrial metabolic activity, the discovery of those enzymes in the 1950s and subsequent investigation regarding their biological function is relevant to this work. Understanding the complex redox activity associated with enzymes within the electron transport chain has enabled histochemistry assays to be developed allowing researchers to specifically assess focal mitochondrial enzyme dysfunction in diseased tissue. Since respiratory chain complexes are assembled in the mitochondria from proteins encoded in both the nuclear genes and the mtDNA itself,

with the exception of Complex II which genes are found exclusively in the nuclear DNA, dysfunctional enzymatic activity in the mitochondria can be detected regardless if the problem is of nuclear or mitochondrial DNA in origin.

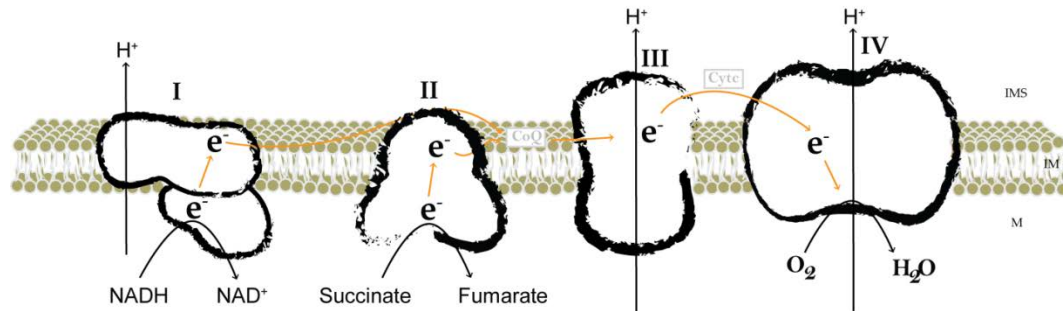


Figure 1.4 | Electron transport chain. A simplified view of the electron transport chain within the inner membrane bilayer, showing the 4 enzyme complexes with the flow of electrons and protons. Complex I, II, III and IV are marked with roman numbers respectively. CoQ, coenzyme Q; Cyt c, cytochrome c; e^- , electron; H^+ , proton; IMS, intermembrane space; IM, inner membrane; M, matrix.

The major source of electron entry into the respiratory chain is through removal of hydrogen from NADH by Complex I, resulting in proton translocation across the inner membrane and electron transfer to the membrane-bound ubiquinone molecule. Another source of electrons is through the enzymatic activity of Complex II: succinate which is generated within the citric cycle is stripped of two hydrogen atoms to form fumarate with the resulting reduction of flavin adenine dinucleotide (FAD) into $FADH_2$ and subsequently the reduction of ubiquinone. Reduced ubiquinone move electrons to Complex III where cytochrome c serves as the next electron acceptor in the chain. Complex IV terminates the electron transfer with the oxidation of cytochrome c, proton translocation and reduction of oxygen to water molecules. Finally, the electrochemical gradient generated is used by the ATP synthase (Complex V) to generate ATP from adenosine diphosphate (ADP) and inorganic phosphate (Pi). Protons pass through a channel formed by 2 main subunits: F_0 , a hydrophobic octameric protein complex and F_1 , a hydrophilic subunit rotating upon the passage of protons (the proton-motive force)

thereby catalyzing the production of ATP (Reviewed in Junge & Nelson 2015; Yoshida et al. 2001, **Figure 1.5**).

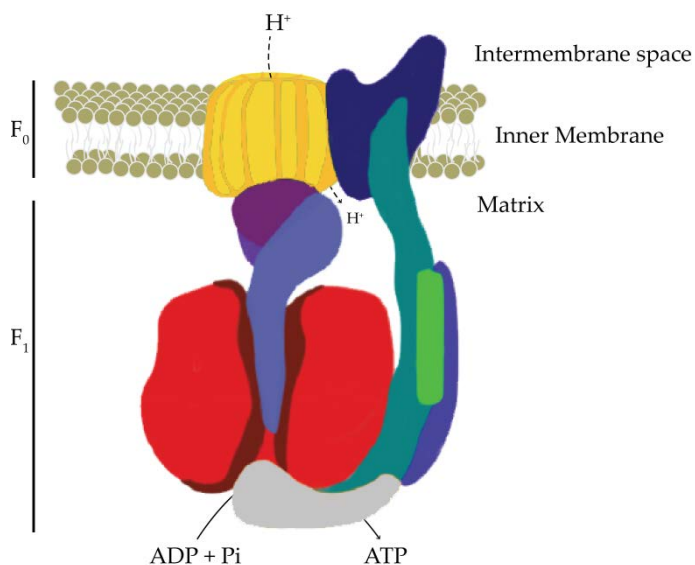


Figure 1.5 | Illustration of the mammalian ATP synthase. The ATP synthase is composed of several subunits together forming a hydrophobic (F₀) part, embedded in the mitochondrial inner membrane, and a hydrophilic (F₁) multisubunit complex. On the passage of protons through the barrel-shaped F₀ subunit (dashed arrows), a mechanical rotation of the F₀ subunit (shown with a black arrow) provides the energy for ATP synthesis within the F₁ subunit. Image adapted from Antoniel et al 2014, International Journal of Molecular Sciences (Open Access).

1.4.2 Metabolic pathways within the mitochondria

The OXPHOS system described above is central to mitochondrial function but is not the only metabolic activity attributed to this organelle. Indeed, mitochondria are also the site of other key metabolic events such as production of reducing equivalents by the TCA cycle, steroid synthesis – in mitochondria of specific cells of the adrenal glands, the gonads and the kidney (Miller 2013) – gluconeogenesis and ketone bodies in the liver, as well as the urea cycle and amino acid synthesis. In addition, fatty acid β -oxidation which ultimately feeds into the OXPHOS system and contributes to a high yield of ATP production takes place within the mitochondrial matrix. The importance of fatty acid-oxidizing metabolism is exemplified by human diseases associated with defect in either

transport of fatty acid into the mitochondria or defects in β -oxidation (Vishwanath 2016). Fatty acids are taken up into the mitochondria and metabolized through repetitive 4 step enzymatic reactions (dehydrogenation, hydratation, a second dehydrogenation step and finally thiolytic cleavage), the process ends when the chain of carbon atoms has been fully cleaved into several molecules of acetyl-CoA. In the mitochondria of the liver, acetyl-CoA does not enter the TCA cycle but is used for the synthesis of ketone bodies; another important source of alternative energy for many organs, particularly for the brain (Rinaldo et al. 2002).

1.4.3 *Control of mitochondrial activity*

Overall, metabolic events taking place in the mitochondria are unequivocally interlaced with that of the cell and have an incredible adaptability and responsivity to cellular demands. Given its structure, this feature seems coherent; mitochondria are built with an isolating double membrane equipped with several ion channels (as well as numerous exchangers and pumps), it contains specialized enzymes and a small genome, including its own transcription machinery. The details of the molecular pathways and biochemical events by which cellular metabolic demands are translated into a mitochondrial response are still largely unknown.

Nevertheless, advancing research on the topic shows that mitochondrial activity is controlled through the convergence of distinct regulatory mechanisms that include: substrate limitation for ATP production (ADP and phosphate concentration), mitochondrial calcium concentration, tissue specific or developmental expression of isozymes, allosteric control (expression of small proteins affecting OXPHOS enzyme kinetics) and cell signalling induced phosphorylation and dephosphorylation of OXPHOS components. In addition, mitochondria form a network that dynamically reshapes itself upon fusion or fission events. Described as an integrated reticulum this reshaping of the mitochondrial architecture is thought to serve as a way for mitochondrial quality control as well as being part of the complex orchestration of

mitochondrial metabolism modulation (Shutt & McBride 2013; Scalettar et al. 1991). The equilibrium between the fused or fragmented state has been shown to correspond to cellular energetic state. For example, mitochondria will fragment when apoptosis signals are triggered (Liu et al. 1996) or will fuse and elongate during starvation (Gomes et al. 2011). Furthermore, properly coordinated mitochondrial dynamic has been associated with successful progress of cellular events such as cell division (Kianian & Kianian 2014), immune responses (Rambold & Pearce 2017) and tissue differentiation and development (Chen et al. 2003). The machinery behind fusion and fission include guanosine-5'-triphosphate (GTP)-dependent proteins, the mitofusin 1 and 2 (Mfn1 and Mfn2 located on the outer membrane) and optic atrophy 1 (OPA-1, located in the inner membrane) and the GTPase dynamin-related protein 1 (Drp1) which forms ring-like structure around the mitochondrial outer membrane and cause fragmentation (reviewed in Liesa et al. 2009). Several more genes involved in mitochondrial dynamic or its regulation have been identified or remain to be found but the last decade of research in the field has certainly exposed the crucial role of mitochondrial dynamic in cellular functions and health. Most of the pioneer work has been done on yeast or cell culture which begs the question as to how mitochondrial dynamic shapes tissue function in human or mouse tissues and what is the relevance of this in terms of the physiopathology of mitochondrial diseases. In physiological conditions, fusion and fission events take place to maintain a stable mitochondrial network that is adaptive to cellular demands. Human mitochondrial diseases such as axonal Charcot-Marie-Tooth and Dominant optic atrophy (DOA) are examples of the dire consequences of gene mutations that affect mitochondrial dynamic (Cohn et al. 2007; Kijima et al. 2005). Depending on the cell type, the mitochondrial network requires more or less motility and adaptability, making certain subsets of cells more susceptible to mitochondrial dysfunction. For example, neuronal cells have high energy demands – consumes around 20% of oxygen at rest - and critically rely on mitochondrial OXPHOS metabolism (Kann & Kovács 2007). Mitochondria dynamically position themselves at sites of high neuronal activity where mitochondrial calcium buffering and ATP production contributes to

support neuronal activity and some form of synaptic plasticity (Kann et al. 2003; Tang & Zucker 1997); the reliance of neuronal cells on mitochondrial motility to sustain complex signalling patterns might provide one explanation for the vulnerability of certain neuronal network to mitochondrial dysfunction.

1.4.4 Cell signalling pathways and modulation of cellular response

Mitochondria are strongly implicated in cell signalling events but our knowledge of this crucial interaction is still incomplete. What we know so far is that mitochondria are not just recipients of cellular signals which command mitochondrial activity to fulfill cellular requirements but rather, there exists a level of greater complexity which position mitochondria as active modulators of cellular functions. The ubiquitous organelles occupy part of the cytosol and with fusion and fission dynamically remodeling the network, mitochondria integrate cellular signal and influence their outcome. This is true for cell cycle events which have been shown to come to a halt under low energy conditions – an outcome of a stop signal coming from the mitochondrial network. Cell division is initiated by external signals and requires sufficient nutrients and available ATP to synthesize protein and double in size. Glucose availability has been shown to be an intermediate “checkpoint” (Jones et al. 2005) which low level will be translated in the mitochondria by the activation of adenosine monophosphate (AMP)-activated protein kinase (AMPK) and reversibly interrupt the initiation of cell division. The active form of AMPK induces the phosphorylation of p53, a transcription factor that act on several genes which regulate cell cycle arrest, cellular senescence and apoptosis (Harris & Levine 2005).

The mitochondria are also contributing to the shape and intensity of signalling pathways through their ability to uptake and release calcium ions (Ca^{2+}). The calcium uptake capacity of mitochondria has been discovered very early on, even before the OXPHOS system (Rizzuto et al. 2012). It is constituted primarily of the mitochondrial Ca^{2+} uniporter (MCU) that selectively permits a rapid flow of calcium ions inside the

matrix and slower $\text{Na}^+/\text{Ca}^{2+}$ exchangers (mNCX) which returns Ca^{2+} to the cytosol. Increase in cellular Ca^{2+} concentration engages a wide range of cellular events and cells spend a considerable amount of energy maintaining low cytosol Ca^{2+} concentration – in the nanomolar range inside the cell compared to millimolar concentrations in the extracellular space – (reviewed in Clapham 2007). Increasing intracellular Ca^{2+} concentration is readily used by cells to trigger all sorts of events: neurotransmitter release, muscle contraction or cellular motility, and modulation of gene expression, cell growth and apoptosis. Interestingly, Ca^{2+} signalling is very variable; through different means of regulation, intracellular changes in Ca^{2+} concentration produces a spectrum of outcomes which lead sometimes to opposite changes in the same cell. For example, long-term potentiation and long-term depression in neurons are two opposing consequences observed in certain neuronal circuit following a transient increase in intracellular Ca^{2+} . It was shown that the difference lies merely in the timing and duration of Ca^{2+} influx (Yang et al. 1999, reviewed in Burgoyne 2007). Others have also demonstrated the effect of oscillation of intracellular Ca^{2+} changes in gene expression and on the redox state of the mitochondria (Hajnóczky et al. 1995; Dolmetsch et al. 1998). Mitochondria are not the main Ca^{2+} -storage organelles, in fact, the endo/sarcoplasmic reticulum, the golgi apparatus, endosomes/lysosomes and secretory vesicles are stronger contributors to calcium homeostasis but in terms of fine tuning signal transduction where spatial distribution and temporal regulation of cytosolic Ca^{2+} transients has been shown to play a crucial role, the Ca^{2+} buffering capacity of mitochondria is relevant to cellular function. Mitochondrial Ca^{2+} uptake plays a role in neuronal plasticity, for example in post-tetanic potentiation (Yang et al. 1999; Yang et al. 2003), or in segregating Ca^{2+} diffusion in polarized cells such as the pancreatic acinar cells (Tinel 1999).

1.4.5 *Cell death through apoptosis*

Another well-known function of mitochondria is its role in apoptosis. Apoptosis is an internal cell death program essential in multicellular organism for proper embryonic development but also eliminates old or damaged cells in adults (tissue homeostasis) and

is initiated as part of the immune defense system to destroy compromised cells (reviewed in Wang and Youle 2009). The central role of mitochondria in cell death by apoptosis established itself in the mid 1990's when both proapoptotic and antiapoptotic proteins were found to reside or localize upon activation on the mitochondria and with the notable discovery that cytochrome c release is a key event in the activation of caspases (Liu et al. 1996; Zamzami et al. 1996). Internal signals such as DNA damage or prolonged nutrient starvation lead to activation of proapoptotic proteins (e.g.: Bax and Bak) and inhibition of antiapoptotic Bcl-2 family proteins ultimately causing the permeabilization of the mitochondrial inner membrane, the loss of the electrochemical gradient and the release of cytochrome c in the cytosol. Apoptosis is tightly regulated in the cell and a decrease or increase in apoptosis can lead to diseases such as cancer, autoimmune diseases or neurodegenerative disorders such as Alzheimer's or Parkinson's disease (Favaloro et al. 2012). Considering the important function attributed to the mitochondria in the execution of apoptotic signals, dysregulation of programmed cell death is another lurking consequence of mitochondrial dysfunction.

1.5 Mitochondrial diseases

Even though the intricate links between mitochondria and cellular function is well studied today, pathologic processes of mitochondrial disease still largely elude us. Syndromes associated with mitochondrial dysfunctions are very diverse. In some cases single organs are affected although most mitochondrial diseases are multisystemic syndromes. Symptoms can manifest themselves for the first time at any age and different severity levels are also commonly observed. Adding to this, disease phenotypes are overlapping: the same genetic defect can result in different phenotype expression and different gene mutations are seen in patients with similar clinical features (Wallace 1999; Turnbull & Rustin 2016). Defects in mitochondrial function unequivocally lead to human diseases but the spectrum of clinical manifestations is broad; neuromuscular problems, myopathy, cardiomyopathy, lactic acidosis, stroke, encephalopathy, optic neuropathy and deafness are among the most common symptoms

encountered (see **Table 1**). Over the years, mitochondrial diseases have been classified according to different criteria such as their genetic origin (nuclear or mitochondrial), biochemical impairments, or clinical syndromes (see **Table 2**). In addition, studies of mitochondrial dysfunction are important to human health as a number of hereditary disorders (such as diabetes), age-related diseases and normal ageing are associated with various degrees of mitochondrial impairment (see reviewed in Gorman et al. 2016; Swerdlow 2011; Finsterer 2004; Kauppila et al. 2016).

Table 1 Common clinical manifestations of mitochondrial diseases

Peripheral nervous system	Myopathy (ptosis, fatigue intolerance, cramps, muscle aching, lactic acidosis, stiffness), polyneuropathy (weakness, reduced or absent tendon reflexes, neuropathic pain, restless legs, sicca syndrome, absent or excessive sweating)
Central nervous system	Developmental delay, mental retardation or regression, early or late onset dementia, fatigue, epilepsy, myoclonic, migraine, stroke-like episodes, dystonia, dyskinesia, atypical cerebral palsy, leukoencephalopathy, basal ganglia calcifications, psychosis, myelopathy, coma
Endocrine system	Short stature, polyphagia, failure to gain weight, diabetes mellitus and insipidus, hypoglycemia, thyroid and parathyroid dysfunction, amenorrhoea, hypogonadism, delayed puberty, gynaecomastia, osteoporosis, hyperlipidaemia, hypopituitarism, hypoparathyroidism, hyperaldosteronism, adrenocorticotropin deficiency
Sensory nervous system	Hypacusis, sensorineural deafness, tinnitus, peripheral vertigo, cataract, glaucoma, pigmentary retinopathy, optic atrophy, uveitis, acquired strabism
Gastrointestinal system	Parodontosis, impaired swallowing, gastro-oesophageal reflux, delayed gastric emptying, dysphagia, chronic vomiting, inability to produce digestive enzymes, hepatopathy with liver failure and hyperammonaemia, recurrent diarrhea, villous atrophy, pancreatitis, constipation, failure to thrive, anorexia, malabsorption, intestinal pseudo-obstruction
Heart	Impulse generation and conduction defects, myocardial thickening, left ventricular hypertrabeculation/non-compaction, heart failure
Kidney	Renal tubular insufficiency, Fanconi syndrome, renal cysts
Bone marrow	Sideroblastic anaemia, leucopenia, thrombopenia, pancytopenia

Adapted by permission from RightsLink Permissions John Wiley and Sons: European Journal of Neurology, (Mitochondriopathies, Finsterer J.), COPYRIGHT, 2004.

Table 2 Mitochondrial Disease Classification

Classical classification (by acronym/syndrome)

CPEO, KSS, Pearson syndrome, MELAS, MERRF, LHON, Leigh syndrome, NARP, etc.

Biochemical classification

Defects of substrate transport
 Defect of substrate utilization
 Defects of the Krebs cycle
 Defects of the oxidation-phosphorylation coupling
 Defects of the respiratory chain

Genetic classification

Disorders due to mutations in the mtDNA genes encoding for RC proteins, tRNAs or rRNAs
 Disorders due to mutations in the nDNA genes encoding for RC proteins
 Disorders due to mutations in nDNA genes encoding for non_RC proteins
 Disorders associated with the RC defects due to mutations in nDNA genes encoding for non-mitochondrial proteins.

Adapted by permission from RightsLink Permissions John Wiley and Sons: European Journal of Neurology, (Mitochondriopathies, Finsterer J.), COPYRIGHT, 2004.

It was first postulated that impairment in ATP production was at the origin of mitochondrial diseases and that the vast diversity in the clinical manifestation was attributed to the energy requirements of each organ and the degree to which a gene mutation impairs respiratory chain function and ATP production (Wallace 1992; Wallace 1993). The particularity of mtDNA gene mutations which coexist with wild-type mtDNA molecule within a cell (heteroplasmy) also provided a rationale to explain the variation in clinical presentations of mitochondrial diseases. Today, the engineering of several animal models and the identification of patients with a variety of symptoms did not yet provide a satisfactory explanation for the unpredictability of mitochondrial diseases manifestation. The double nature of the genetic origin of mitochondrial diseases

(nuclear or mitochondrial) and the biochemical/metabolic dysregulation that leads to organ failure suggest that there is a much greater complexity at play and that the correlation between mitochondrial ATP production impairment and organ energy requirement is a poor predictor of the clinical manifestations of mitochondrial diseases. Indeed, in order to better understand the role of mitochondrial dysfunction in human health and disease, the organelle should be seen for its complex involvement in cellular function and as such more than just a power house (McBride et al. 2006).

A compelling discussion about the topic was formulated by several groups in the early 2000s (Brière et al. 2004; McBride et al. 2006). An interesting example is that of the optic nerve which was believed to be a vulnerable site due to its particularly high energy requirement. The optic nerve is the main organ affected in Leber hereditary optic neuropathy (LHON) but over the years, it was shown that the most common homoplasmic mutations causing LHON disease affect Complex I activity (K_m for NADH and electron transfer activity) albeit without significant decrease in ATP production (Majander et al. 1991; Larsson et al. 1991). In addition, several more mutations were discovered which impairs the respiratory chain and ATP production without any deleterious effect on the optic nerve. This theory also fell short to explain late onset mitochondrial diseases and the implication of mitochondrial dysfunction in age-related degenerative diseases. In other words, new hypotheses were needed to explain the wide clinical spectrum of mitochondrial and mitochondrial-related diseases. More than 10 years later, the complexing clinical manifestation of the majority of mitochondrial diseases is still widely discussed (McBride 2015; Turnbull & Rustin 2016; El-Khoury et al. 2013). Other hypotheses were brought forward and some remain hot topics today: superoxide toxicity, metabolic imbalance, accumulation of somatic mtDNA mutation with age, polymorphism of mtDNA, mitochondrial dynamics, etc.; but none of which have, on their own, been able to be a satisfactory explanation. The answer probably lay in the multifaceted functions of mitochondria, the cellular specific demands for

mitochondrial activity and additional stressors such as the environment and genetic predisposition.

The question remains therefore as to which extent OXPHOS dysfunction contributes to disease phenotypes, which cell types are vulnerable to mitochondrial activity loss (within which threshold) and how other aspects of mitochondrial function can be integrated in our understanding of mitochondrial disease physiopathology.

1.6 *Enzyme histochemistry*

Investigating the state of the electron chain activity in single cells is easily done with the use of mitochondrial enzyme histochemistry. This accessible method allows the visualization of mitochondrial activity without disturbing the structural integrity of the tissue, permitting each cell to be individually analyzed. By the 1980's, histochemical techniques had already identified focal mitochondrial Complex IV deficiency in diseases later found to be due to pathogenic, nuclear-encoded mitochondrial gene alleles (Müller-Höcker et al. 1983) or in normal ageing of human hearts (Müller-Höcker 1989). Later, again using mitochondrial enzyme histochemical methods, it was found that clonal expansion of mtDNA mutations with age leads to COX deficiency in many human tissues, and in vertebrate animal models of ageing (reviewed in Baines et al. 2014). Enzyme histochemical techniques have an advantage in the visualization of single cell dysfunction, compared to other biochemical measurements of tissue homogenates, where the averaging of biochemical competence across individual cells can mask cell-specific mitochondrial defects.

Quantitative analysis of COX activity has been described by several groups, where the oxidation of 3,3'-diaminobenzidine (DAB) catalyzed by COX is monitored using microphotometric assays (Old & Johnson 1989; Gonzalez-Lima & Jones 1994; Melendez-Ferro et al. 2013). A major drawback of this approach is the difficulty to clearly distinguish pathologic loss of COX activity due to normal activity being tightly linked to the unique energy demands of each cell type, where even segments of a cell

display heterogeneous activity (Wong-Riley 1989). Given the mosaic pattern of COX-deficiency typically observed in mitochondrial diseases, the distinction between a pathological decrease in COX activity and normal variation due to physiological characteristics is laborious. Alternatively, deficient COX activity can be revealed using a double-labelling method known as COX/SDH (cytochrome c oxidase / succinate dehydrogenase) histochemistry (Ross 2011). The COX/SDH method cleverly reveals cells with normal mitochondrial function in brown, through the oxidation of DAB, while cells with deficiencies in COX activity are revealed in blue. This dual color hinders the detection of low or intermediate deficiency levels which light blue color is obstructed by the predominant brown pigment, therefore, detection and quantification of COX deficiency remains incomplete (Murphy et al. 2012).

Immunofluorescence technique is also used to quantify the presence of several subunits of the respiratory chain complexes in tissues (Rocha et al. 2015; Hevner & Wong-Riley 1989; Grünewald et al. 2014). This later approach, on the plus side, enables simultaneous evaluation of Complex I and Complex IV expression in a single cell. In addition, immunofluorescence labelling is semi-quantitative and provides reliable and sensitive detection of protein expression. The downsides of this approach are the costs of species specific antibodies, the detection of protein rather than a measurement of enzyme function and like DAB cytochemical methods, a stringent comparison of very specific areas is required in order to reveal moderate changes in protein expression.

To obtain a greater sensitivity of a cell-by-cell detection of deficient COX activity, we developed a new enzyme histochemical assay that exploits the competing redox reactions between phenazine methosulfate (PMS), cytochrome c oxidase, and nitrotetrazolium blue chloride (NBT) - reagents well established in mitochondrial enzyme histochemistry. Old and Johnson in 1989 described with a microphotometric assay, optimal protocols for both the histochemical assay of SDH and COX activity. Their work was confirmed in mouse tissues, thereafter (Nakae & Stoward 2001). In addition, literature dating back to the 1950's describes the use of PMS for the reduction

of NBT (Farber & Bueding 1956; Nachlas et al. 1960) as well as the interaction of reduced PMS with Complex IV (Kearney & Singer 1955; Löw et al. 1964; Worsfold et al. 1977; Brody & Engel 1964). Building up on these previous works, we uncovered that the dual affinity of PMS for either NBT or Complex IV can be exploited to reveal COX-deficient cells without the use of DAB and sequential reactions. Indeed, PMS is a strong electron carrier that transfers electrons from Complex II to NBT, but in a complete system where mitochondrial COX activity is optimal, PMS preferentially passes on electrons to molecular oxygen via electron acceptors located in the COX subunits (Löw et al. 1964; Brody & Engel 1964; McMillan 1967). We show here that the alternative enzyme histochemical method - hereafter named nitrotetrazolium blue exclusion assay (NBTx) - can efficiently reveal surprisingly low levels of COX deficiency in single cells. The strength of this new assay is through the catalysis of formazan only where COX activity is dysfunctional, leading to the direct visualization of respiratory-deficient cells rather than a reduction in the predicted COX activity. The NBTx assay offers the unique opportunity to measure and quantify COX deficiency directly and unambiguously.

AIMS OF THIS STUDY

The development of a new enzyme histochemistry assay to visualize COX-deficient cells is the main focus of this study. We pursued the idea that a direct assessment of COX dysfunction with a single color would improve the read-out and provide a stronger tool for the evaluation of COX deficiency in fresh-frozen tissue samples.

With this body of work, we aimed to validate the biochemical interactions which regulate the new assay and demonstrate the strong correlation between COX deficiency and blue formazan deposition. In addition, we sought to define the limits and experimental set-up for a variety of tissue and organisms, including human tissues, to pave the way for a successful use of this new assay and improve reproducibility. Lastly, we developed ways to quantify COX deficiencies in heart tissues and skeletal muscles and demonstrate how being able to quantify COX-deficiency at the cellular level can help in advancing our knowledge of the physiopathology of mitochondrial diseases as well as being a valuable tool to assess treatment efficacy in regards to tissue recovery and respiratory chain activity.

MATERIALS AND METHODS

1.7 Ethics statement

All animal work was approved by the Landesamt für Natur, Umwelt und Verbraucherschutz Nordrhein-Westfalen in accordance with German and European Union regulations (Permits 84-02.042015.A103; 84-02.05.50.15.004).

The use of human tissues in this study was under the ethical guidelines issued by the Newcastle and North Tyneside Local Research Ethics Committees (reference 09/H0906/75 & REC ref. no.: 2001/188) and comply with the Declaration of Helsinki.

1.8 Preparation of incubation media

Phosphate-buffered saline (PBS, 0.1 M, pH 7.0) was prepared from mixing sodium dihydrogen orthophosphate monohydrate (0.04 M) to di-sodium hydrogen phosphate anhydrous (0.06 M).

NBTx solution contained 5 mg NBT dissolved in 3.2 ml PBS to which thawed stock solutions of PMS (100 µl/ml, 2.0 mM in purified water) and sodium succinate (100 µl/ml, 1.3 M in 0.1 M PBS) were added. Final concentrations were 130 mM sodium succinate, 2 mM NBT and 0.2 mM PMS, pH 7.0.

1.9 NBTx assay

Tissue Preparation – Small pieces of heart tissue were quickly frozen in 2-methylbutane, in a glass beaker cooled by immersion in liquid nitrogen. Frozen tissues were stored at -80 °C until ready to use. Testis and colons were frozen in Tissue-Tek® O.C.T. compound (supplied by A. Hartenstein GmbH, Wuerzburg, Germany) immersed into liquid nitrogen. Brain tissues were frozen slowly on dry ice. Heart tissues were cut

at 7 μm whereas brains, skeletal muscles, testis and colons were cut at 10 μm with a cryostat at $-20\text{ }^{\circ}\text{C}$ (OFT 5000, Bright Instruments, Luton, UK), mounted on Superfrost Plus microscope slides (Menzel, Thermo Scientific, Waltham, MA, USA) and air-dried for 5 to 10 minutes. Slides were kept at $-80\text{ }^{\circ}\text{C}$ for maximum a few months to avoid the loss of enzyme activity.

Staining Protocol – Slides were taken out of the $-80\text{ }^{\circ}\text{C}$ freezer and thawed briefly at room temperature on a slide holder without lid. Sections (3 sections per slide) were then covered with 1ml PBS for 10 minutes in an incubator set at the desired temperature (1 ml per slide). PBS was discarded and replaced with 1 ml NBTx solution. Incubation time and temperature varies according to tissue type. Generally, best results were obtained with heart sections at $18\text{ }^{\circ}\text{C}$ for 30 minutes. Brain, skeletal muscles and testis required a higher incubation temperature (22 to $25\text{ }^{\circ}\text{C}$).

Sections were washed briefly in purified water followed by dehydration in ethanol (2 minutes in 50 %, 75 %, 96 %, 100 % followed by an extra 5 minutes in 100 % ethanol). Finally, slides were immersed for 5 minutes in two changes of xylene before mounted on coverslips with Cytoseal™ (Thermo Scientific, Darmstadt, Germany).

1.10 Inhibiting the respiratory chain

Sodium azide and potassium cyanide were dissolved in water, malonate in 1 M sodium hydroxide and all other inhibitors in absolute ethanol at the following concentration: thenoyltrifluoroacetone (TTFA, 1 mM), atpenin A5 (0.1 mM) sodium azide (100 mM), potassium cyanide (100 mM), rotenone (1 mM), antimycin A (1 mM), myxothiazol (0.2 mM), oligomycin (3 mM) and malonate (6 M). Stock solutions were stored at $-20\text{ }^{\circ}\text{C}$ and thawed shortly before use. Inhibitors were added to PBS for the preincubation time as well as to the NBTx solution (rotenone, oligomycin, antimycin A 1:500; myxothiazol, atpenin A5, TTFA 1:200; sodium azide, potassium cyanide 1:100, malonate 1:1000). Control conditions contained 5 $\mu\text{l/ml}$ of 100 % ethanol or 1 $\mu\text{l/ml}$ 1 M NaOH accordingly. All conditions retained a neutral pH value between 6.9 and 7.2.

1.11 Mouse tissues

All mouse lines used in all experiments were maintained on the C57Bl/6NCrI nuclear background (Charles River Laboratories, Germany, strain code 027). *Lrpprc* conditional knockouts (MGI:5438915) and *Surf1* knockout mice (MGI:2651426) were kindly provided by the group of Nils-Göran Larsson, Department of Mitochondrial Biology, Max Planck Institute for Biology of Ageing, Cologne. mtDNA mutator mice (MGI:3046825) were F1 animals born to true C57Bl/6NCrI females from the P generation to minimized mtDNA mutagenesis (Trifunovic et al. 2004). The *mt-tRNA^{ALA}* m.5024C>T mice (MGI:5902095) are maintained by female transmission of the mutated mtDNA in crosses to C57Bl/6NCrI males (Kauppila et al. 2016).

1.12 Human tissues

Human skeletal muscle (*vastus lateralis*) and cardiac tissue were obtained through the NHS Highly Specialised Services located within the Wellcome Centre for Mitochondrial Research at Newcastle University. All samples were obtained and used with informed consent. Human colon tissue was obtained from patients with colorectal tumors undergoing surgical resection. Normal mucosa was taken from at least 20 cm from the resection margin. Informed written consent was obtained prior to surgery and samples were coded to maintain confidentiality. This project was approved by the Joint Ethics Committee of Newcastle and North Tyneside Health Authority (REC ref. no.: 2001/188). All tissues were cut at 7 µm and consecutive sections were used to compare COX/SDH (40 minutes COX, 40 minutes SDH at 37 °C), NBTx (20 minutes at 37 °C) and COX-only (skeletal muscles and hearts - 40 minutes, colons – 30 minutes at 37 °C).

1.13 Fruit flies, *Drosophila melanogaster*

Fly models were kindly provided by the group of Nils-Göran Larsson, Department of Mitochondrial Biology, Cologne, Germany. See references for maintenance and engineering of *Lrpprc2* RNAi (Baggio et al. 2014) and DmPolγA –

compound heterozygous $\text{tam}^{\text{D263A}}/\text{tam}^{\text{H1038A}}$ – (Bratic et al. 2015). Flies were quickly frozen in liquid nitrogen and subsequently glued on a cryostat mounting disk with fixing gel (Tissue-Tek® O.C.T. compound). Sections of the thorax muscles were cut at 10 μm and mounted on microscope slides. NBTx assays were performed at 18°C for 10 minutes.

1.14 Hypoxic conditions

Heart tissues were cut and sections placed on microscope slides as for the standard NBTx experiments. PBS buffer was placed with lid open inside an oxygen controlling chamber system (COY Laboratory Products) 30 minutes before the start of the experiment. Chamber parameters were set for 2.0 % oxygen and 5.0 % CO_2 . Temperature and humidity inside the chamber was measured around 24 °C and 22 % relative humidity. Microscope slides with 7 μm thin section of mouse heart tissue were placed inside the chamber. PBS buffer was added to the slides and incubated for 10 minutes followed by the usual NBTx buffer for 10, 20 or 30 minutes. After the incubation time, slides were taken out of the chamber and transferred into water for 5 minutes, dehydrated in ethanol and xylene before mounting with cover slips.

1.15 COX/SDH assay

The protocol used here is according to a standard protocol utilized across diagnostic histopathology laboratories (Ross 2011).

1.16 Succinate dehydrogenase activity

SDH activity was measured by removing PMS from the NBTx staining solution. Without the presence of PMS as an intermediate electron carrier, the catalysis of NBT into formazan crystals is weak but independent of the activity of Complex IV. Alternatively, to mimic 100% COX deficiency in tissues, SDH activity was also assessed with 1 mM sodium azide in the NBTx solution.

1.17 DAB histochemistry

3,3 diaminobenzidine tetrahydrochloride (DAB) is dissolved in purified water followed by an equal part of 0.2 M phosphate buffer, pH 7.0 for a final concentration of 5 mM. Prior to staining, cytochrome c (100 μ M) and catalase (0.2 mg/ml) are added.

1.18 Laser microdissection and quantitative pyrosequencing

Heart tissues are cut at 12 μ m and collected onto PEN-membrane slides (Leica, Microsystems GmbH, Wetzlar, Hesse, Germany) and stained for 30 minutes using the NBTx assay. Areas stained blue or areas with no coloration were then laser micro-dissected (LMD7000, Leica) and collected into sterile 0.5 ml centrifuge tube. The collected sections are lysed with 10 μ l of lysis buffer (50 mM Tris-HCl pH 8.5, 1% Tween-20, 20 mg/ml proteinase K) followed by a 2 hours incubation at 55°C. Proteinase K is denatured by a 10 minutes incubation at 95 °C. Pyrosequencing analysis of the m.5024C>T mutation was performed using a PyroMark Q24 pyrosequencer and the design software v2.0 (Qiagen GmbH, Hilden, Germany). A single PCR reaction amplifies a 178 bp PCR fragment spanning the m.5024 mutation site, using a biotinylated forward primer and a non-biotinylated reverse primer (forward primer: 5'-Biotin-TTCCACCCTAGCTATCATAAGC, reverse primer: GTAGGTTTAATTCCTGCCAATCT). PCR products were combined with dH₂O, PyroMark binding buffer (Qiagen) and 1 μ l Streptavidin sepharose™ high performance beads (GE Healthcare, Little Chalfont, UK), and purified and denatured using a Pyromark Q24 vacuum workstation. Sequencing was carried out with PyroMark Gold Q24 Reagents according to manufacturer's directions, using the sequencing primer (TGTAGGATGAAGTCTTACA). For calibration curves, mixture of synthetic biotin-labelled oligos were mixed, which correspond to wild-type and mutant sequences.

1.19 *Statistical analyses*

Pyro sequencing data was analyzed with GraphPad Prism 7 software. A one-way ANOVA with Dunn's multiple comparisons test was used to establish statistical significance between the percentage of m.5024C>T mutations in clear versus light blue areas, white versus dark blue areas and light blue versus dark blue areas.

1.20 *Image acquisition, processing and analysis*

Images were obtained using a Nikon Eclipse Ci microscope and processed with Fiji (open-source software, Schindelin et al. 2012). The following steps were written in a single macro command: white balancing, color deconvolution and threshold (Huang and Wang 1995) followed by total image analysis of area, mean intensity and standard deviation values. In addition, processed images were stacked and the total pixel number for each intensity value (0-255) was analyzed with the histogram command. Full details of the macro can be found in the section **Appendix A**. The macro is written to process many images at once, making it easier to analyze groups of images. When prompted by the macro, select a folder containing the images.

1.21 *Quantitative analysis of skeletal muscle*

Skeletal muscles of mice hindlimb (gastrocnemius and soleus) were cut in serial sections of 10 μm for NBTx and SDH assays and 12 μm for myosin ATPase reactions. Images processed with the macro were loaded to ImageJ again and single fibres were selected and analyzed individually. Excel and GraphPad Prism 7 were used to compare maximal formazan catalysis (SDH assay) to the blue intensity generated with the NBTx reaction (mean relative OD). Single cells were identified in 3 consecutive sections placed side-by-side on one slide. Values were normalized to the mean intensity of a large area of each slide to account for variability (see also **Appendix B** for raw data).

RESULTS

1.22 Competing biochemical reactions

In the course of our research on heart tissues of a variety of mouse models presenting intermediate or low level respiratory chain defects, we came across several difficulties when attempting to confidently assert the degree of COX deficient cells with available enzyme histochemistry methods (**Figure 4.1**). Standard sequential cytochrome *c* oxidase/succinate dehydrogenase (COX/SDH) protocol used in our laboratory fell short to identify COX deficiency in our mouse models. Besides the long incubation time required for a successful exposure of COX-deficient mitochondria, cells with low or intermediate levels of COX deficiency appear purple or greyish which makes detection and quantification difficult. Animal models with near threshold level of mitochondrial dysfunction display cells with a tint of blue that is confusingly close to colors observed in wild-type sections where the SDH activity was unsuccessfully blocked. An attempt to find the best parameters to reveal maximum deficient mitochondria without unmasking healthy ones easily becomes a struggle.

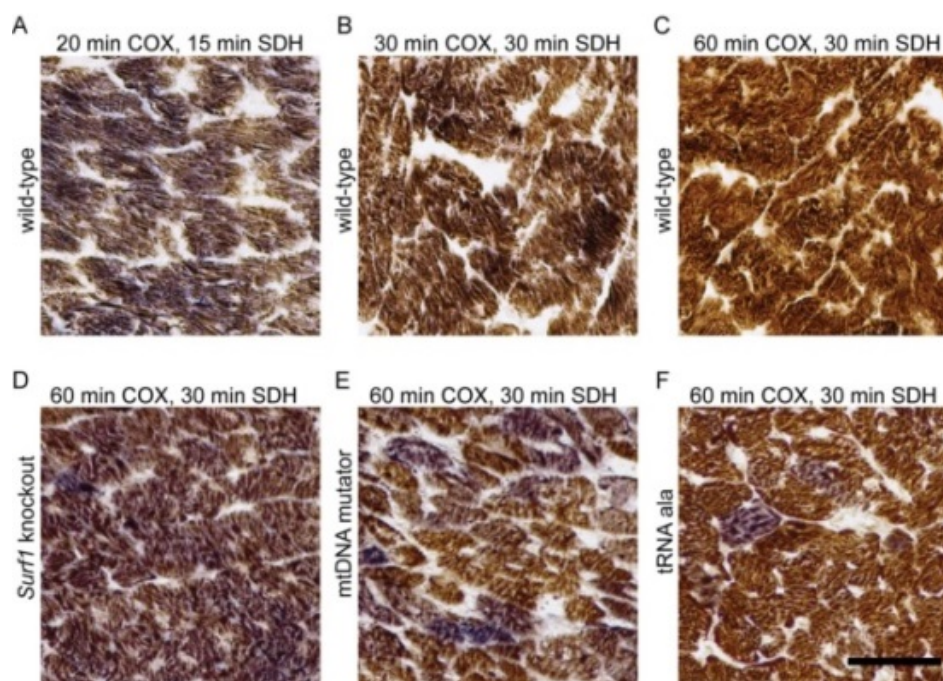


Figure 4.1 | Sequential COX/SDH staining has drawbacks in models with near threshold deficiency. (A) Heart sections of wild-type C57BL/6N mice stained at 37°C for 20 minutes with DAB and 15 minutes SDH, shows insufficient blocking of SDH activity as shown with the mix of unsaturated and blueish browns. (B) 30 minutes DAB and 30 minutes SDH appear to sufficiently block SDH. (C) 60 minutes DAB and 30 minutes SDH reveals a much saturated and yellowish brown suggesting that the previous condition was only partly blocking formazan catalysis. (D) *Surf1* knockout mouse, (E) mtDNA mutator mouse, (F) *mt-tRNA^{ALA}* mutant mouse. Number of animals tested for each condition equals at least 3. Scale bar, 50 μ m.

It will be demonstrated here that a strong biochemical competition between COX and NBT for the acquisition of electrons from PMS forms the basis for the NBTx assay, a new enzyme histochemistry assay which identifies lower threshold of COX deficiency and allows the acquisition of quantifiable data.

The NBTx assay involves only one color (blue formazan crystals from NBT) and is based on a strong biochemical competition between COX and NBT for the acquisition of electrons from PMS (see reaction scheme **Figure 4.6**). In COX-competent mitochondria, minimal or no catalysis of formazan takes place and cells remain colourless.

Using sodium succinate as a substrate and in absence of PMS, NBT reduction leads to visible formazan pigments accumulation - an indication of the succinate dehydrogenase activity (**Figure 4.2A**). This activity is independent of Complex IV and no effect is observed when blocking its oxidative activity with sodium azide (**Figure 4.2B**). However, formazan formation was strongly blocked by atpenin A5 (**Figure 4.2C**), a potent Complex II inhibitor (Miyadera et al. 2003).

Adding PMS has long been shown to improve the rate of formazan catalysis, but its use in tissue sections is known to be beneficial only with a COX inhibitor (L6w et al. 1964). We therefore speculated that PMS is capable of transferring electrons to Complex IV and that this reaction is favored over its ability to reduce NBT. To confirm this, we incubated heart sections with PMS (0.2 mM), NBT (2 mM) and sodium succinate (130 mM) in the absence of any COX inhibitors. We observed that catalysis of formazan is effectively suppressed, suggesting the inability of PMS to reduce NBT in the presence of a functional COX activity. NBT molecules remained in their oxidized form even after prolonged incubation (**Figure 4.2D-F**). As expected, NBT reduction is fully restored using sodium azide (1 mM) or potassium cyanide (1 mM), two COX inhibitors (**Figure 4.2G,H**). Sodium succinate removal prevents this effect (**Figure 4.2I**).

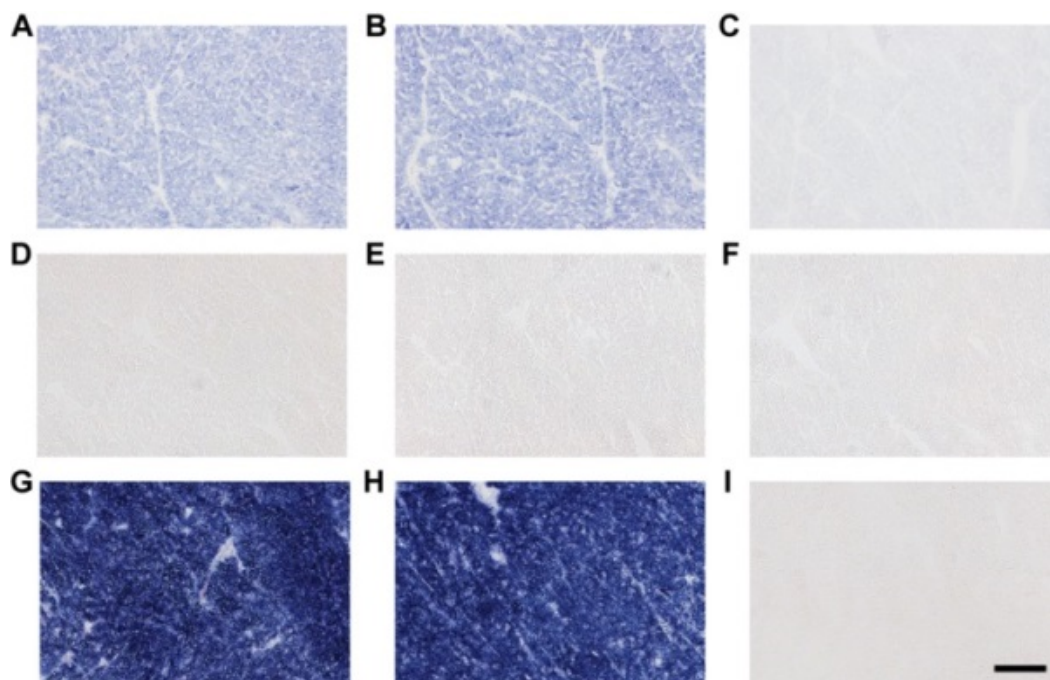


Figure 4.2 | PMS engages both the activity of Complex II and Complex IV. (A) Succinic dehydrogenase activity is detected in wild-type heart tissues using sodium succinate as a substrate and NBT as a final electron acceptor ($n = 3$). (B) Blocking COX activity with sodium azide does not prevent NBT reduction ($n = 3$). (C) Inhibiting the quinone-binding site of Complex II with atpenin A5 fully blocks the transfer of electrons to NBT (500nM, $n = 3$). Wild-type heart tissues treated with a solution containing 0.2 mM PMS in addition to sodium succinate and NBT significantly represses the catalysis of blue formazan crystals for (D) 10 minutes (E) 20 minutes or (F) 30 minutes incubation at 18°C ($n = 5$). (G) Complete reduction of NBT is rescued by chemically blocking COX with sodium azide (1mM, 10 minutes, $n = 15$), or (H) potassium cyanide (1mM, 10 minutes, $n = 3$). (I) Removing sodium succinate prevents formazan formation even in the presence of sodium azide (10 minutes, $n = 3$). Scale bar, 100 μm

To confirm the specificity of Complex IV in preventing the transfer of electrons from PMS to NBT, we attempted to restore NBT reduction with various electron transport chain inhibitors: Complex I (rotenone, 2 μM), Complex III (antimycin A, 1 μM and myxothiazol, 1 μM) and inhibited ATP synthesis (oligomycin A, 6 μM). None of the tested inhibitors could restore NBT reduction (**Figure 4.3**). In addition, the source of electron transfer from Complex II to PMS was confirmed using antimycin A, atpenin A5 and malonate (**Figure 4.4**).

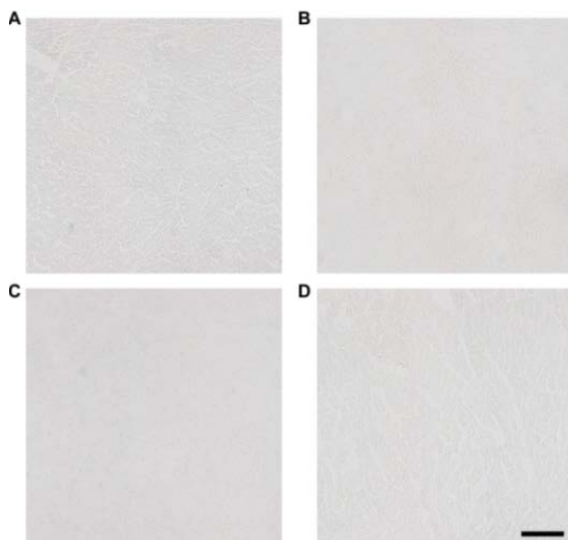


Figure 4.3 | Inhibiting mitochondrial complexes other than Complex IV does not reestablish the reduction of NBT. Heart sections from wild-type mice were incubated 10 minutes in NBTx solution containing the following inhibitors: (A) rotenone (2 μ M), (B) antimycin A (1 μ M), (C) myxothiazol (1 μ M), (D) oligomycin (6 μ M). Representative images of 3 experiments. Scale bar, 100 μ m.

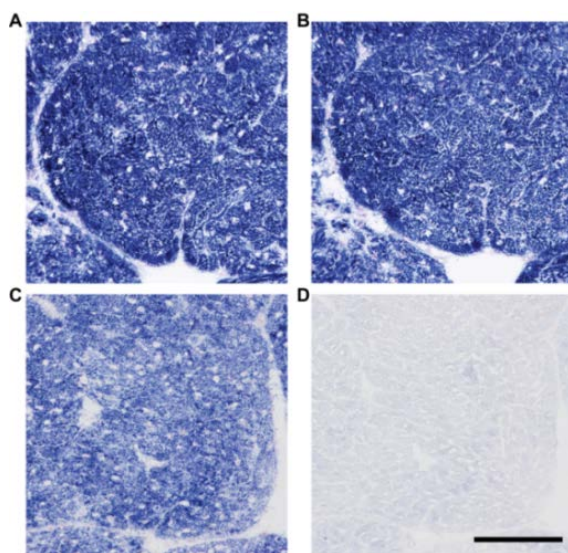


Figure 4.4 | Site of electron transfer from Complex II to PMS. (A) NBTx + sodium azide (1 mM) (B) NBTx + sodium azide and antimycin A (1 μ M) (C) NBTx + sodium azide and atpenin A5 (5 μ M), (D) NBTx + sodium azide and malonate (6 mM). Representative images of 3 experiments. Scale bar, 100 μ m.

Our results indicate that once reduced by Complex II, PMS will transfer electrons to COX or NBT bypassing the classical respiratory chain electron pathway. Thus, in the presence of PMS, NBT reduction into formazan only depends on the respective activities of Complex II and COX.

As NBT reduction depends on the absence of COX activity and because oxygen is a substrate of COX, its concentration modulates COX catalytic activity and substrate affinity (Chandel et al. 1996), we hypothesized that formazan formation could be influenced by oxygen pressure and availability. This possibility was examined with heart tissues of young (12 weeks old) wild-type mice in a chamber containing 2% oxygen. Low-oxygen conditions led to a rapid accumulation of formazan pigments (**Figure 4.5A**). Likewise, elevated levels of formazan deposition were noted in young hearts incubated at high temperature, which we speculate increased the reaction rate and caused a more rapid depletion of dissolved oxygen in the incubation media (**Figure 4.5B**). High relative humidity also led to a slow deposition of formazan crystals over time, suggesting again that oxygen depletion is an important factor which influences the outcome of the NBTx assay (**Figure 4.5C**).

Our findings point to a strong interplay between PMS, Complex II and Complex IV that is independent of the rest of the respiratory chain, in agreement with previous reports (Farber & Bueding 1956; Nachlas et al. 1960; Kearney and Singer 1955, Löw et al. 1964). In light of these observations, we suggest a model where PMS interacts preferentially with Complex IV, hindering its ability to deliver electrons to NBT. In this scenario, NBT reduction serves as an indicator of the loss of COX activity and thus enables fast and sensitive detection of COX-deficient cells (**Figure 4.6**).

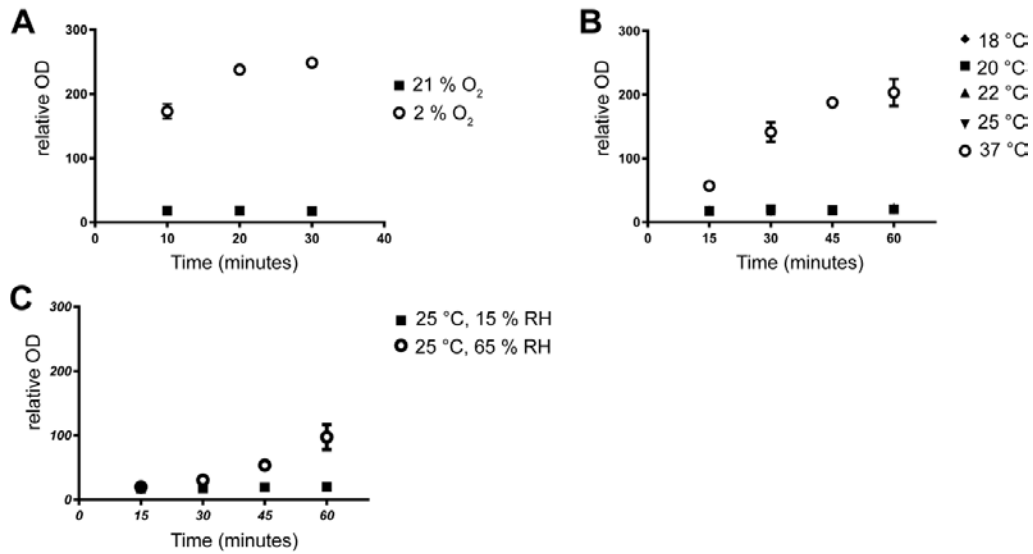


Figure 4.5 | Stability of a negative signal is dependent on oxygen. Wild-type hearts from 12 weeks old mice were used to test the stability of a negative signal. (A) Hypoxic conditions (2% oxygen) induced formazan deposition after 10 minutes at room temperature. (B) Slight variation in the temperature (between 18 and 25°C) did not significantly increase formazan deposition although high temperature (37°C) for heart tissues causes a gradual accumulation of formazan crystals. (C) Lastly, we observed that high relative humidity levels (65%) increase formazan deposition in a healthy tissue and can influence the maintenance of a colorless background at a given temperature. N = at least 3 for each condition.

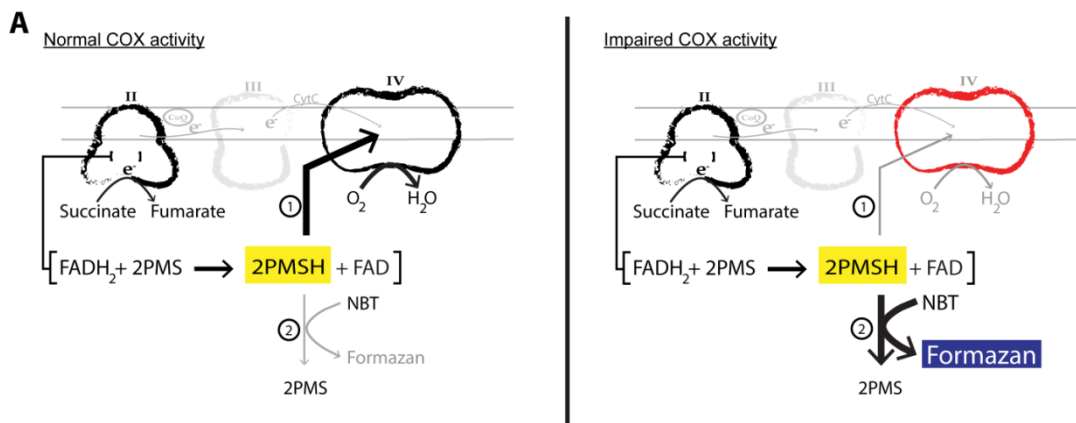


Figure 4.6 | Proposed interaction scheme. PMS is reduced within Complex II and subsequently re-oxidized by COX, leaving NBT in its colorless, oxidized form (marked as ①). When the oxidative activity of Complex IV is either artificially blocked or deficient, PMS is efficiently passing electrons to NBT which triggers the formation of blue formazan crystals (marked as ②).

1.23 COX-deficient mitochondria in mouse models

Based on the biochemical interactions described above, we predicted that deficient cells within tissues of transgenic mice with known COX deficiency would be revealed by the deposition of formazan crystals. In order to verify this, we analyzed four different transgenic mouse models previously characterized and presenting different levels of COX deficiency in the heart, namely: *Lrpprc* conditional knockout (*Lrpprc/CKMM-cre*) (Ruzzenente et al. 2011; Mourier et al. 2014), *Surf1* knockout (Dell'Agnello et al. 2007; Agostino et al. 2003), the *PolgA*^{D257A} mtDNA mutator (Trifunovic et al. 2004) and a mouse heteroplasmic for an mtDNA m.5024C>T mutation in the *tRNA^{ALA}* gene (mt-*tRNA^{ALA}* mice, Kauppila et al 2016). *Lrpprc/CKMM-cre* conditional knockout mice have an extensive loss of Complex IV in heart tissues, with enzyme activities decreased by 90% already at 12 weeks of age (Ruzzenente et al. 2011). *Surf1* knockout mice are reported to suffer a loss between 30-50% of COX activity (Mourier et al. 2014, Dell'Agnello et al. 2007) whereas mtDNA mutator mice lose around 25-30% (Ross et al. 2013). Mice harboring the *mt-tRNA^{ALA}* mutation show only sparse COX impairment (Kauppila et al. 2016). The NBTx assay revealed that across all mouse models, qualitative levels of formazan crystal deposition correlated to the mitochondrial COX deficiency previously reported (**Figure 4.7**). The darkest blue pigments were seen in *Lrpprc* knockout heart sections, followed by *Surf1* knockout, the mtDNA mutator mouse, with the lowest amount observed in mouse heart with the mt-*tRNA^{ALA}* mice. The ease at which COX-deficient cells are revealed is especially evident in the *Surf1* knockout model (**Figure 4.7B**). The relevance for this new approach is particularly striking when compared side-by-side with sequential COX/SDH or COX-only histochemistry. The NBTx assay reveals even slight changes in COX activity, with cells clearly distinguishable with a light blue tint, whereas the same area in the COX/SDH serial section reveals a puzzling presentation of colors that vary from purple-brown or even greyish-blue, which may lead to ambiguous interpretations and hinder proper quantification (Murphy et al.

2012). Likewise, images of heart tissue reacted to DAB only show COX-positive activity which is a disadvantage when assessing for the presence of defective oxidative activity. For example, in the *Lrpprc* knockout heart tissue (**Figure 4.7A**) we identified 3 areas with distinct intensity of formazan deposition (labelled 1 to 3) in the NBTx assay. The same areas in the COX/SDH shows characteristic colour variation but the light blue, seen in the NBTx section of area #1, is undetected in both the COX/SDH and the COX-only histochemistry methods. Furthermore, when COX deficiency is partial and equally distributed across the tissue (as seen in *Surf1* knockout mice) COX-only histochemistry poorly performs in revealing COX-deficient mitochondria (**Figure 4.7C**). Overall, the newly developed NBTx assay successfully reveals COX-deficient mitochondria in tissue sections and is more sensitive than previous methods.

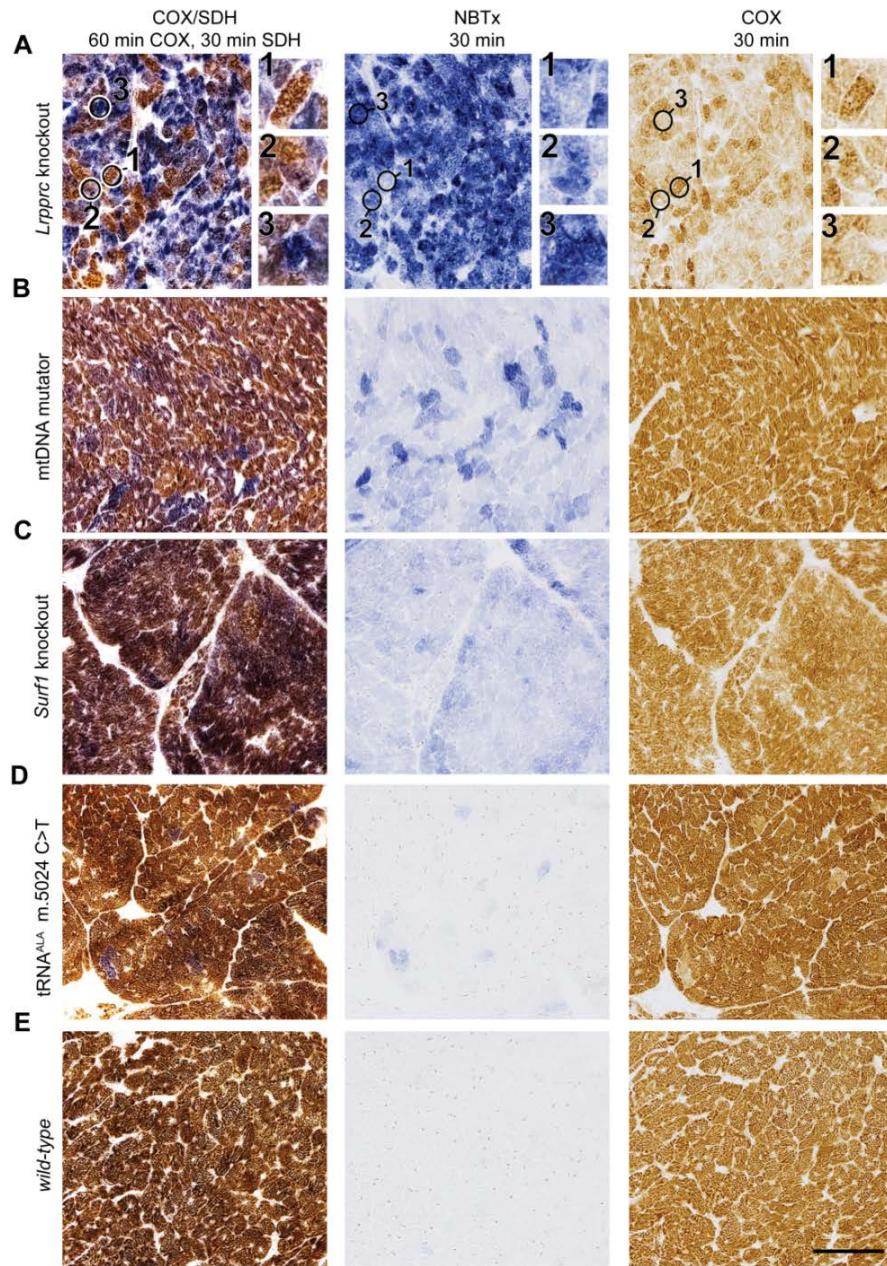


Figure 4.7 | COX-deficient cells in mouse heart tissues. Fresh frozen heart tissues from mice models with COX deficiencies are shown here after COX/SDH, NBTx or COX-only histochemistry. (A) *Lrpprc* knockout (n = 3), (B) mtDNA mutator (n = 3), (C) *Surf1* knockout (n = 3) (D) mt-tRNA^{ALA} m.5024C>T (n = 5), (E) wild-type (n = 5). Scale bar, 100 μ m.

1.24 Quantification of COX deficiencies

A mosaic distribution of affected cells within a given tissue is a characteristic of many mitochondrial diseases. Quantifying this variation would help decipher the correlation between cellular OXPHOS deficiencies and disease mechanism. To demonstrate the high sensitivity and reproducibility of the NBTx reaction, we proceeded to evaluate the degree of blue formazan crystals in wild-type heart tissues exposed to increasing amounts of sodium azide.

For this purpose, a simple and accessible workflow was developed using images captured with an upright microscope and subsequently analyzed with Fiji, a free image processing software (see **Appendix A**, Fiji Macro).

Concentrations as low as 5 μM induced a small, detectable change in relative optic density (ROD) measurements followed by a gradual increase which plateaus at about 100 μM . A linear relationship was detected in the range of 5 to 25 μM sodium azide (**Figure 4.8A**). Completely blocking mitochondrial activity with 1 mM sodium azide saturates the image with an average ROD of 252 ± 1.5 (not shown).

The variation in cellular dysfunction within the tissue is lost when the average ROD is calculated rather than the single cell values. We reanalyzed the images from the sodium azide treated heart tissues and extracted total number of pixels for each intensity level. Figure 8c shows a distribution curve with an important distribution of values across the range but interestingly, each sodium azide concentration creates a unique and consistent curve. The distribution of mitochondria within a cell and the variation in mitochondrial density between regions, as well as spaces between cells in the tissue might explain this distribution (see close up images in **Figure 4.8B**). We arbitrarily assigned a range of blue optical densities which would represent low, intermediate and high levels of COX deficiency, with the goal of establishing the distribution levels in distinct animal models. Plotting the number of pixels versus the blue ROD values for the

four different animal models resulted in similar curves (**Figure 4.8D**). Moreover, each animal was plotted individually as to assess variability within each group.

Our data shows that the new NBTx assay accurately reveals COX deficiency with a very high sensitivity. The absence of brown pigments in functional mitochondria led to a clearer and consistent distinction of blue intensities. Our image analysis enables the extraction of valuable information such as: COX deficiency levels – as an average ROD for the entire tissue or as a spectrum within the tissue (number of pixels per ROD), variability within one specific genetic line (e.g.: we found that mtDNA mutator mice as well as *Surf1* knockout mice varied substantially between each animal, whereas *Lrpprc* knockout and mt-tRNA^{ALA} mice tended to be consistent (**Figure 4.8D**)).

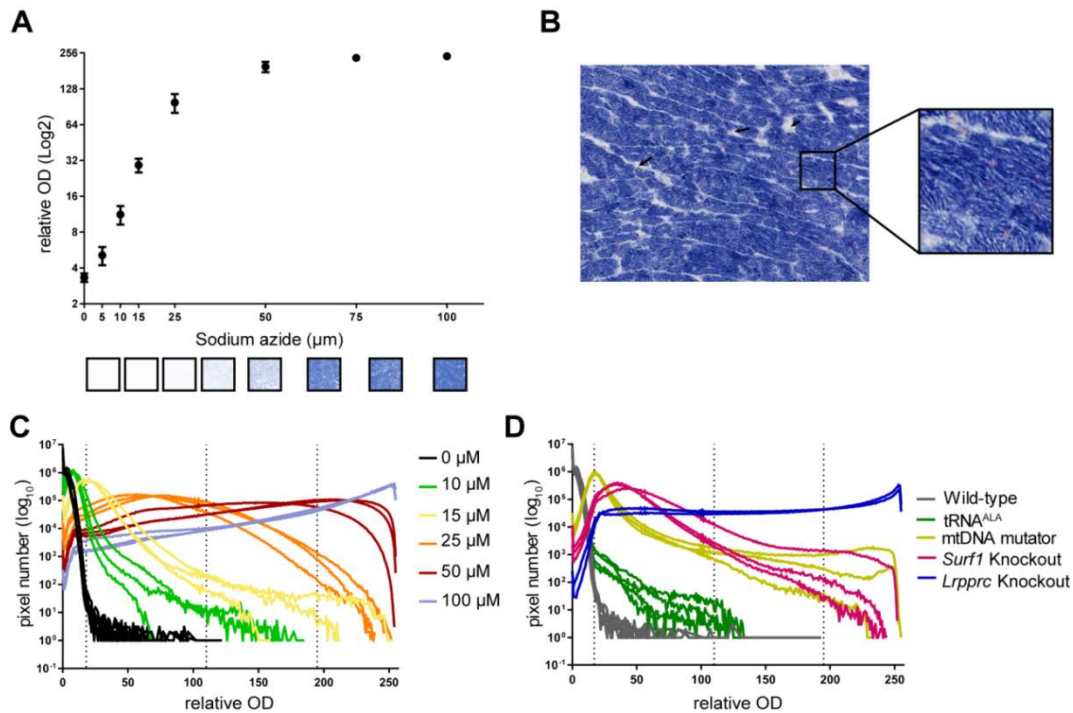


Figure 4.8 | Quantifying COX deficiency in heart tissues. **(A)** Fresh frozen heart tissues, sectioned at 7 μm , were exposed to different concentrations of sodium azide (0, 5, 10, 15, 25, 50, 75 and 100 μM). Average blue intensity is calculated using Fiji software and plotted against each sodium azide concentration. Numbers represent mean \pm SD from 6 images per animal ($n = 3$, 12 week old males). Representative images for each azide concentration are shown under the graph. **(B)** Images of a section of heart tissue exposed to 75 μM sodium azide and the NBTx solution. Arrows show unstained areas of connective tissues or holes in the tissue. Image inset shows the non-homogenous intensity of formazan deposition within the cytoplasm. **(C)** Selected concentrations of sodium azide were plotted showing total pixel number from 6 images against each ROD value. Dashed lines are arbitrary range for background, low, intermediate and high deficiency which we transposed also to tissues of animal models. **(D)** Heart tissues of *Lrpprc* knockout, *Surf1* knockout, mtDNA mutator and mt-tRNA^{ALA} mice compared to aged matched wild-type tissue. Each line represents results of replicate experiments for different animals.

In skeletal muscles, where mitochondrial activity varies greatly between muscle fibre types, we performed single cell analysis. Consecutive slides were used to distinguish fibre types with myosin ATPase reactions at pH 4.3 and 10 in addition to a section for histochemical assay of SDH activity. The intensity of formazan deposition as measured in the SDH assay was used to distinguish fiber types of similar mitochondrial activity. Three different types of fibers in mtDNA mutator mice hindlimb (gastrocnemius and soleus) - fiber type I, type II (oxidative) and type II (glycolytic) - were identified and used to make an evaluation of each fiber's characteristic COX impairment (**Figure 4.9A to H**). We found no significant difference in SDH activity between wild-type or mutant animals (**Figure 4.9I**, see also **Appendix B** for raw data).

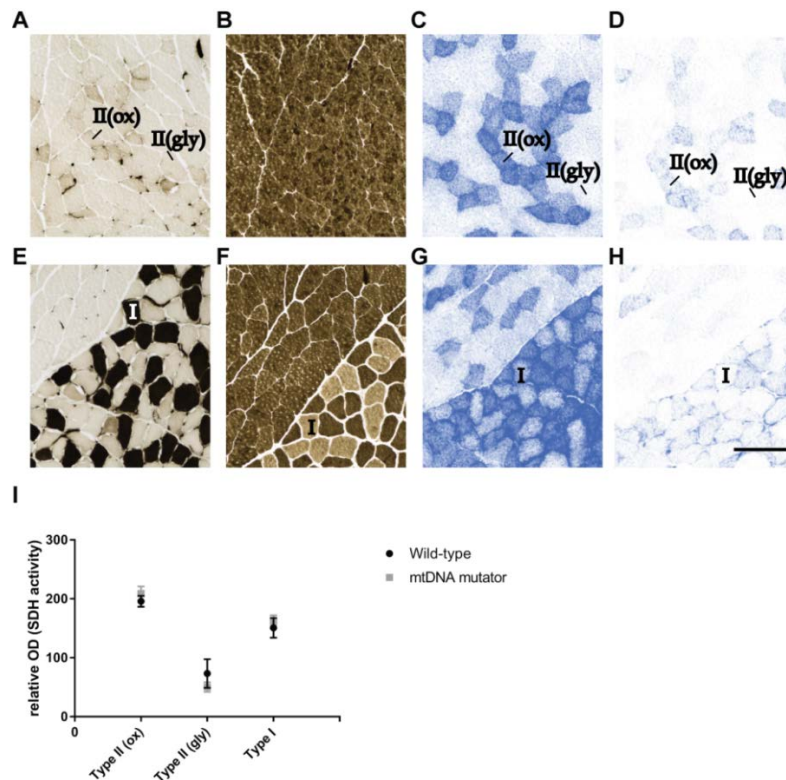


Figure 4.9 | Quantification of skeletal muscle fibre types. Consecutive sections of the gastrocnemius and soleus muscles of mtDNA mutator mice were reacted to (**A, E**) myosin ATPase at pH 4.3, (**B, F**) myosin ATPase at pH 10, (**C, G**) SDH assay, (**D, H**) NBTx assay. SDH and NBTx reactions were run simultaneously at 18°C for 30 minutes. (**I**) Relative optical density (OD) depicting SDH activity in the skeletal muscle. Individual cells from type II (oxidative, ox or glycolytic, gly) and type I fibres were selected in wild-type and mtDNA mutator mice. Mean relative OD \pm SD (n = 3). Scale bar, 100 μ m.

Having established that baseline SDH activity was characteristic across the different fiber types but uniformed between cells of the same type and is not significantly altered in the mtDNA mutator mice compared to wild-type mice, we completed our analysis with measurements of single cell COX deficiency levels. Our results show that fiber types with greater oxidative activity (type II (oxidative) and type I) are more strongly affected than glycolytic fibers (**Figure 4.10A**). Although in oxidative type II fibres COX deficiency can reach high levels (seen in our samples up to 70%), there is no correlation between a high COX deficiency and a high SDH activity. In other words, this demonstrate further that formazan deposition in the NBTx assay strongly correlates with COX deficiency and that the scenario where a shift in the stoichiometric proportion between SDH and COX in favor of more SDH molecules is unlikely (**Figure 4.10B**).

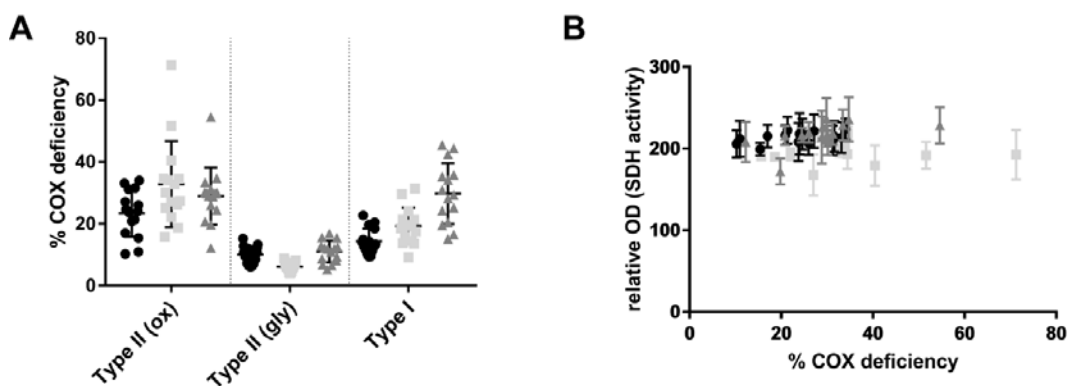


Figure 4.10 | COX deficiency measured in 3 different fibre types. **(A)** Fiber type II (oxidative, ox), type II (glycolytic, gly) and type I from the skeletal muscle of three mtDNA mutator mice. Each dot represents a single cell, with 15 cells per column, with mean and standard deviation shown. **(B)** Oxidative type II fibres were used to compare % COX deficiency to the value of SDH activity (relative OD, mean value of 3 replicates with standard deviation) obtained for each single cell.

1.25 MtDNA heteroplasmy in heart tissues

Cellular heteroplasmy describes the presence of wild-type and mutated copies of mtDNA molecules at a ratio that varies between organs and individual cells. The increase of this ratio towards the mutated variant is critical in the development of mtDNA-induced mitochondrial disease or may be a risk factor in the development of other age-related diseases (Stewart & Chinnery 2015). Using the NBTx assay, we were able to easily expose various levels of COX deficiency in heart tissues of mice with a point mutation in the *mt-tRNA^{ALA}* gene. Pups were assayed at weaning for their relative levels of the m.5024C>T mtDNA mutation using whole tissue quantitative pyrosequencing. Even mice with relatively high levels of the m.5024C>T mutation had low numbers of detectable dysfunctional cells within the tissue (Kaupilla et al. 2016). Heart sections reacted with the NBTx assay revealed areas with low (clear), intermediate (light blue) or high (dark blue) formazan catalysis (**Figure 4.11A**). We proceeded to isolate the different areas using laser capture microdissection with subsequent pyrosequencing to assay the relative m.5024C>T mutation level within the laser captured area. As expected, we observed a significant increase in the relative levels of the m.5024C>T mutation in dark or light blue areas, confirming a correlation between high relative levels of this pathogenic mutations and the presence of deficient COX activity (**Figure 4.11B**).

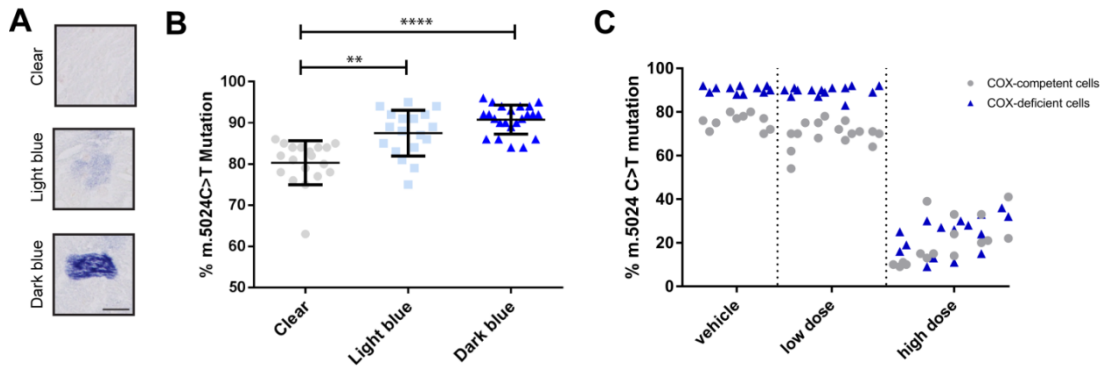


Figure 4.11 | Link between heteroplasmy levels and COX deficiency. (A) The high contrast ensued from the NBTx treatment of heart sections, allows a clear distinction of areas with low (clear), intermediate (light blue) or high (dark blue) formazan deposition. Scale bar, 20 μm . (B) Each area was collected separately with a laser dissecting microscope and analyzed using pyrosequencing technology. Results of at least 5 laser-capture microdissections for each color, from 4 different mice carrying heteroplasmic m.5024C>T mutation in the *mt-tRNA^{ALA}* gene. Single point values \pm SD. One-way ANOVA: clear versus light blue or clear versus dark blue, $p < 0.05$. Light blue vs dark blue values are not statistically different. (C) Using a laser capturing microscope, COX-competent (clear) and COX-deficient (dark blue) cells were isolated from *mt-tRNA^{ALA}* mice treated with vehicle, low (1×10^{12} vg) or a high (5×10^{12} vg) dose of mitochondrially targeted zinc finger nucleases. $N =$ at least 3 per group.

We proceeded to isolate the different areas using laser capture microdissection with subsequent pyrosequencing to assay the relative m.5024C>T mutation level within each region. Our results show a significant difference between the dark or light blue areas, compared to the clear areas (**Fig. 4.11B**). There was no statistically significant difference between the mutation loads in light versus dark blue areas, but the distribution suggests a greater variability in the mutation levels in the light blue areas. We demonstrate how the improved visibility of the NBTx reaction provides a robust and sensitive tool to study within-tissue heteroplasmy and the threshold to which pathologic mtDNA variants affect COX activity.

The NBTx was subsequently used to assess changes in the levels of COX deficiency after infusions of mitochondrially targeted zinc finger nucleases (mtZFNs). Engineered mtZFNs were specifically designed to target m.5024C>T mutation in the *mt-tRNA^{ALA}* mouse model so as to reduce its mutation load and test this approach as a

potential treatment strategy (Gammage et al 2014; Gammage et al 2018). Cardio-tropic adeno-associated virus (AAV9.45) was used as a vehicle and administered systemically to deliver mtZFNs to the host animal. After 65 days of recovery following tail-vein injection, animals were sacrificed and heteroplasmy levels in the heart were measured by pyrosequencing. Animals with high dose delivery showed a drastic drop in the m.5024C>T mutation load whereas low dose or vehicle had no effect (see **Table 3**).

Table 3: Mutation load changes after mtZFNs treatment

Animal #	Dose	Pre-treatment (mutation load in %)	Post-treatment (mutation load in %)
1	5 x 10 ¹² vg	81	45
2	5 x 10 ¹² vg	74	36
3	5 x 10 ¹² vg	68	40
4	5 x 10 ¹² vg	68	25
5	1 x 10 ¹² vg	80	75
6	1 x 10 ¹² vg	69	66
7	1 x 10 ¹² vg	73	72
8	1 x 10 ¹² vg	68	69
9	vehicle	67	72
10	vehicle	71	71
11	vehicle	68	69
12	vehicle	72	72
13	vehicle	74	74
14	vehicle	74	75
15	vehicle	75	74
16	vehicle	76	76
17	mt-tRNA ^{ALA} control	76	no treatment
18	mt-tRNA ^{ALA} control	75	no treatment
19	mt-tRNA ^{ALA} control	76	no treatment
20	mt-tRNA ^{ALA} control	73	no treatment
21	mt-tRNA ^{ALA} control	80	no treatment
22	mt-tRNA ^{ALA} control	78	no treatment
23	mt-tRNA ^{ALA} control	71	no treatment
24	mt-tRNA ^{ALA} control	70	no treatment
25	mt-tRNA ^{ALA} control	69	no treatment

Gammage and colleagues are reporting a successful reduction in heteroplasmy levels in favor of the wild-type variant. The heteroplasmy shift is accompanied by a significant increase in mt-tRNA^{ALA} steady-state levels. In addition, analysis of heart tissue revealed metabolomic signatures of a rebalancing between oxidative and glycolytic metabolism.

These signatures included elevated phosphoenol pyruvate and pyruvate levels, lower lactate levels, higher glucose levels and lower glucose-6-phosphate and fructose-6-phosphate levels. Despite the apparent successful reduction of mutant mtDNA from cardiac tissue and promising recovery of metabolic function, the NBTx histochemistry exposed the presence of persistent COX-deficient cells. We analyzed the intensity of formazan deposition after the NBTx reaction in mice of 3 distinct mutation loads (70 %, 75 %, and 80 %) to match those used for the mtZFNs treatment. We have found that mice of each group displayed a characteristic distribution of relative OD, reflecting the load of COX-deficient cells in each group (Figure 9). Based on this, we were able to predict where on the graph an animal of a certain mutation load would be found. Subsequently, we plotted the results from NBTx reacted hearts of mt-tRNA^{ALA} treated with low (1×10^{12} viral genomes (vg) per monomer per mouse) or high (5×10^{12} vg) doses and compared them with control animals (untreated animals or vehicle injection). We found that despite a high viral dose which shifted the heteroplasmy levels in favor of the wild-type mtDNA copy, similar or increased levels of COX-deficiency were measured (**Figure 4.12**). More surprisingly, mtZFNs induced reduction in m.5024C>T mutation was equally strong in COX-competent and COX-deficient areas, as measured by pyrosequencing (**Figure 4.11C**). The persistent COX deficiency in cells despite a strong reduction in mutant mtDNA load is not yet elucidated.

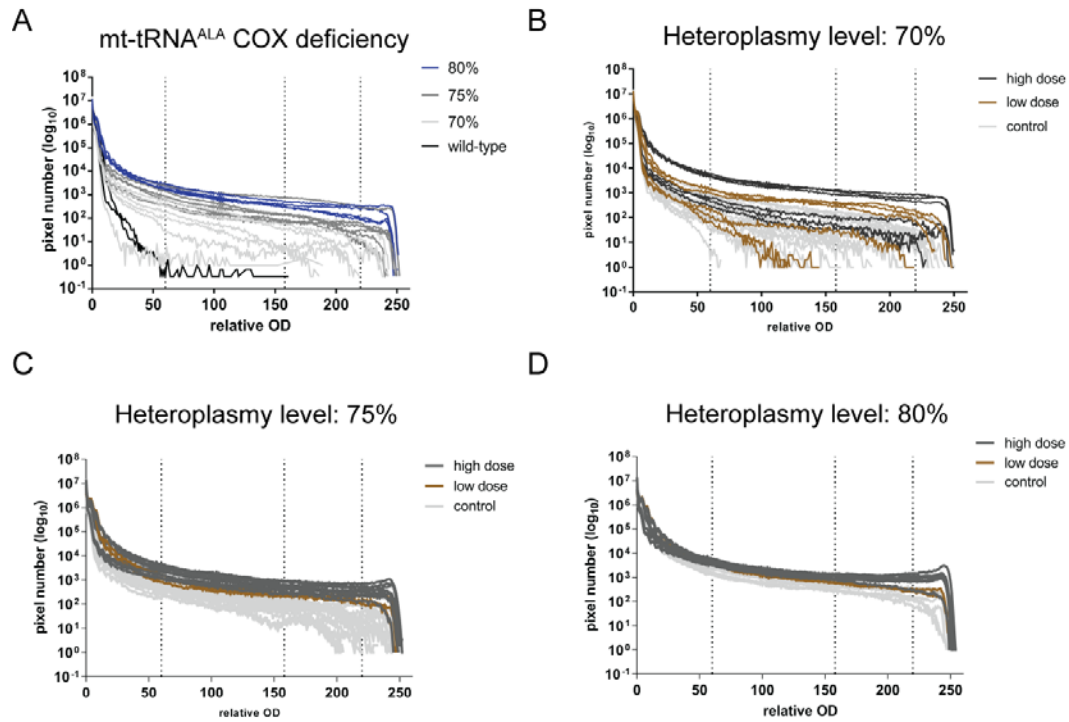


Figure 4.12 | Range of COX deficiency in the mt-tRNA^{ALA} heart. **(A)** Quantification of COX-deficient cells in mt-tRNA^{ALA} with 70, 75 and 80 % (± 2) mutation load. N = 2 controls, 5 at 70 %, 5 at 75 % and 4 at 80 %. Each line represents the mean value of 3 replicates. **(B)** Comparison of COX deficiency distribution between control and mtDNA ZFNs treated animals at 70 %, **(C)** 75 % and **(D)** 80 % mutation load. Each line is 1 of 3 replicate for each animal. 2 animals at low dose and 2 animals at high dose were used for the 70 % group and only one animal at low dose and high dose were used at the 75 % and the 80 %. Due to this low number of treated animals, no statistical analysis was performed.

1.26 NBTx assay in the brain

Brain tissues show great heterogeneity in the distribution of mitochondria which varies according to the type of cell and the area within the neuronal cell. It is therefore particularly difficult to use the current enzyme histochemical methods to expose COX-deficiency in neuronal tissue. Protocols that succeed in revealing COX-deficiency nevertheless come short to properly expose low or intermediate levels. We adapted the NBTx assay for brain tissue by evaluating the capacity to maintain colorless tissue in wild-type animals as well as being able to expose low levels of COX deficiency (**Figure 4.13, 4.14 and 4.15**).

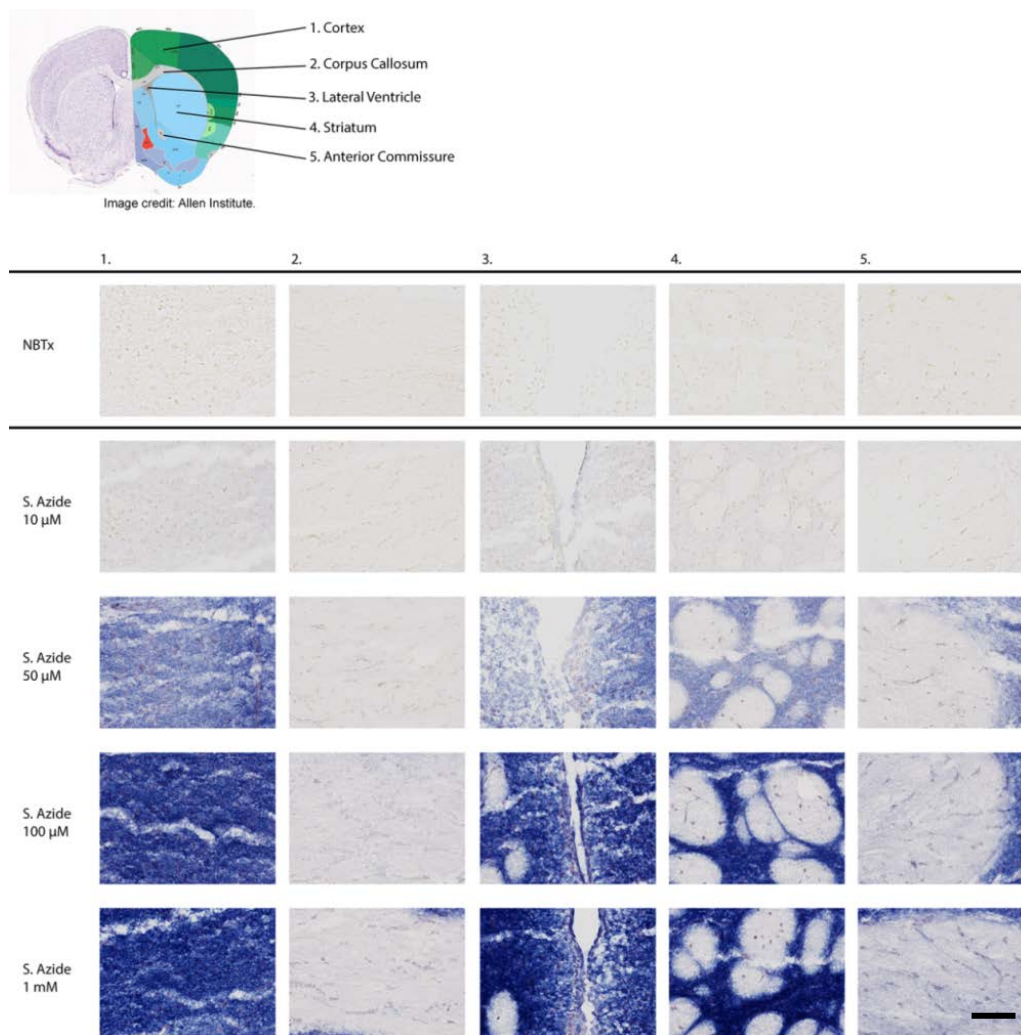


Figure 4.13 | Detection of COX-deficient cells in brain tissue: section 1. Coronal sections of young (12 weeks) male mouse brain corresponding to frontal area where the following structures are identified: 1. Cortex, 2. Corpus callosum, 3. Lateral ventricle, 4. Striatum, 5. Anterior commissure. 10 μm thick sections reacted using the NBTx protocol or SDH activity with partial or full inhibition of COX activity with sodium azide. 30 minutes incubation at 25°C. Representative images of 3 replicates. Scale bar 50 μm .

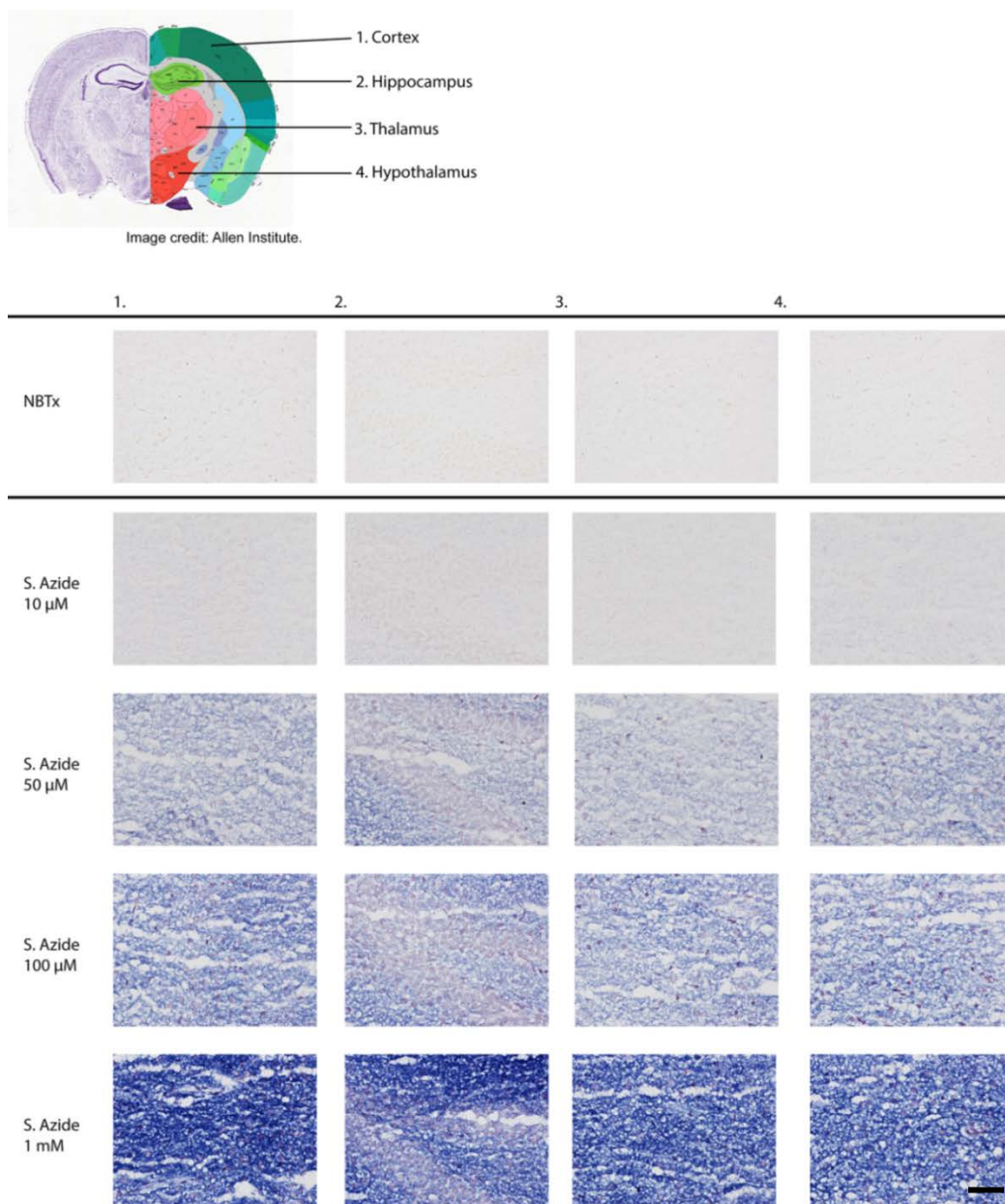


Figure 4.14 | Detection of COX-deficient cells in brain tissue: section 2. The following structures are identified: 1. Cortex, 2. Hippocampus, 3. Thalamus, 4. Hypothalamus. 10 μm thick sections reacted using the NBTx protocol or SDH activity with partial or full inhibition of COX activity with sodium azide. 30 minutes incubation at 25°C. Representative images of 3 replicates. Scale bar 50 μm .

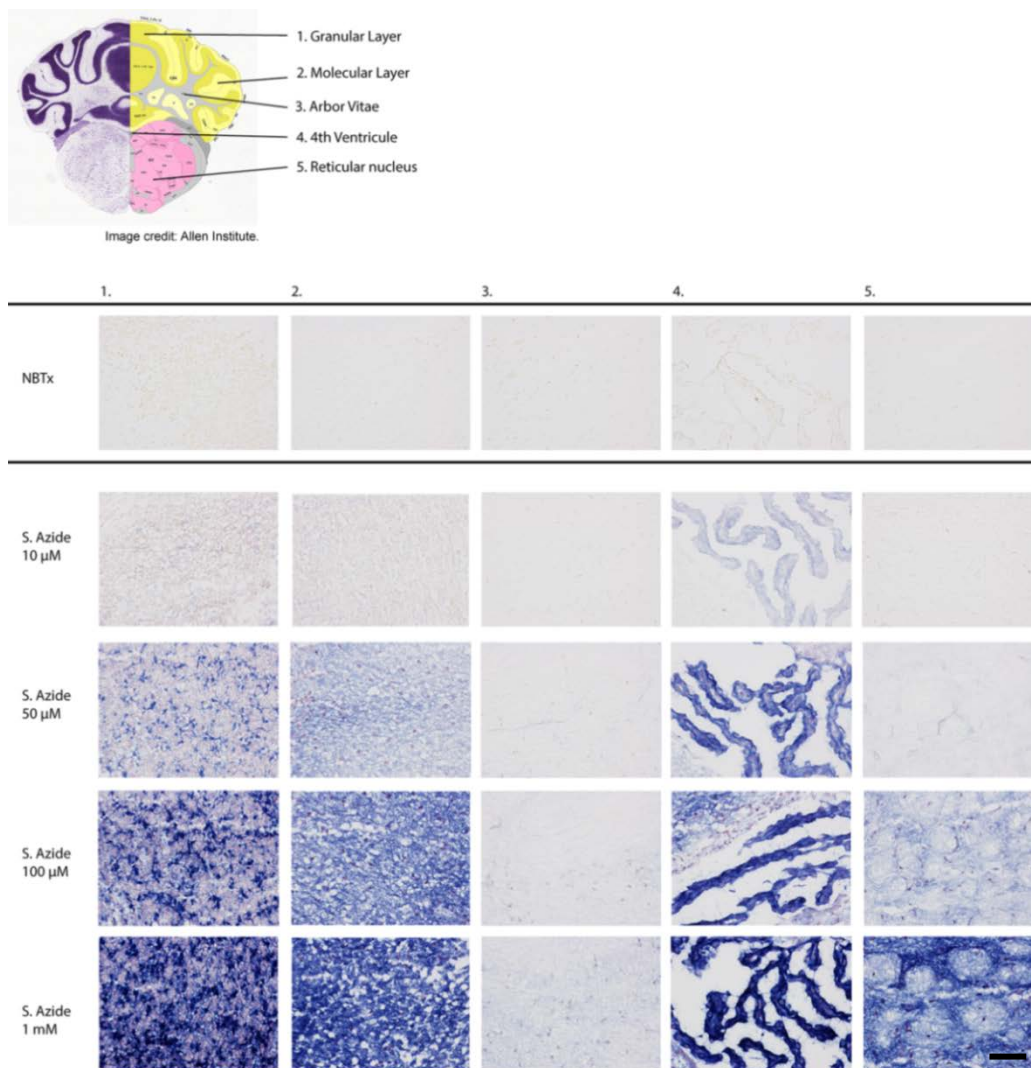


Figure 4.15 | Detection of COX-deficient cells in brain tissue: section 3. The following structures within the cerebellum are identified: 1. Granular layer, 2. Molecular layer, 3. Arbor vites, 4. 4th ventricle, 5. Reticular nucleus. 10 µm thick sections reacted using the NBTx protocol or SDH activity with partial or full inhibition of COX activity with sodium azide. 30 minutes incubation at 25°C. Representative images of 3 replicates. Scale bar 50 µm.

The NBTx assay in brain sections of different mouse models displaying various levels of COX deficiency was tested and compared to COX/SDH histochemical method. The *Surf1* knockout revealed an easily observable deposition of blue pigments across the tissue (**Figure 4.16A,B**), whereas we found serial sections of control and mutant brain sections after a COX/SDH reaction difficult to analyze (**Figure 4.16A,B** second panel). The color is, as seen in the heart, similar to what one would see if the DAB incubation is insufficient to block all of the SDH activity in normal brain controls (**Figure 4.16A**, 20 minutes COX, third panel). Within these sections, it appears as though brown deposits within functional mitochondria are mixed with blue deficient mitochondria, rendering the coloration of *Surf1* knockout brain sections difficult to interpret. There was no ambiguity with the NBTx assay; detection of COX-deficient cells against the background of COX-functional cells that lack any coloration provided excellent contrast.

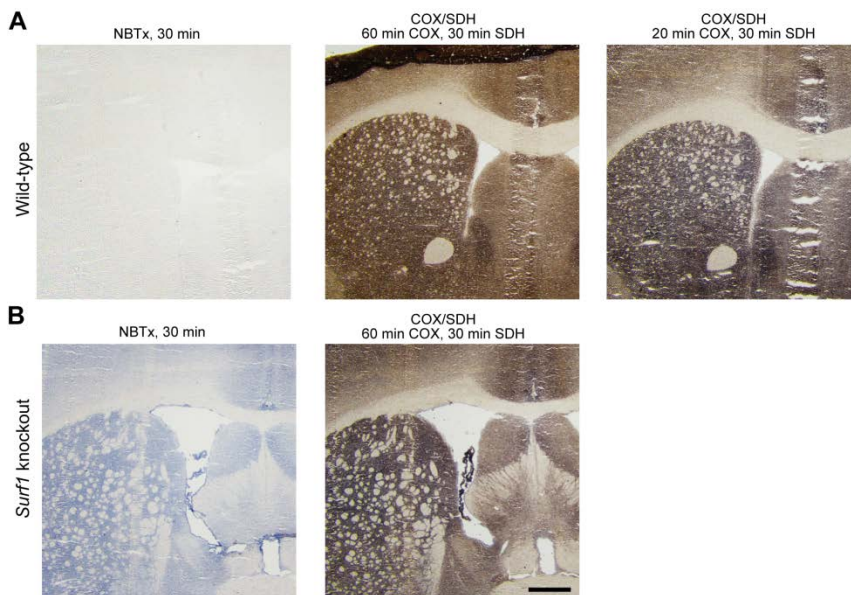


Figure 4.16 | NBTx assay in brain tissue of *Surf1* knockout mice. (a) Brain sections of wild-type mice are shown reacted either with the NBTx or the COX/SDH histochemical method. (b) Consecutive section of brain *Surf1* knockout mice (n = 3). Scale bar, 500 μ m.

The NBTx assay also proved efficient in mouse models where COX deficiency is not general but specific to targeted areas. For example, we used the *Dars2*^{NEKO} mutant expressing Cre recombinase under the calcium/calmodulin-dependent kinase II alpha promoter (CaMKII α -Cre). Depletion of the DARS2 protein in this model is targeted to forebrain, hippocampal and striatum neurons (Arandjanski et al. 2017). *Dars2* gene encodes for the mitochondrially expressed aspartyl-tRNA synthetase and is linked to severe mitochondrial dysfunction in humans (Scheper et al. 2007). The NBTx reveals substantial COX deficiency in 15 weeks old animals in hippocampal and cortical neurons (**Figure 4.17**), as it was previously shown with the sequential COX/SDH reactions (Arandjanski et al. 2017).

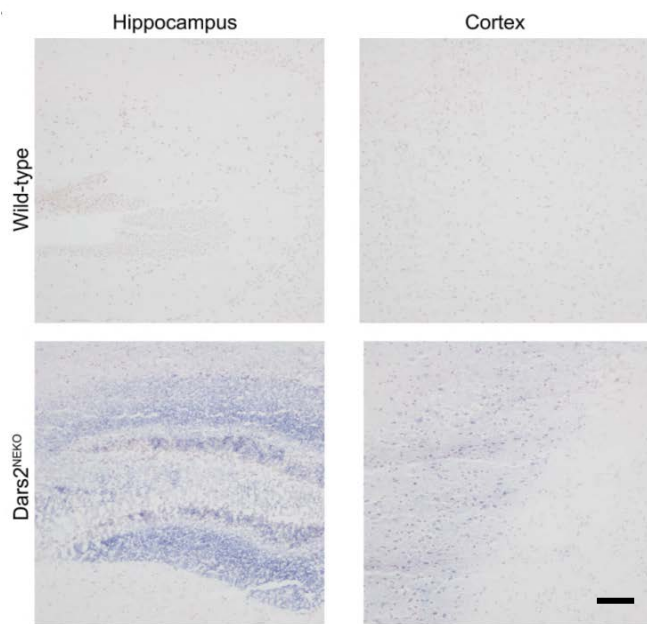


Figure 4.17 | NBTx assay in conditional knockout mouse models. Brain sections of wild-type mice remain clear in the hippocampus or the cortex area. *Dars2*^{NEKO} mice on the other hand display strong formazan deposition. NBTx reaction, 1h at 25°C. representative images of 2 wild-type and 2 *Dars2*^{NEKO} mice. Scale bar 50 μ m.

One caveat with performing the NBTx assay is the assumption that a certain amount of mitochondrial activity is present in the tissue. The intensity of blue formazan deposition is proportional to the amount of Complex II molecules paired to a deficient Complex IV. Severe mitochondrial defects though can lead not only to a detectable OXPHOS deficiency but also to the loss of mtDNA and eventually cell death. For this reason, in tissues with low baseline levels of mitochondrial activity, the presence of disease causing genetic defects might render the mitochondrial activity critically low, making detection difficult.

To assess the limitations of the NBTx assay, we looked at the MitoPark mouse model where the knockout of the nucleus encoded mitochondrial transcription factor A (*Tfam*) gene in dopamine neurons leads to the reduction of mtDNA copy number with a severe respiratory chain dysfunction and a progressive loss of dopamine neurons in the midbrain (Ekstrand et al. 2007, Ekstrand & Galter 2009). Deficiency could not be detected with a standard NBTx assay, even after one hour incubation. We struggled equally to detect deficiency using the standard COX/SDH protocol. In this mouse model, it is reasonable to speculate that COX deficiency remains undetected because of a critically low level of mitochondrial activity and neuronal cell death. Indeed, deficient mitochondria were finally detected by changing the protocol to a long incubation of 2 hours (with a change of solution after the first hour), which suggest that the overall mitochondrial activity in this model is low due to impaired mitochondrial biogenesis and cell death. This was consistent with the incubation time also needed for the COX/SDH assay to reveal COX-deficient cells (**Figure 4.18**). This later set of data highlights the importance of considering mitochondrial content and cell death when interpreting negative data. The successful application of a considerably longer incubation time is, on the other hand, a good demonstration of the versatility and potential of the NBTx assay.

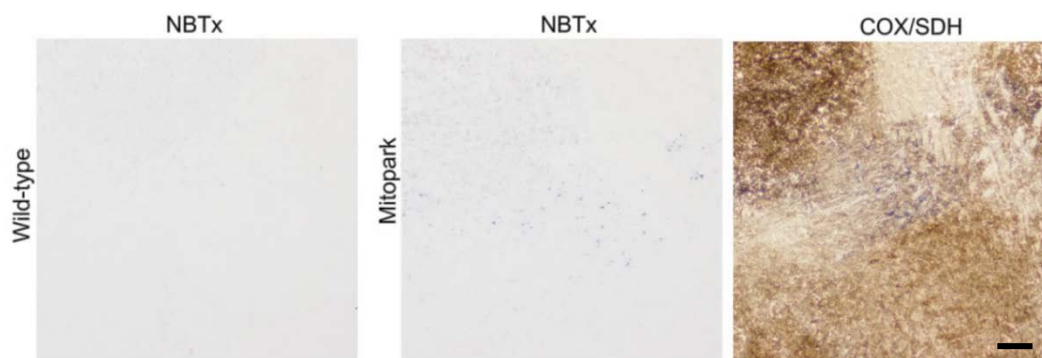


Figure 18 | NBTx assay in conditional knockout mouse models. Sections of midbrain area from wild-type or MitoPark mice reacted 2 hours in NBTx medium. Last panel shows midbrain of MitoPark mice after serial COX/SDH reaction (60 minutes in DAB solution followed by 2 hours in SDH solution). N = 3, Scale bar, 50 μ m.

We proceeded with the evaluation of a few other mouse organs which are commonly used in our laboratories as an example of how various tissues respond to the NBTx assay. Deficient COX activity is easily revealed in colonic crypts (**Figure 4.19**, first panel, *PolgA^{D257A}* mtDNA mutator mice) and in skeletal muscles (**Figure 4.19**, second panel, *Surf1* knockout mice). Furthermore, small developing sperm cells in the testis were also successfully detected with the NBTx method (**Figure 4.19**, third panel, *PolgA^{D257A}* mtDNA mutator mice). In the latter, a strong pink discoloration is easily recognizable. This additional pinkish color was seen in all tissue tested and is interpreted as a half-reduced intermediate which is partly washed away in ethanol (Nachlas et al. 1956, Altman 1976).

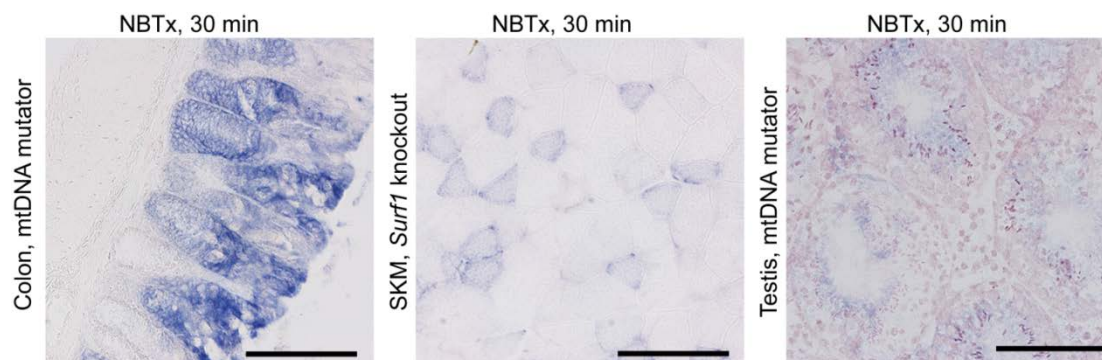


Figure 4.19 | NBTx assay on various mouse tissues. Detection of COX-deficient mitochondria was possible with several tissues taken from either mtDNA mutator mice or *Surf1* knockout mice. First panel: colon, second panel: skeletal muscle, third panel: testis. Fresh frozen sections were cut at 10 μm and incubated for 30 minutes at 25°C. N = 3 per tissue, Scale bar, 100 μm .

Lastly we attempted to apply the NBTx assay on skin tissue. As anticipated, wild-type skin tissue remains clear and the mitochondrial activity is detected with formazan deposition in tissue treated with sodium azide (**Figure 4.20A**). Nevertheless, not all areas of wild-type skin tissue remain clear. Some significant amount of formazan is catalyzed despite the lack of COX deficiency in the wild-type tissue (**Figure 4.20B**). The reason for this unspecific deposition of formazan is unknown. One possible explanation is the composition of skin tissue which might interfere with proper diffusion of the reactants. Such conditions are not optimal and interfere with the interpretation of a positive signal in genetically modified animals.

Overall, we were able to successfully distinguish COX-functional and COX-dysfunctional regions using the single step NBTx assay in a variety of tissue types. As the concentration of respiratory complexes varies between tissues, incubation conditions need to be adjusted accordingly. For each organ, the correct incubation time and temperature is established by reacting wild-type tissue and assessing the best parameters to maintain a colorless tissue, indicating efficient PMS to COX electron

transfer. Additionally, incubation in SDH solution (1mM sodium azide to block all COX activity) provides information as to the maximum formazan deposition in a given tissue and whether the chosen incubation time and temperature is sufficient to expose slight decreases in COX activity (see full protocol **Appendix C**).

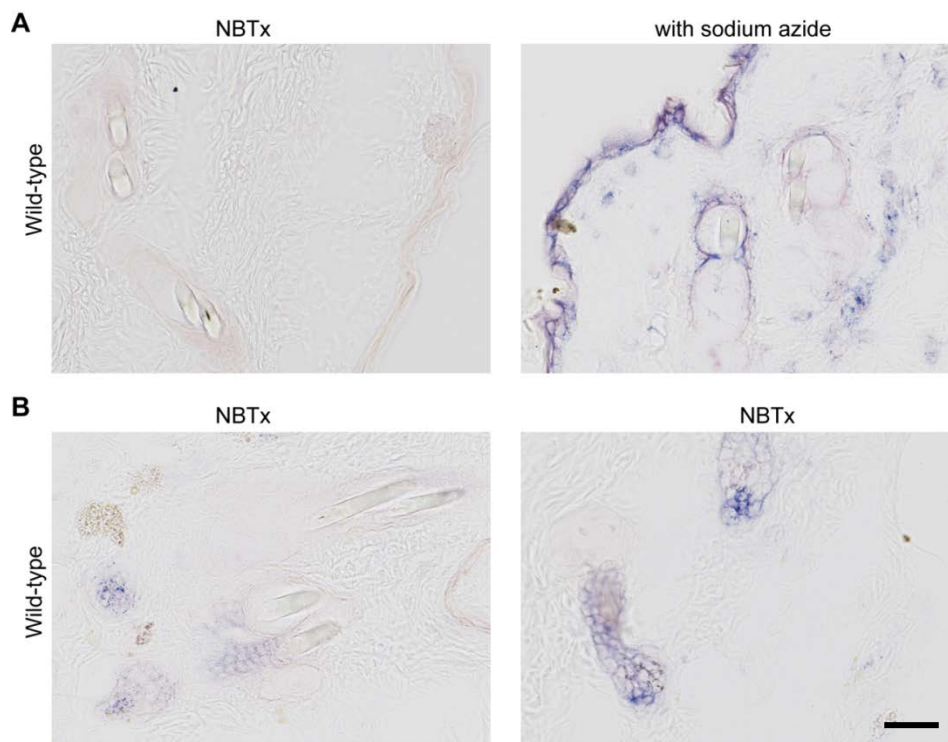


Figure 4.20 | NBTx assay in skin tissue. (A) Mouse skin tissue after NBTx assay (left panel) or SDH activity measured with the addition of sodium azide in the NBTx solution (right panel). (B) Sections of skin tissue from wild-type animal showing formazan deposition despite the presumed healthy mitochondria. Representative images of 3 replicates. Scale bar 50 μm

1.27 The application of the NBTx assay to study *Drosophila melanogaster*

The fruit fly *Drosophila melanogaster* is becoming more commonly used as an alternative animal model for mitochondrial research (Sánchez-Martínez et al. 2006). We therefore applied the NBTx reaction to the detection of mitochondrial COX activity in muscle sections from the fly thorax. Wild-type flies, as well as two different genetically engineered models were investigated. The fly *Lrpprc2* gene is one of two homologs of the mouse *Lrpprc* gene also involved in coordinating mitochondrial gene translation. Manipulation of the *Lrpprc2* knockout or knockdown leads to a drastic loss of respiratory chain complexes (Baggio et al. 2014). The DmPol γ A flies are flies trans-complementing two deleterious mitochondrial polymerase gamma mutant alleles (the exo- deficient *PolgA^{D257A}* and the processivity impairing *PolgA^{H1134A}* alleles), which present no pathogenic phenotype (Bratic et al. 2015). However using the NBTx assay, we were able to observe mild deficiency in COX activity. The high Complex IV content in the fly thoracic muscles require a short incubation time of only 10 minutes at 18°C to allow strong formazan deposition in the *Lrpprc2* RNAi fly. DmPol γ A muscles had only minimal formazan deposition, whereas wild-type healthy muscles remained colorless under these conditions (**Figure 4.21**).

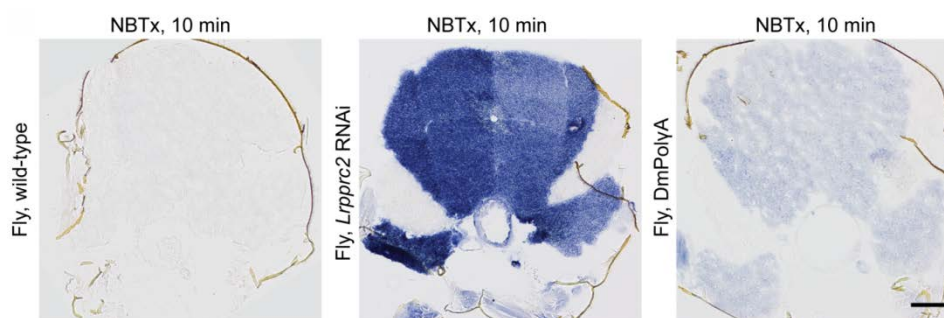


Figure 4.21 | Skeletal muscles from the thorax of *Drosophila melanogaster* stained for 10 minutes at 18 °C. Representative images of 5 flies per genotype. Scale bar, 100 μ m.

1.28 NBTx Assay in Human Diagnostics

The sequential COX/SDH histochemical assay is universally-applied in pathology laboratories as part of the diagnostic work-up of human tissue, including muscle biopsies, to identify COX deficient cells (Alston et al. 2016). To test the applicability of the NBTx method in human diagnostics, we compared serial sections of NBTx images against sequential COX/SDH and COX-only reactions for a variety of human biopsy samples, (**Figure 4.22**). Seven distinct genotypes were used to evaluate human skeletal muscles as well as seven samples of heart tissues (**Figure 4.23 and 4.24**). We found that regardless of the genetic defect (mtDNA mutations **Figure 4.22A** or nuclear gene mutations **Figure 4.22B and 4.22C**) the NBTx successfully exposed the full range of COX-deficient cells, as predicted from the COX/SDH sections, with the advantage that low and intermediate levels of dysfunction were distinguished with a quantifiable variation in blue intensity. In contrast to the classical COX/SDH reaction, the NBTx assay does not identify cells with functional mitochondria, regardless of the COX activity level (**Figure 4.22A** marked I and II) but, as seen in the mouse, reveals dysfunctional COX activity with the accumulation of blue formazan pigments with varying intensity (**Figure 4.22A** marked III, IV and V). Thus, NBTx successfully detected COX-deficient cells in all three types of tissue, in patterns consistent with the COX/SDH method. These data show that the NBTx assay is suitable for human diagnostic work, revealing high-contrast sections that allow for quantification and rapid diagnosis.

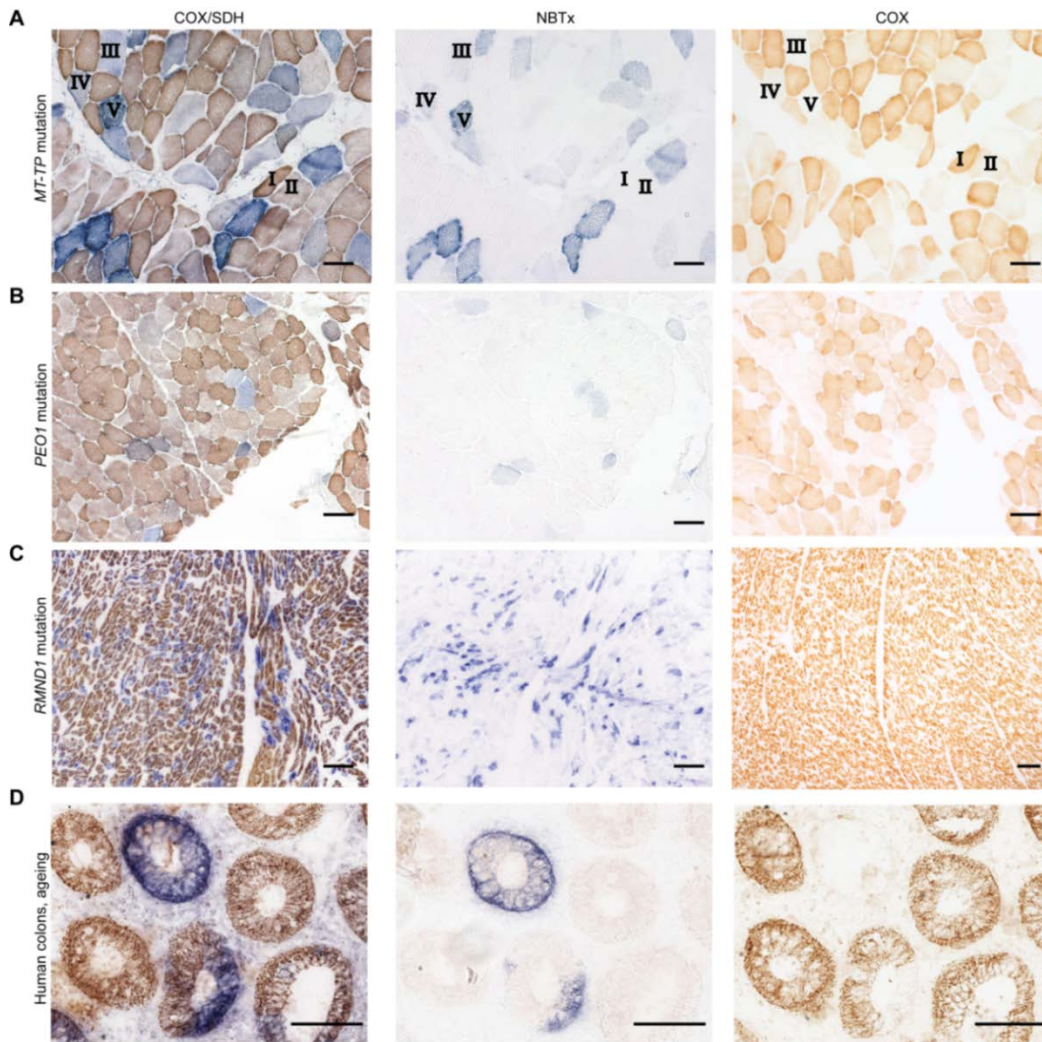


Figure 4.22. Human tissues analyzed using COX/SDH, NBTx or COX histochemical methods. (A) Skeletal muscle tissue with a novel m.16015T>C *MTTP* mutation. Roman numerals point to individual cells with: I) no COX deficiency, high COX activity, II) no COX deficiency, low COX activity III) mild COX deficiency, low SDH activity levels, IV) mild COX deficiency, mild SDH activity levels, V) strong COX deficiency, high SDH activity levels. (B) Section of skeletal muscle from patient with identified nuclear gene p.(Arg371Trp) *TWINK* (formerly *PEO1*) mutation. (C) Human heart tissue, p.Asn238Ser;c.829_830+2her_delGAGT *RMND1* mutations. (D) Sections of colonic tissue from patient with no known mitochondrial disease. COX-deficient colonic crypts are detected in elderly patients. (n = 2, 78 and 72 years old). Scale bar, 100 μ m.

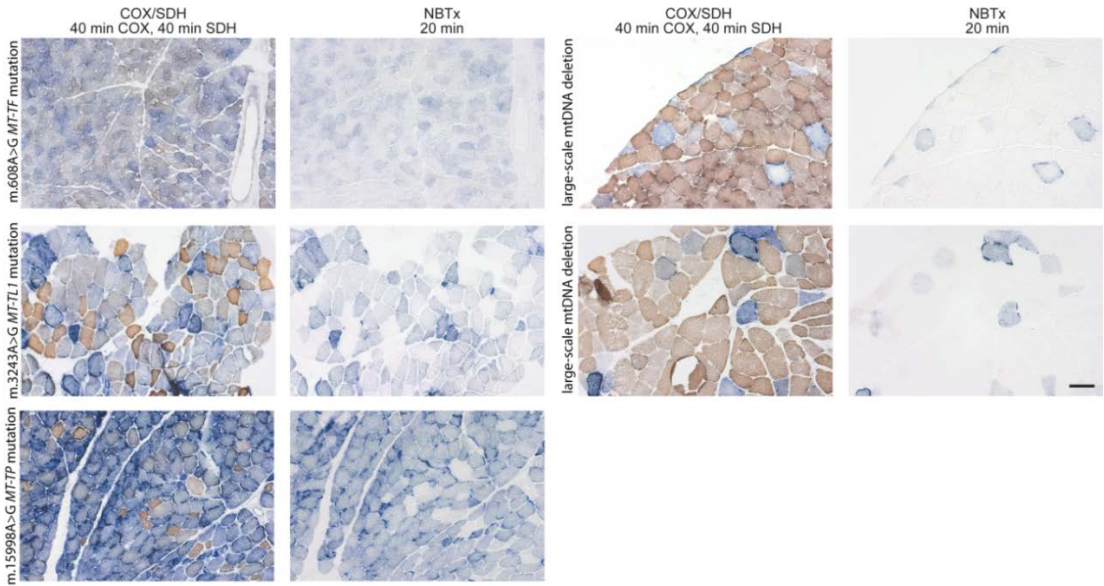


Figure 4.23 | Skeletal muscle sections from patients with various genetic background. Tissue was cut at 10 µm and consecutive slides were used for comparing COX/SDH to the new NBTx method. Scale bar, 100 µm.

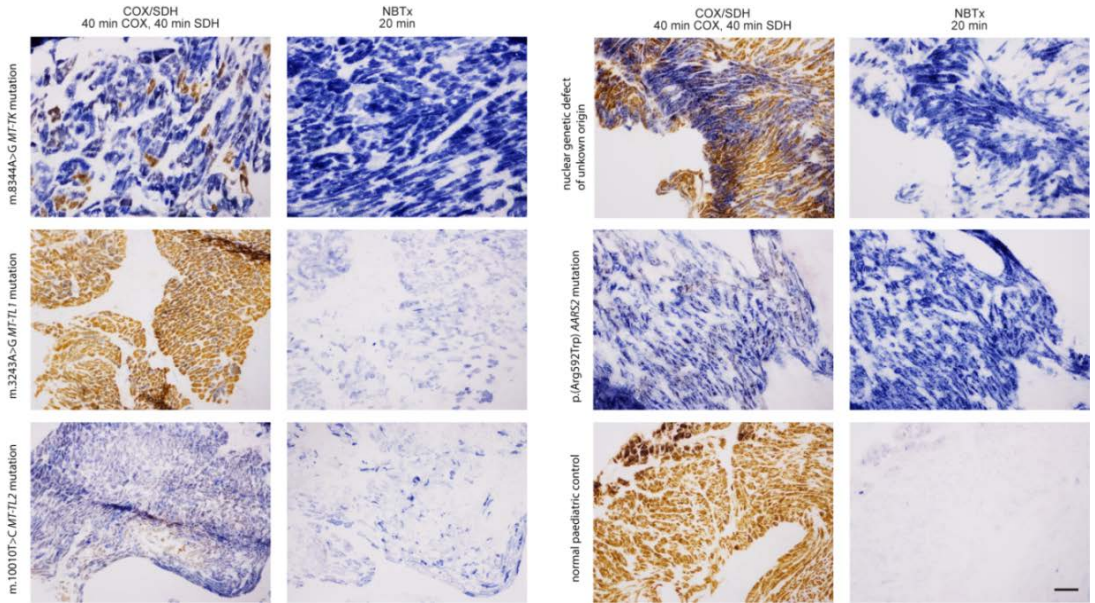


Figure 4.24 | Heart tissues from patients with various genetic background. Tissue was cut at 10 µm and consecutive slides were used for comparing COX/SDH to the new NBTx method. Scale bar, 100 µm.

DISCUSSION

Accurately quantifying COX impairment at the cellular level will contribute to understand the role of respiratory chain defects in mitochondrial disease processes and the implication of mitochondrial dysfunction in age-related diseases. The currently available methods for cell specific detection, like the COX-only histochemistry, immunolabeling of mitochondrial complex subunits or the sequential COX/SDH assay, involve either many steps or are limited to detection of high levels of COX deficiency, failing to clearly expose low or intermediate levels. Detecting deficiencies with the COX-only histochemistry or by using immunohistochemistry methods is achieved through the interpretation of a reduction in signal – indicating a poor COX activity – but since COX activity naturally varies between cells or sections of cell bodies, mild COX deficiencies cannot be ascertain with the use of those methods. As a direct visualization of deficient COX activity, the sequential COX/SDH method improves the quantification of dysfunctional cells. By highlighting areas of reduced COX activity with formazan deposition (blue) in addition to revealing positive COX activity with DAB oxidation (brown), the COX/SDH method also comes short in clearly detecting mild dysfunction.

The core of this work was to show that deficiency in cytochrome *c* oxidase activity can be detected with the simple reduction of NBT. It was demonstrated that the NBTx method exploits tightly competing biochemical interactions between PMS, NBT and Complex IV to evaluate the integrity of COX activity in an enzyme histochemical assay. Compare to the sequential COX/SDH reactions, the NBTx has the advantage of not requiring a double staining and eliminates the need for DAB. The presence of DAB has been reported to interfere with certain assays, such as real-time qPCR (Murphy et al. 2012) and therefore, the capacity to reveal COX deficient cells without DAB is advantageous in many ways. The NBTx assay generates images with a high-contrast between COX-deficient and COX-competent cells and not only reduces the overall cost; it is quick, and allows clear identification of cells harboring even mildly COX-deficient mitochondria. This single-color reaction has the added advantage that simple

automation and quantitative analysis are possible, without having to rely on comparing activity levels between samples.

The biological process driving the segregation of mutant mtDNA variants in some cells and not others, creating the typical mosaic distribution of COX-deficient cells across tissues, remains an important question to which there are currently no definite answers. As we demonstrated in the skeletal muscles of mtDNA mutator mice, individual fibers show COX deficiency with a variable intensity. With the acquisition of quantifiable data with the NBTx assay and, subsequently our ability to quantify fiber cell individually, we were able to distinguish the overall greater burden of COX-deficiency in oxidative type II fibers compared to glycolytic fibers. This degree of precision, to the best of our knowledge, had not been previously achieved. In addition, the sensitivity of the NBTx assay to low or intermediate levels of COX-deficiency made it possible to quantify the loss of COX activity in heart tissues of tRNA^{ALA} mice. This is a model with a single pathologic mtDNA mutation; an opportunity to study in vivo the distribution patterns of the mtDNA variants (heteroplasmy levels between tissues) as well as the consequences over the animal life span on the OXPHOS system and possibly on other mitochondrial functions. The ease at which cellular COX dysfunction was revealed and the detection of the full spectrum of deficiency with the NBTx assay permitted to establish that the COX deficiency burden within the heart of tRNA^{ALA} mice is predictable within a certain range based on the animal's mutant mtDNA heteroplasmy level (see Figure 4.12). This surprising predictability opens up new avenues to address the complexing ways by which mutant mtDNA variants behave and their effect on COX activity in single cells. The NBTx assay will be advantageous in studying COX deficiencies in age-related mitochondrial diseases and in investigations of environmental factors or genetic backgrounds where their contribution to the clinical manifestations remains difficult to establish. Additionally, as shown here, the precision with which we were able to quantify COX deficiencies in tRNA^{ALA} mice enabled us to confidently evaluate the impact of a newly developed treatment: the injection of engineered mtZFNs

to eliminate the mutant variants. Hopefully more such attempts to find effective treatments can be supported by the NBTx assay in the future.

The one-step NBTx assay eliminates the confounding results observed with the sequential COX/SDH reaction of intermediate COX deficiency (Murphy et al. 2012). Unarguably, the strong contrast of blue COX-deficient cells over a clear background of fully-functional cells in the NBTx assay offers an improvement on previous methods. Our results on brain sections of *Surf1* constitutive KO mice illustrate how intermediate levels of COX activity are easily identified. Beyond primary mitochondrial disease, loss of mitochondrial activity in the brain is a domain of investigation in normal ageing processes or age-related diseases such as Alzheimer's or Parkinson's disease (Navarro & Boveris 2006; Boveris & Navarro 2008; Swerdlow 2011). Reduction of COX activity in aged brain tissue has been reported in humans, rodents or monkeys using COX cytochemical or immunohistochemical methods (Itoh et al. 1996; Bertoni-Freddari et al. 2004; Navarro et al. 2002). Analysis of DAB accumulation or detection of immunolabeled Complex IV subunits is challenging because it requires imaging at very precise brain area and comparing those areas between samples. This limits the field of view to precisely where investigators make their measurements and given the heterogeneous distribution of mitochondrial activity in the brain, assessment of a loss of enzyme activity in the nervous system is difficult. Detection of COX-deficient cells in genetic models with neuron targeted gene knockouts, like the *Dars2*^{NEKO} or the Mitopark model, showed that the NBTx assay can be adapted to several models which display either strong COX deficiency (easily detectable and quantifiable) or in severe mitochondrial activity loss.

Based on the successful identification of COX deficiency in human tissues of a wide range of genetic background, we set the basis for establishing the NBTx within the diagnostic workflow. Although other approaches such as the COX/SDH, COX-only histochemistry or immunohistochemistry are routinely used and appreciated by

clinicians and pathologists, the new NBTx assay stands out as a new alternative to reveal the wider spectrum of COX-deficiency within a tissue.

The new NBTx assay is a strong complimentary tool to assess deficient COX activity for a variety of mouse or human tissues and smaller model organisms such as the fly, *Drosophila melanogaster*. In addition, we showed the potential for the acquisition of quantitative data, which will support research on mitochondrial disease mechanisms and also in the evaluation of therapeutic approaches and anticipate that the advantages of this method will benefit many in the field of mitochondrial research. This new assay not only gives an accurate readout of deficiency, it is the first enzyme histochemistry assay that exploits not a single enzyme activity but rather, the ratio of activity between 2 enzymes connected within one biochemical pathway. As such, the NBTx assay is of benefit for the field of mitochondrial biology research but also introduces a new avenue for the development of new enzyme histochemistry assays.

References

Agostino, A. et al., 2003. Constitutive knockout of Surf1 is associated with high embryonic lethality, mitochondrial disease and cytochrome c oxidase deficiency in mice. *Human Molecular Genetics*, 12(4), pp.399–413.

Allen, J.F., 2015. Why chloroplasts and mitochondria retain their own genomes and genetic systems: colocation for redox regulation of gene expression. *Proceedings of the National Academy of Sciences of the United States of America*, 112(33), pp.10231-10238.

Alston, C.L. et al., 2016. The genetics and pathology of mitochondrial disease. *The Journal of Pathology*, 241(2), pp.236–250.

Altman, F.P., 1976. Tetrazolium salts and formazans. *Progress in histochemistry and cytochemistry*, 9(3), pp.1–56.

Antonieli, M. et al., 2014. The oligomycin-sensitivity conferring protein of mitochondrial ATP synthase: emerging new roles in mitochondrial pathophysiology. *International Journal of Molecular Sciences*, 15(5), pp.7513-7536.

Aradjanski, M. et al., 2017. DARS2 protects against neuroinflammation and apoptotic neuronal loss, but is dispensable for myelin producing cells. *Human Molecular Genetics*, 26(21), pp.4181–4189.

Baggio, F. et al., 2014. Drosophila melanogaster LRPPRC2 is involved in coordination of mitochondrial translation. *Nucleic acids research*, 42(22), pp.13920–13938.

Baines, H.L. et al., 2014. Similar patterns of clonally expanded somatic mtDNA mutations in the colon of heterozygous mtDNA mutator mice and ageing humans. *Mechanisms of ageing and development*, 139, pp.22–30.

Bertoni-Freddari, C. et al., 2004. Cytochrome oxidase activity in hippocampal synaptic mitochondria during aging: a quantitative cytochemical investigation. *Annals of the New York Academy of Sciences*, 1019, pp.33–36.

Bogenhagen, D. & Clayton, D.A., 1974. The number of mitochondrial deoxyribonucleic acid genomes in mouse L and human HeLa cells. Quantitative isolation of mitochondrial deoxyribonucleic acid. *The Journal of Biological Chemistry*, 249(24), pp.7991–7995.

Boveris, A. & Navarro, A., 2008. Brain mitochondrial dysfunction in aging. *IUBMB life*, 60(5), pp.308–314.

Brandt et al., 2017. Changes of mitochondrial ultrastructure and function during ageing in mice and Drosophila. *eLife*, 6, e24662.

- Bratic, A. et al., 2015. Complementation between polymerase- and exonuclease-deficient mitochondrial DNA polymerase mutants in genomically engineered flies. *Nature communications*, 6, p.8808.
- Brière, J.J., et al., 2004. Respiratory chain defects: what do we know for sure about their consequences in vivo? *Biochemica et Biophysica Acta* 1659, pp.172-177.
- Brody, I.A. & Engel, W.K., 1964. Effects of phenazine methosulfate in histochemistry. *Journal of Histochemistry & Cytochemistry*, 12(12), pp.928-929.
- Brown, D.T. et al., 2001. Random genetic drift determines the level of mutant mtDNA in human primary oocytes. *American journal of human genetics*, 68(2), pp.533-536.
- Burgoyne, R.D., 2007. Neuronal calcium sensor proteins: generating diversity in neuronal Ca²⁺ signalling. *Nature reviews. Neuroscience*, 8(3), pp.182-193.
- Calvo, S.E., Clauser, K.S., Mootha, V.K., 2016. MitoCarta2.0: an updated inventory of mammalian mitochondrial proteins. *Nucleic Acids Research*, 44, pp. D1251-D1257.
- Cedergren R. et al., 1988. The evolutionary relationships among known life forms. *Journal of Molecular Evolution*, 28, pp.98-112.
- Chandel, N.S., Budinger, G.R. & Schumacker, P.T., 1996. Molecular oxygen modulates cytochrome c oxidase function. *The Journal of Biological Chemistry*, 271(31), pp.18672-18677.
- Chen, H. et al., 2003. Mitofusins Mfn1 and Mfn2 coordinately regulate mitochondrial fusion and are essential for embryonic development. *The Journal of Cell Biology*, 160(2), pp.189-200.
- Chen, X. et al., 1995. Rearranged mitochondrial genomes are present in human oocytes. *American journal of human genetics*, 57(2), pp.239-247.
- Clapham, D.E., 2007. Calcium signaling. *Cell*, 131(6), pp.1047-1058.
- Cohn, A.C. et al., 2007. Autosomal dominant optic atrophy: penetrance and expressivity in patients with OPA1 mutations. *American journal of ophthalmology*, 143(4), pp.656-662.
- Dell'agnello, C. et al., 2007. Increased longevity and refractoriness to Ca²⁺-dependent neurodegeneration in Surf1 knockout mice. *Human Molecular Genetics*, 16(4), pp.431-444.
- Dolmetsch, R.E., Xu, K. & Lewis, R.S., 1998. Calcium oscillations increase the efficiency and specificity of gene expression. *Nature*, 392(6679), pp.933-936.

- Ekstrand, M.I. & Galter, D., 2009. The MitoPark Mouse - an animal model of Parkinson's disease with impaired respiratory chain function in dopamine neurons. *Parkinsonism & related disorders*, 15 Suppl 3, pp.S185–8.
- Ekstrand, M.I. et al., 2007. Progressive parkinsonism in mice with respiratory-chain-deficient dopamine neurons. *Proceedings of the National Academy of Sciences of the United States of America*, 104(4), pp.1325–1330.
- El-Khoury, R. et al., 2013. Engineering the alternative oxidase gene to better understand and counteract mitochondrial defects: state of the art and perspectives. *British Journal of Pharmacology*, 171, pp.2243–2249.
- Ernster, L. & Schatz, G., 1981. Mitochondria: a historical review. *The Journal of Cell Biology*, 91(3 Pt 2), pp.227s–255s.
- Farber, E. & Bueding, E., 1956. Histochemical localization of specific oxidative enzymes. V. The dissociation of succinic dehydrogenase from carriers by lipase and the specific histochemical localization of the dehydrogenase with phenazine methosulfate and tetrazolium salts. *Journal of Histochemistry & Cytochemistry*, 4(4), pp.357–362.
- Favaloro, B. et al., 2012. Role of Apoptosis in disease. *Aging*, 4(5), p.330.
- Finsterer, J., 2004. Mitochondriopathies. *European journal of neurology*, 11(3), pp.163–186.
- Gammage, P.A. et al., 2014. Mitochondrially targeted ZFNs for selective degradation of pathogenic mitochondrial genomes bearing large-scale deletions or point mutations. *EMBO molecular medicine*, 6(4), pp.458–466.
- Gammage, P.A. et al., 2018. Genome editing in mitochondria corrects a pathogenic mtDNA mutation *in vivo*. *Nature Medicine*, in revision.
- Gomes, L.C., Di Benedetto, G. & Scorrano, L., 2011. During autophagy mitochondria elongate, are spared from degradation and sustain cell viability. *Nature cell biology*, 13(5), pp.589–598.
- Gonzalez-Lima, F. & Jones, D., 1994. Quantitative mapping of cytochrome oxidase activity in the central auditory system of the gerbil: a study with calibrated activity standards and metal-intensified histochemistry. *Brain Research*, 660(1), pp.34–49.
- Gorman, G.S. et al., 2016. Mitochondrial diseases. *Nature reviews. Disease primers*, 2, p.16080.
- Gray, M.W., 2017. Lynn Margulis and the endosymbiont hypothesis: 50 years later. *Molecular biology of the cell*, 28(10), pp.1285–1287.
- Gray, M.W., 1999. Mitochondrial Evolution. *Science*, 283(5407), p.1476.

- Gray, M.W., 2012. Mitochondrial evolution. *Cold Spring Harbor perspectives in biology*, 4(9), p.a011403.
- Gray, M.W., Burger, G. & Lang, B.F., 2001. The origin and early evolution of mitochondria. *Genome biology*, 2(6), pp.1018.1–1018.5.
- Green, D.E. & Beinert, H., 1955. Biological Oxidations. *Annual Review of Biochemistry*, 24(1), p.1.
- Grünewald, A. et al., 2014. Quantitative quadruple-label immunofluorescence of mitochondrial and cytoplasmic proteins in single neurons from human midbrain tissue. *Journal of neuroscience methods*, 232, pp.143–149.
- Gustafsson, C.M., Falkenberg, M. & Larsson, N.-G., 2016. Maintenance and Expression of Mammalian Mitochondrial DNA. *Annual Review of Biochemistry*, 85, pp.133–160.
- Hajnóczky, G. et al., 1995. Decoding of cytosolic calcium oscillations in the mitochondria. *Cell*, 82(3), p.415.
- Harris, S.L. & Levine, A.J., 2005. The p53 pathway: positive and negative feedback loops. *Oncogene*, 24(17), pp.2899–2908.
- Hevner, R.F. & Wong-Riley, M.T., 1989. Brain cytochrome oxidase: purification, antibody production, and immunohistochemical/histochemical correlations in the CNS. *The Journal of neuroscience : the official journal of the Society for Neuroscience*, 9(11), pp.3884–3898.
- Huang, L.-K. & Wang, M.-J.J., 1995. Image thresholding by minimizing the measures of fuzziness. *Pattern Recognition*, 28(1), pp.41–51.
- Isokallio, M., 2017. The source and fate of mitochondrial DNA mutations using high-sensitivity next-generation sequencing technologies. (PhD Dissertation), Retrieved from Universitäts- und Stadtbibliothek Köln.
- Itoh, K. et al., 1996. Cytochrome c oxidase defects of the human substantia nigra in normal aging. *Neurobiology of aging*, 17(6), pp.843–848.
- Jones, R.G. et al., 2005. AMP-activated protein kinase induces a p53-dependent metabolic checkpoint. *Molecular cell*, 18(3), pp.283–293.
- Junge, W. & Nelson, N., 2015. ATP synthase. *Annual Review of Biochemistry*, 84, pp.631–657.
- Kann, O. & Kovács, R., 2007. Mitochondria and neuronal activity. *American journal of physiology. Cell physiology*, 292(2), pp.C641–57.

- Kann, O. et al., 2003. Coupling of neuronal activity and mitochondrial metabolism as revealed by nad(p)h fluorescence signals in organotypic hippocampal slice cultures of the rat. *Neuroscience*, 119(1), p.87.
- Kasahara, A. & Scorrano, L., 2014. Mitochondria: from cell death executioners to regulators of cell differentiation. *Trends in cell biology*, 24(12), pp.761–770.
- Kauppila, J.H.K. et al., 2016. A Phenotype-Driven Approach to Generate Mouse Models with Pathogenic mtDNA Mutations Causing Mitochondrial Disease. *Cell reports*, 16(11), pp.2980–2990.
- Kauppila, T.E.S. et al., 2016. Mammalian Mitochondria and Aging: An Update. *Cell metabolism*, 25(1), pp.57–71.
- Kearney, E.B. & Singer, T.P., 1955. Studies on Succinic Dehydrogenase. *Journal of Biological Chemistry*, 219, pp.963–975.
- Kianian, P.M.A. & Kianian, S.F., 2014. Mitochondrial dynamics and the cell cycle. *Frontiers in plant science*, 5, p.222.
- Kijima, K. et al., 2005. Mitochondrial GTPase mitofusin 2 mutation in Charcot-Marie-Tooth neuropathy type 2A. *Human genetics*, 116(1-2), pp.23–27.
- Koonin, E.V., 2010. The origin and early evolution of eukaryotes in the light of phylogenomics. *Genome biology*, 11(5), p.209.
- Laipis, P.J., Van de Walle, M.J. & Hauswirth, W.W., 1988. Unequal partitioning of bovine mitochondrial genotypes among siblings. *Proceedings of the National Academy of Sciences of the United States of America*, 85(21), pp.8107–8110.
- Lane, N. & Martin, W., 2010. The energetics of genome complexity. *Nature*, 467(7318), pp.929–934.
- Larsson, N.G. et al., 1991. Leber's hereditary optic neuropathy and complex I deficiency in muscle. *Annals of Neurology*, 30(5), pp.701–708.
- Larsson, N.G. & Clayton, D.A., 1995. Molecular genetic aspects of human mitochondrial disorders. *Annual review of genetics*, 29(1), pp.151–178.
- Liesa, M., Palacín, M. & Zorzano, A., 2009. Mitochondrial dynamics in mammalian health and disease. *Physiological reviews*, 89(3), pp.799–845.
- Liu, X., Kim, C.N., Yang, J., Jemmerson, R. & Wang, X., 1996. Induction of apoptotic program in cell-free extracts: requirement for dATP and cytochrome c. *Cell*, 86(1), pp.147–157.

- Löw, H., Alm, B. & Vallin, I., 1964. The use of phenazine methosulfate in the study of oxidative phosphorylation. *Biochemical and Biophysical Research Communications*, 14(4), pp.347–352.
- Majander, A. et al., 1991. Electron transfer properties of NADH: Ubiquinone reductase in the ND1/3460 and the ND4/11778 mutations of the Leber hereditary optic neuroretinopathy (LHON). *FEBS Letters*, 292(1-2), p.289.
- Martin, W., 2005. Archaeobacteria (Archaea) and the origin of the eukaryotic nucleus. *Current opinion in microbiology*, 8(6), pp.630–637.
- Martin, W.F., Garg, S. & Zimorski, V., 2015. Endosymbiotic theories for eukaryote origin. *Philosophical transactions of the Royal Society of London. Series B, Biological sciences*, 370(1678), p.20140330.
- McBride, H.M., 2015. Open questions: seeking a holistic approach for mitochondrial research. *BMC biology*, 13, p.8.
- McBride, H.M., Neuspiel, M. & Wasiak, S., 2006. Mitochondria: more than just a powerhouse. *Current biology : CB*, 16(14), pp.R551–60.
- McMillan, P.J., 1967. Differential demonstration of muscle and heart type lactic dehydrogenase of rat muscle and kidney. *The Journal of Histochemistry and Cytochemistry*, 15(1), pp.21–31.
- Melendez-Ferro, M. et al., 2013. An accurate method for the quantification of cytochrome C oxidase in tissue sections. *Journal of neuroscience methods*, 214(2), pp.156–162.
- Miller, W.L., 2013. Steroid hormone synthesis in mitochondria. *Molecular and cellular endocrinology*, 379(1-2), pp.62–73.
- Miyadera, H. et al., 2003. Atpenins, potent and specific inhibitors of mitochondrial complex II (succinate-ubiquinone oxidoreductase). *Proceedings of the National Academy of Sciences*, 100(2), pp.473–477.
- Mourier, A. et al., 2014. Loss of LRPPRC causes ATP synthase deficiency. *Human Molecular Genetics*, 23(10), pp.2580–2592.
- Murphy, J.L. et al., 2012. Cytochrome c oxidase-intermediate fibres: importance in understanding the pathogenesis and treatment of mitochondrial myopathy. *Neuromuscular disorders : NMD*, 22(8), pp.690–698.
- Müller-Höcker, J., 1989. Cytochrome-c-oxidase deficient cardiomyocytes in the human heart--an age-related phenomenon. A histochemical ultracytochemical study. *The American journal of pathology*, 134(5), pp.1167–1173.

- Müller-Höcker, J. et al., 1996. Defects of the respiratory chain in various tissues of old monkeys: a cytochemical-immunocytochemical study. *Mechanisms of ageing and development*, 86(3), p.197.
- Müller-Höcker, J., Pongratz, D. & Hübner, G., 1983. Focal deficiency of cytochrome-c-oxidase in skeletal muscle of patients with progressive external ophthalmoplegia. Cytochemical-fine-structural study. *Virchows Archiv. A, Pathological anatomy and histopathology*, 402(1), pp.61–71.
- Nass, M.M. & Nass, S., 1963. Intramitochondrial fibers with DNA characteristics. I. Fixation and electron staining reactions. *The Journal of Cell Biology*, 19, pp.593–611.
- Nachlas, M.M. et al., 1956. Cytochemical Demonstration of Succinic Dehydrogenase by the use of a new p-nitrophenyl substituted detetrazole. *The Journal of Histochemistry and Cytochemistry*, pp.420–436.
- Nachlas, M.M., Margulies, S.I. & Seligman, A.M., 1960. A colorimetric method for the estimation of succinic dehydrogenase activity. *Journal of Biological Chemistry*, 235(2), pp.499–503.
- Nakae, Y. & Stoward, P.J., 2001. A valid quantitative histochemical technique for assaying cytochrome c oxidase in single cells. *Histochemistry and Cell Biology*, 115, pp.413–419.
- Navarro, A. & Boveris, A., 2006. The mitochondrial energy transduction system and the aging process. *American journal of physiology. Cell physiology*, 292(2), pp.C670–86.
- Navarro, A. et al., 2002. Behavioral dysfunction, brain oxidative stress, and impaired mitochondrial electron transfer in aging mice. *American journal of physiology. Regulatory, integrative and comparative physiology*, 282(4), pp.R985–92.
- Old, S.L. Johnson, M.A., 1989. Methods of microphotometric assay of succinate dehydrogenase and cytochrome c oxidase activities for use on human skeletal muscle. *The Histochemical journal*, 21(9-10), pp.545–555.
- Olivo, P.D. et al., 1983. Nucleotide sequence evidence for rapid genotypic shifts in the bovine mitochondrial DNA D-loop. *Nature*, 306, pp.400–402.
- O'Malley, M.A., 2015. Endosymbiosis and its implications for evolutionary theory. *Proceedings of the National Academy of Sciences*, 112(33), p.10270.
- O'Rourke, B., 2007. Mitochondrial ion channels. *Annual review of physiology*, 69, pp.19–49.

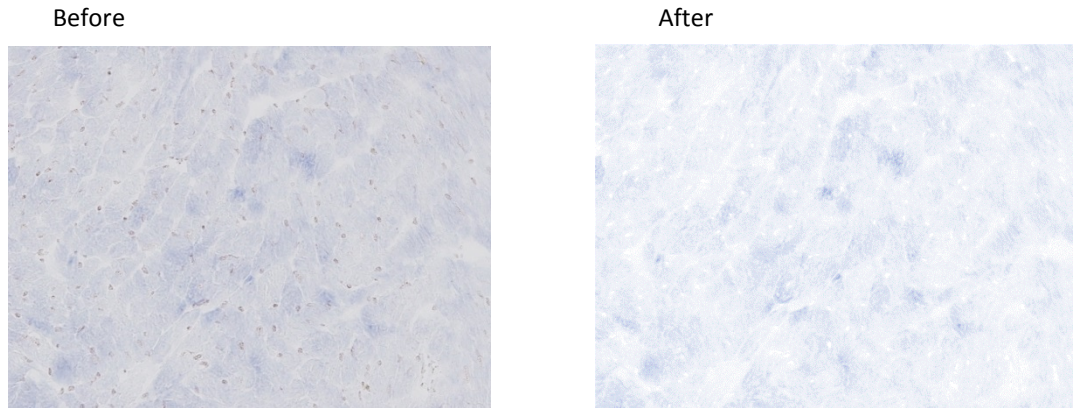
- Rambold, A.S. & Pearce, E.L., 2017. Mitochondrial Dynamics at the Interface of Immune Cell Metabolism and Function. *Trends in immunology*, 39(1), pp.6–18.
- Rinaldo, P., Matern, D. & Bennett, M.J., 2002. Fatty acid oxidation disorders. *Annual review of physiology*, 64, pp.477–502.
- Rizzuto, R. et al., 2012. Mitochondria as sensors and regulators of calcium signalling. *Nature reviews. Molecular cell biology*, 13(9), pp.566–578.
- Rocha, M.C. et al., 2015. A novel immunofluorescent assay to investigate oxidative phosphorylation deficiency in mitochondrial myopathy: understanding mechanisms and improving diagnosis. *Scientific reports*, 5, p.15037.
- Ross, J.M., 2011. Oxidase / Succinate Dehydrogenase (COX/SDH) Double-labeling Histochemistry. *Journal of Visualized Experiments*, 57(e3266), pp.1–6.
- Ruzzenente, B. et al., 2011. LRPPRC is necessary for polyadenylation and coordination of translation of mitochondrial mRNAs. *The EMBO Journal*, 31(2), pp.443–456.
- Sagan, L., 1967. On the origin of mitosing cells. *Journal of theoretical biology*, 14(3), pp.255–274.
- Sánchez-Martínez, A. et al., 2006. Modeling human mitochondrial diseases in flies. *Biochimica et biophysica acta*, 1757(9-10), pp.1190–1198.
- Sato, M. & Sato, K., 2013. Maternal inheritance of mitochondrial DNA by diverse mechanisms to eliminate paternal mitochondrial DNA. *Biochimica et biophysica acta*, 1833(8), pp.1979–1984.
- Scalettar, B.A., Abney, J.R. & Hackenbrock, C.R., 1991. Dynamics, structure, and function are coupled in the mitochondrial matrix. *Proceedings of the National Academy of Sciences*, 88(18), p.8057.
- Scheper, G.C. et al., 2007. Mitochondrial aspartyl-tRNA synthetase deficiency causes leukoencephalopathy with brain stem and spinal cord involvement and lactate elevation. *Nature Genetics*, pp.534–539.
- Schindelin, J. et al., 2012. Fiji: an open-source platform for biological-image analysis. *Nature methods*, 9(7), pp.676–682.
- Shutt, T.E. & McBride, H.M., 2013. Staying cool in difficult times: mitochondrial dynamics, quality control and the stress response. *Biochimica et biophysica acta*, 1833(2), pp.417–424.
- Stewart, J.B. & Chinnery, P.F., 2015. The dynamics of mitochondrial DNA heteroplasmy: implications for human health and disease. *Nature Reviews Genetics*, 16(9), pp.530–542.

- Swerdlow, R.H., 2011. Brain aging, Alzheimer's disease, and mitochondria. *Biochimica et biophysica acta*, 1812(12), pp.1630–1639.
- Tang, Y. & Zucker, R.S., 1997. Mitochondrial involvement in post-tetanic potentiation of synaptic transmission. *Neuron*, 18(3), pp.483–491.
- Taylor, R.W. & Turnbull, D.M., 2005. Mitochondrial DNA mutations in human disease. *Nature Reviews Genetics*, 6(5), pp.389–402.
- Tinel, H., 1999. Active mitochondria surrounding the pancreatic acinar granule region prevent spreading of inositol trisphosphate-evoked local cytosolic Ca²⁺ signals. *The EMBO Journal*, 18(18), p.4999.
- Trifunovic, A. et al., 2004. Premature ageing in mice expressing defective mitochondrial DNA polymerase. *Nature*, 429(6990), pp.417–423.
- Turnbull, D.M. & Rustin, P., 2016. Genetic and biochemical intricacy shapes mitochondrial cytopathies. *Neurobiology of disease*, 92, pp.55–63.
- Upholt, W.B. & Dawid, I.B., 1977. Mapping of mitochondrial DNA of individual sheep and goats: rapid evolution in the D loop region. *Cell*, 11(3), pp.571–583.
- Vishwanath, V.A., 2006. Fatty acid beta-oxidation disorders: a brief overview. *Annals of Neurosciences*, 23, pp.51-55.
- Wai, T., Teoli, D. & Shoubbridge, E.A., 2008. The mitochondrial DNA genetic bottleneck results from replication of a subpopulation of genomes. *Nature genetics*, 40(12), pp.1484–1488.
- Wallace, D.C., 1992. Diseases of the mitochondrial DNA. *Annual Review of Biochemistry*, 61(1), pp.1175–1212.
- Wallace, D.C., 1999. Mitochondrial diseases in man and mouse. *Science (New York, N.Y.)*, 283(5407), pp.1482–1488.
- Wallace, D.C., 1993. Mitochondrial diseases: genotype versus phenotype. *Trends in genetics : TIG*, 9(4), pp.128–133.
- Wang, C., Youle, R.J., 2009. The role of mitochondria in apoptosis. *Annual Reviews in Genetics*, 43, 95-118
- Wong-Riley, M.T.T., 1989. Cytochrome oxidase: an endogenous metabolic marker for neuronal activity. *Trends in Neurosciences*, 12(3), pp.94–101.

- Worsfold, M., Marshall, M.J. & Ellis, E.B., 1977. Enzyme Detection Using Phenazine Methosulphate and Tetrazolium Salts: Interference by Oxygen. *Analytical Biochemistry*, 79, pp.152–156.
- Yang, F. et al., 2003. Ca²⁺ influx-independent synaptic potentiation mediated by mitochondrial Na⁽⁺⁾-Ca²⁺ exchanger and protein kinase C. *The Journal of Cell Biology*, 163(3), pp.511–523.
- Yang, S.-N., Tang, Y.-G. & Zucker, R.S., 1999. Selective Induction of LTP and LTD by Postsynaptic [Ca²⁺]_i Elevation. *Journal of Neurophysiology*, 81(2), p.781.
- Yoshida, M., Muneyuki, E. & Hisabori, T., 2001. ATP synthase--a marvellous rotary engine of the cell. *Nature reviews. Molecular cell biology*, 2(9), pp.669–677.
- Zamzami, N. et al., 1996. Mitochondrial control of nuclear apoptosis. *The Journal of experimental medicine*, 183(4), pp.1533–1544.

Appendix

Appendix A | Fiji Macro for NBTx Quantitative Analysis



```

1 optionalManualRoiSelection=0;//if 1 manual ROI selection is offered for each image, if 0 autothresholding is applied without callback
2
3
4 directory=getDirectory("Choose a Directory");
5 fileList=getFileList(directory);
6 fileList=cleanFilelist(filelist);
7 resultpath=directory+File.separator+"ImageJ";
8 origFile="";
9 if(!File.exists(resultpath)){
10     File.makeDirectory(resultpath);
11 }
12 run("Clear Results");
13 run("Set Measurements...", "area mean standard min median area_fraction redirect=None decimal=3");
14 totalArea=newArray(filelist.length);
15 for(i=0;i<filelist.length;i++){
16     open(filelist[i]);
17     origImg=getImageID;
18     origFile=File.nameWithoutExtension;
19     deconvFile=resultpath+File.separator+origFile+"_ "+i+".tif";
20     selectImage(origImg);
21     //TODO: Implement white balancing
22     //TODO: Implement interactive component vector creation
23     run("Colour Deconvolution", "vectors=[User values] [r1]=107 [g1]=86 [b1]=37 [r2]=12 [g2]=17 [b2]=14 [r3]=10 [g3]=10 [b3]=10");

```

```

24 //selectWindow("02_1345_NBTx15min_22DC_080616_001.tif-(Colour_3)");
25 close("**Colour_2*");
26 //selectWindow("02_1345_NBTx15min_22DC_080616_001.tif-(Colour_2)");
27 close("**Colour_3*");
28 //selectWindow("02_1345_NBTx15min_22DC_080616_001.tif-(Colour_1)");
29 deconvImg=getImageID;
30 run("Invert");
31 run("Invert LUT");
32 run("Duplicate...", " ");
33 maskImg=getImageID;
34 setAutoThreshold("Huang");
35 setOption("BlackBackground", true);
36 run("Convert to Mask");
37 run("Create Selection");
38 if(optionalManualRoiSelection){
39     discardAutothreshold=getBoolean("Would you like to change the selected ROI?");
40     if(discardAutothreshold){
41         close;
42
43         selectImage(deconvImg);
44
45         run("Duplicate...", " ");
46
47         maskImg=getImageID;
48
49         //Prompt until user selected ROI
50
51         setSelection=-1;
52
53         while(setSelection<0){
54
55             waitForUser("Create user defined selection");
56
57             setSelection=selectionType();
58
59         }
60     }
61 }
62 roiManager("Add");
63 selectImage(deconvImg);

```

```

56     roiManager("Select", i);
57     run("Measure");
58     selectImage(deconvImg);
59     run("Select All");
60     getStatistics(area);//assumes constant image size!
61     totalArea[i]=area;
62     save(deconvFile);
63     roiManager("Save", resultpath+File.separator+"RoiSet.zip");
64     close("");
65 }
66 saveAs("Results", resultpath+File.separator+"Values.csv");
67 roiManager("reset");
68 plottitle=origFile;
69
70 xlabel="Image number";
71 ylabel="Stain Intensity [a.u.]";
72 thrshAreaValues=newArray(nResults);
73 thrshMeanValues=newArray(nResults);
74 thrshStdDevValues=newArray(nResults);
75
76 for(i=0;i<nResults;i++){
77     thrshAreaValues[i]=getResult("Area", i);
78     thrshMeanValues[i]=getResult("Mean", i);
79     thrshStdDevValues[i]=getResult("StdDev", i);
80 }
81 yValues=thrshMeanValues;
82
83 Plot.create(plottitle, xlabel, ylabel);
84 //Plot.setLimits(0, 5, 0, 3);
85 Plot.setLineWidth(5);
86 Plot.setColor("darkGray");
87 Plot.add("line", thrshMeanValues);
88 Plot.add("error bars", thrshStdDevValues);
89
90
91 Plot.setColor("lightGray");
92 for(i=0;i<nResults;i++){
93     x=i*(1/(nResults-1));
94     areaPercentage=round((thrshAreaValues[i]/totalArea[i])*100);
95     Plot.addText(areaPercentage+"%", x, 0.12);
96     row=nResults-(nResults-i);
97     setResult("%Area",row,areaPercentage);
98 }

```

```

99
100
101 Plot.show();
102 saveAs("png",resultpath+File.separator+"Plot.png");
103
104 function cleanFilelist(filelist){
105     origLength=filelist.length;
106     cleanLength=origLength;
107     for(i=0;i<origLength;i++){
108         if(!endsWith(filelist[i],".tif")){
109
110
111
112
113
114
115
116
117
118
119
120
121
122
123
124
125
126
cleanLength=cleanLength-1;
filelist[i]="-";
}
}
if(cleanLength==origLength) {
return filelist;
}
cleanList=newArray(cleanLength);
idx=0;
for(i=0;i<origLength;i++){
if(filelist[i]!="-"){
cleanList[idx]=filelist[i];
idx=idx+1;
}
}
return cleanList;
}

```

Appendix B | Raw Data

Wild-Type: SDH activity

Adjustment Factor:

	Sneu26	AF	Sneu27	AF	Sneu28	
S1	120.136	1.018119	165.394	1.01	91.765	0.96
S2	124.851	1.058077	165.395	1.01	99.677	1.04
S3	109.007	0.923804	162.904	0.99		
	117.998		164.5643		95.721	

Cell #	TypeI		Sneu27													
	S1S1	Adjusted	S1S2	Adjusted	S1S3	Adjusted	Average	SD	S1S1	Adjusted	S1S2	Adjusted	S1S3	Adjusted	Average	SD
1	154.665	151.6127	163.767	154.4972	131.438	142.8674	149.6591	6.056028	180.801	179.0109	183.133	181.3198	166.148	167.8263	176.0523	7.216908
2	135.693	133.0324	149.621	141.1519	116.309	126.4228	133.537	7.377419	154.034	152.5089	145.778	144.3947	144.123	145.5788	147.4741	4.40441
3	162.047	158.8696	166.867	157.4217	121.977	132.5837	149.625	14.77595	180.426	178.6396	172.528	170.8198	164.725	166.3889	171.9494	6.202987
4	170.194	166.8569	177.562	168.4547	147.692	160.5348	165.2821	4.188221	178.028	176.2653	165.173	163.5376	166.523	168.2051	169.336	6.438791
5	139.655	136.8284	152.256	143.6377	132.912	144.4696	141.6452	4.192165	155.136	153.6	151.702	150.2	146.012	147.4869	150.429	3.06299
6	142.232	139.4431	137.192	129.4264	127.283	138.3511	135.7402	5.495105	183.669	181.8713	208.585	206.5198	184.71	186.5756	191.6556	13.08591
7	138.094	130.4843	132.479	124.9802	128.146	139.2891	131.5845	7.21764	167.032	165.3782	177.197	175.4426	167.043	168.7303	169.8504	5.124814
8	153.324	150.3176	145.522	137.2949	126.416	137.4087	141.6704	7.488977	188.186	186.3228	199.381	197.4069	177.68	179.4747	187.7348	9.049099
9	151.708	148.7333	142.833	134.7481	135.874	147.6891	143.7235	7.79045	173.069	171.3554	172.178	170.4733	173.071	174.8192	172.216	2.297203
10	157.244	154.1608	161.165	152.0425	144.307	156.8554	154.3529	2.412235	183.294	181.4792	178.408	176.6416	161.174	162.802	173.6409	9.699412
11	146.665	143.7892	161.312	152.1811	143.001	155.4359	150.4687	6.009189	157.003	155.4485	157.237	155.6802	163.242	164.8909	158.6732	5.389394
12	142.705	139.3069	137.051	129.2934	123.39	134.1196	134.4399	5.313981	170.703	169.0129	174.151	172.4267	161.978	163.6141	168.3512	4.443394

Cell #	Sneu28		S1S1													
	S1S1	Adjusted	S1S2	Adjusted	S1S3	Adjusted	Average	SD	S1S1	Adjusted	S1S2	Adjusted	S1S3	Adjusted	Average	SD
1	182.998	190.6229	162.614	156.3596			173.4913	24.22781								
2	149.796	150.0375	122.238	117.5365			136.787	27.22429								
3	184.765	192.4635	139.227	133.8721			163.1678	41.43039								
4	170.665	177.776	127.563	122.6567			150.2164	38.97524								
5	124.73	129.9271	97.766	94.00577			111.9664	25.4002								
6	138.201	143.9594	84.969	81.70096			112.8302	44.02335								
7	144.194	150.2021	107.473	103.3394			126.7708	33.1369								
8	144.331	150.3448	116.672	112.1846			131.2647	26.98332								
9	154.753	161.201	131.326	126.275			143.738	24.69644								
10	134.854	140.4729	113.211	108.8567			124.6648	22.35602								
11	161.851	168.5948	137.592	132.3			150.4474	25.66429								
12	146.134	152.2229	125.628	120.7962			136.5095	22.22208								

Cell #	TypeII (gly)		Sneu27													
	S1S1	Adjusted	S1S2	Adjusted	S1S3	Adjusted	Average	SD	S1S1	Adjusted	S1S2	Adjusted	S1S3	Adjusted	Average	SD
1	58.955	57.79902	50.801	47.92547	39.733	43.18804	48.63751	7.454426	105.658	104.6119	123.426	122.204	120.387	121.603	116.1396	9.987839
2	69.371	68.01078	73.205	69.06132	50.165	54.52717	63.86634	8.105068	88.426	87.5505	98.022	97.05149	90.183	91.09394	91.89864	4.801339
3	56.922	55.80588	65.393	61.69151	44.588	48.46522	55.32087	6.626472	88	87.12871	77.813	77.04257	84.603	85.45758	83.20962	5.405786
4	86.611	84.91275	80.227	75.88585	59.14	64.28261	74.9604	10.33418	74.94	74.19802	77.177	76.41287	90.041	90.9051	80.52047	9.100312
5	64.004	62.74902	53.913	50.86132	44.304	48.15652	53.92229	7.762885	87.493	86.62673	88.142	87.26931	84.275	85.12626	86.34077	1.099769
6	75.812	74.32549	78.847	74.04434	59.214	64.36304	70.91096	5.672402	128.367	127.096	123.659	122.4347	102.576	103.6121	111.7143	12.34323
7	84.947	83.28137	75.807	71.51604	66.489	72.27065	75.68935	6.585698	128.233	126.9634	134.195	132.8669	130.388	131.7051	130.5116	3.127225
8	77.083	75.57157	77.584	73.54151	52.625	57.20109	68.77139	10.07145	119.526	118.3426	115.28	114.1386	119.488	120.6949	117.7254	3.321458
9	71.736	70.32943	57.617	54.38566	43.749	47.55326	57.41245	11.69124	92.626	91.70891	90.659	89.76139	84.739	85.59495	89.02175	3.123368
10	74.076	72.6253	79.151	74.67075	58.648	63.74783	70.34737	5.806813	120.382	119.1301	108.319	107.2465	112.053	113.1848	113.2072	5.971813
11	73.85	72.5	53.731	50.68962	48.069	52.24891	58.47351	11.21671	83.946	83.11485	81.704	80.88505	78.781	79.57677	81.19556	1.788082
12	80.355	78.77941	67.405	63.58962	52.202	56.7413	66.37011	11.27909	102.16	101.1485	103.63	102.604	104.16	105.2121	102.9882	2.058872

Cell #	Sneu28		S1S1													
	S1S1	Adjusted	S1S2	Adjusted	S1S3	Adjusted	Average	SD	S1S1	Adjusted	S1S2	Adjusted	S1S3	Adjusted	Average	SD
1	39.225	40.85938	40.345	36.79327			39.82632	1.460357								
2	42.112	43.86667	51.951	49.55288			46.90378	4.303606								
3	39.627	41.27813	37.934	36.475			38.87656	3.396322								
4	45.158	47.03958	41.941	40.32788			43.68373	4.745888								
5	70.657	73.60104	57.745	55.52404			64.56254	12.78237								
6	52.955	55.20313	61.124	58.77308			56.9881	2.524337								
7	50.732	52.84583	45.321	43.57788			48.21186	6.553429								
8	59.155	62.41146	53.768	57.46923			53.94034	3.494683								
9	60.127	62.63229	50.776	48.62308			55.72768	9.746589								
10	92.769	96.63438	92.173	88.62788			92.63119	5.661444								
11	71.67	74.65625	55.723	53.57981			64.11803	14.9033								
12	54.742	57.02292	45.05	43.31731			50.17011	9.691329								

Cell #	TypeII (ox)		Sneu27													
	S1S1	Adjusted	S1S2	Adjusted	S1S3	Adjusted	Average	SD	S1S1	Adjusted	S1S2	Adjusted	S1S3	Adjusted	Average	SD
1	211.177	207.0963	204.314	192.7491	187.135	203.4076	201.0643	7.426266	194.959	193.0287	196.341	194.397	197.649	199.6455	195.6304	3.492838
2	201.238	197.2922	206.377	194.6953	184.737	200.8011	197.5962	3.064234	206.984	204.9347	202.427	200.4228	199.743	201.7606	202.3727	2.317378
3	229.225	224.7304	220.541	208.0575	188.471	204.8598	212.5492	10.66967	208.228	206.1663	206.673	204.6267	194.234	196.196	202.3297	5.367444
4	209.231	205.1284	201.345	189.9481	172.158	187.1283	194.0683	9.681596	213.925	211.8069	219.147	216.9772	209.653	211.7707	213.5183	2.995584
5	201.571	197.6186	210.652	198.7283	200.843	218.3076	204.8848	11.63769	210.413	208.3297	207.788	205.7307	202.499	204.5444	206.2016	1.936071
6	211.367	207.2127	203.967	192.4217	180.764	196.4826	198.7057	7.64201	183.644	181.8257	198.878	196.9089	196.604	198.5899	192.4415	9.238171
7	213.143	208.9637	205.509	193.8764	175.075	190.2989	197.713	9.906233	203.382	207.3089	205.471	203.4366	198.278	200.2808	203.6755	35.20132
8	204.474	200.4647	209.022	197.1906	183.57	195.5226	199.0626	1.686908	213.868	211.7505	218.583	216.4188	202.603	204.6495	210.9396	5.926113
9	191.823	188.0618	191.063	180.2481	181.651	197.4467	188.5855	8.611268	211.527	209.4327	198.722	196.7545	196.591	198.5768	201.588	6.854545
10	193.327	189.5363	197.035	185.9387	174.491	188.6641	188.3797	2.114948	209.747	207.6703	210.702	208.6158	199.318	201.3313	205.8725	3.961804
11	189.886	186.1627	210.506	198.5906	187.183	203.4598	196.071	8.919525	215.187	213.0564	221.341	213.1495	215.408	217.5838	216.5966	3.164232
12	210.003	205.8853	211.923	199.9274	183.299	199.238	201.6836	3.65509	199.767	197.7891	194.304	192.3802	183.377	185.2293	191.7935	6.300011

Cell #	Sneu28		S1S1													
	S1															

mtDNA mutator (#21-4410): SDH and NBTx

Adjustment Factor:

	Azide	AF	NBTx	AF	
S1	111	0.979412	18.79		1.06
S2	116	1.023529	15.95		0.90
S3	113	0.997059	18.69		1.05
	113.3333		17.81		

GA

Cell #	Type II (ox)		Azide-S2	Adjusted	Azide-S3	Adjusted	Average Azide	NBTx-S1	Adjusted	NBTx-S2	Adjusted	NBTx-S3	Adjusted	Average NBTx		
	Azide-S1	Adjusted														
1	206.6	210.8163	183.39	179.7941176	184.67	185.2257	191.9454	16.56684	70.147	66.17642	91.009	101.1211	136.636	130.1295	99.14235	32.02244
2	210.214	214.5041	187.579	183.9009804	180.863	181.4072	193.2708	18.43082	53.303	50.28585	60.554	67.28222	86.515	82.39524	66.65444	16.0639
3	203.725	207.8827	168.944	165.6313725	163.821	164.3139	179.276	24.78285	48.364	45.62642	84.757	94.17444	81.843	77.94571	72.58219	24.71444
4	208.63	212.8878	196.113	192.2676471	195.783	196.3721	200.5092	10.91484	58.64	55.32075	53.062	58.95778	86.581	82.4581	65.57888	14.73051
5	197.831	201.8684	194.105	190.2990196	187.759	188.324	193.4971	7.316662	31.84	30.03774	42.32	47.02222	53.927	51.35905	42.80634	11.26853
6	184.789	188.5602	189.012	185.3058824	195.551	196.1394	190.0018	5.558786	25.919	24.45189	37.627	41.80778	42.293	40.27905	35.5129	9.60957
7	182.005	185.7194	153.28	150.2745098			167.9969	25.06331	35.004	33.02264	41.362	45.95778	60.507	57.62571	45.53538	12.30697
8	210.527	214.8235	225.636	221.2117647	217.5	218.1545	218.0632	3.195125	57.94	54.66038	48.367	53.74111	93.029	88.59905	65.66685	19.86519
9	183.354	187.0959	194.101	190.295098	194.889	195.4754	190.9555	4.228607	33.045	31.17453	15.595	17.32778	43.715	41.63333	30.04521	12.19207
10	209.826	214.1082			170.835	171.349	192.7286	30.23526	98.988	93.38491	143.984	159.9822	166.912	158.9638	137.4436	38.15939
11	212.327	216.6602	211.295	207.1519608	220.897	221.5617	215.1246	7.326565	54.535	51.44811	55.22	61.35556	66.56	63.39048	58.73138	6.389032
12	209.333	213.6051	198.589	194.695098	207.519	208.1434	205.4812	9.732041	65.46	61.75472	74.948	83.27556	67.539	64.32286	69.78438	11.75405
13	207.846	212.0878	204.843	200.8264706	208.271	208.8977	207.2706	5.804275	60.327	56.91226	49.623	55.13667	52.657	50.14952	54.06615	3.506161
14	213.362	217.7163	208.506	204.4176471	224.911	225.5878	215.9072	10.70038	64.686	61.02453	47.962	53.29111	50.681	48.26762	54.19442	6.426248
15	212.217	216.548	216.872	212.6196078	227.774	228.4594	219.209	8.248355	104.659	98.73491	68.026	75.58444	55.797	53.14	75.81978	22.79836

Cell #	Type II (gly)		Azide-S2	Adjusted	Azide-S3	Adjusted	Average Azide	NBTx-S1	Adjusted	NBTx-S2	Adjusted	NBTx-S3	Adjusted	Average NBTx		
	Azide-S1	Adjusted														
1	25.876	26.40408	29.549	28.96960784	30.555	30.86364	28.74578	2.238187	1.144	1.079245	2.524	2.804444	1.427	1.359048	1.747579	0.925903
2	65.945	67.29082	75.36	73.88235294	71.152	71.87071	71.01463	3.378128	3.206	3.024528	2.859	3.176667	7.268	6.921905	4.374367	2.207544
3	28.126	28.7	22.465	22.0245098	18.637	18.82525	23.18325	5.038321	0.866	0.816981	1.597	1.774444	2.616	2.491429	1.694285	0.840097
4	23.724	24.20816	24.204	23.72941176	22.875	23.10606	23.68121	0.55263	0.398	0.375472	0.987	1.096667	2.974	2.832381	1.43484	1.262882
5	63.689	64.98878	61.104	59.90588235	69.643	70.34646	65.08037	5.220894	2.248	2.120755	2.271	2.523333	4.834	4.60381	3.082633	1.332667
6	33.762	34.45102	28.23	27.67647056	26.028	26.29091	29.4728	4.366572	1.024	0.966038	0.599	0.665556	2.082	1.982857	1.204817	0.69035
7	30.248	30.86531	27.407	26.86960784	22.135	22.35859	26.69783	4.255961	1.21	1.141509	0.395	0.438889	1.923	1.831429	1.137276	0.696279
8	47.083	48.04388			54.354	54.90303	51.47345	4.850153	2.141	2.019811	6.698	7.442222	4.142	3.944762	4.468932	2.748949
9	50.291	51.31735	71.492	70.09019608	75.215	75.97475	65.7941	12.87786	3.023	2.851887	5.327	5.918889	6.924	6.594286	5.121687	1.994501
10	40.096	40.91429	42.882	42.04117647	61.176	61.79394	48.2498	11.74309	1.432	1.350943	1.299	1.443333	2.946	2.805714	1.866664	0.814553
11	80.989	82.64184	74.711	73.24607843	89.788	90.69495	82.19429	8.733041	4.625	4.363208	6.129	6.81	9.333	8.888571	6.68726	2.265177
12	75.26	76.79592	83.328	81.69411765	96.225	97.19697	85.229	10.64999	4.984	4.701887	5.63	6.255556	6.703	6.38381	5.780417	0.936234
13	81.728	83.39592	79.606	78.04509804	98.186	99.17778	86.87293	10.98703	6.921	6.529245	6.231	6.923333	4.271	4.067619	5.840066	1.547579
14	32.875	33.54592	36.008	35.30196078	41.651	42.07172	36.9732	4.501898	1.83	1.726415	1.673	1.858889	2.584	2.460952	2.015419	0.391488
15	72.144	73.61633	74.209	72.75392157	86.204	87.07475	77.815	8.030763	6.296	5.939623	2.509	2.787778	4.627	4.406667	4.378022	1.576118

Soleus

Cell #	Type I		Azide-S2	Adjusted	Azide-S3	Adjusted	Average Azide	NBTx-S1	Adjusted	NBTx-S2	Adjusted	NBTx-S3	Adjusted	Average NBTx		
	Azide-S1	Adjusted														
1	161.713	165.0133	140.504	137.7490196	159.297	159.7763	154.1795	14.46817	38.717	36.52547	18.477	20.53	16.683	15.88857	24.31468	10.82651
2	182.815	186.5459	174.455	171.0343137	191.725	192.3019	183.294	11.00039	78.523	74.0783	48.818	54.24222	35.78	34.07619	54.13224	20.00128
3	161.568	164.8653	143.237	140.4284314	167.465	167.9689	157.7542	15.0846	45.545	42.96698	31.681	35.20111	24.137	22.98762	33.71857	10.07185
4	178.195	181.8316	166.262	163.0019608	195.63	196.2187	180.3507	16.65779	50.06	47.22642	33.417	37.13	22.996	21.90095	35.41912	12.74912
5	157.889	161.1112	153.934	150.8176471	177.422	177.9559	163.2949	13.70026	35.849	33.81981	16.698	18.55333	14.69	13.99048	22.12121	10.38499
6	148.749	151.7847	143.238	140.4294118	170.584	171.0973	154.4371	15.50504	44.376	41.86415	20.275	22.52778	17.087	16.27333	26.88842	13.34106
7	165.728	169.1102	161.629	158.4598035	179.025	179.5637	169.0446	10.5521	39.42	37.18868	19.895	22.10556	13.956	13.29143	24.19522	12.08489
8	149.296	152.3429	143.552	140.7372545	167.514	168.0181	153.6994	13.6909	39.45	37.21698	28.718	31.90889	16.931	16.12476	28.41688	10.97115
9	168.962	172.4102	170.4	167.0588235	205.75	206.3691	181.946	21.31956	32.227	30.40283	8.962	9.957778	9.816	9.348571	16.56973	11.98369
10	141.136	144.0163	156.078	153.0176471	164.398	164.8927	153.9756	10.47109	28.911	27.27453	21.969	24.41	12.263	11.67905	21.12119	8.301623
11	169.493	172.952	155.235	152.1911765	179.369	179.9087	168.3506	14.42031	44.624	42.09811	25.912	28.79111	29.273	27.87905	32.92276	7.959167
12	190.08	193.9592	184.995	181.3676471	221.855	222.5226	199.2831	21.08768	45.586	43.00566	63.41	70.45556	77.758	74.05524	62.50548	16.98299
13	137.545	140.352	132.032	129.4431373	168.089	168.5948	146.13	20.20523	41.545	39.1934	27.543	30.60333	24.807	23.62571	31.14081	7.797746
14	171.138	174.6306	164.671	161.4421565	193.126	193.7071	176.5933	16.22178	48.545	45.79717	25.537	28.37444	28.66	27.29524	33.82228	10.38458
15	172.655	176.1786	171.995	168.622549	190.221	190.7934	178.5315	11.27114	56.085	52.91038	36.397	40.44111	37.313	35.53619	42.96256	8.957336

mtDNA mutator (#21-4335): SDH and NBTx

Adjustment Factor

	Azide	AF	NBTx	AF
S1	88.052	0.97059796	11.491	0.72
S2	105.841	1.16668626	26.409	1.663739725
S3	78.265	0.86271578	9.72	0.612347753
	90.71939		15.8739393	

GA

Cell #	Type II (ex)		Azide-S2	Adjusted	Azide-S3	Adjusted	Average Azide	NBTx-S1	Adjusted	NBTx-S2	Adjusted	NBTx-S3	Adjusted	Average NBTx		
	Azide-S1	Adjusted														
1	206.61	213	241.896	206.7487179	198.583	230.1877825	216.6455	12.137339	30.038	41.719444	76.769	46.246986	28.799	47.211475	45.059102	2.932206
2	205.04	211.381443	229.078	195.7991624	201.304	233.3418398	213.5055	18.86423	54.221	75.306944	94.563	56.965663	48.691	79.821311	70.697973	12.10484
3	217.932	224.672165	240.086	205.2017094	205.448	238.1453576	222.6731	16.56256	32.871	45.654167	71.677	43.178916	32.561	53.378689	47.409324	5.320252
4	219.318	226.101031	245.778	210.0666667	203.625	236.0322244	224.0666	13.10178	58.091	80.681944	103.221	62.181325	52.2	85.57377	76.14568	12.39895
5	205.724	212.086598	223.593	191.1051282	195.861	227.0325722	210.0748	18.04802	52.623	73.0875	95.99	57.825301	39.998	65.570492	65.494431	7.631384
6	199.285	205.448454	217.911	186.2487179	200.844	232.8086241	208.1686	23.39884	37.102	51.530556	83.025	50.01506	28.43	46.606557	49.384058	2.521916
7	207.871	214.3	230.215	196.7649573	202.458	234.6794946	215.2482	18.97504	53.61	74.458393	99.34	59.843373	42.344	69.416393	67.906039	7.423621
8	208.938	215.4	227.154	194.1487179	210.905	244.4708473	218.0065	25.26212	36.762	51.058393	87.472	52.693976	32.254	52.87541	52.20924	1.000834
9	202.891	209.165979	224.111	191.5478632	203.188	235.5256752	212.0798	22.13923	12.357	17.1625	45.551	27.440361	15.059	24.686885	23.095852	5.320283
10	213.087	219.67732	238.671	199.7188034	195.284	226.3637417	215.2533	13.86244	23.176	32.188889	67.496	40.660241	22.32	36.590164	36.479705	4.236755
11	204.941	211.279381	218.799	187.0025641	188.933	219.0019706	205.7613	16.69812	12.954	17.991667	55.45	33.403614	7.058	11.570492	20.988591	11.22085
12	195.567	201.615464	223.214	190.7811966	177.582	205.8444419	199.4137	7.769245	20.34	28.25	57.151	34.428313	17.762	29.118039	30.598782	3.34475
13	208.281	214.72268	222.497	190.1683761	186.098	215.7157761	206.8689	14.47164	40.545	56.3125	84.527	50.91988	32.794	53.760566	53.664345	2.6976
14	206.52	212.907216	236.447	202.091453	205.731	238.4739875	217.824	18.68266	39.062	54.252778	87.379	52.637952	32.658	53.537705	53.476145	0.809171
15	218.042	224.785567	239.706	199.7487179	207.498	240.5216182	221.6853	20.56249	45.522	63.225	91.41	55.066265	37.641	61.706557	59.999274	4.39905

Cell #	Type II (gly)		Azide-S2	Adjusted	Azide-S3	Adjusted	Average Azide	NBTx-S1	Adjusted	NBTx-S2	Adjusted	NBTx-S3	Adjusted	Average NBTx		
	Azide-S1	Adjusted														
1	48.921	50.4340206	51.699	44.16717949	34.992	40.68837209	45.10319	4.936975	6.248	8.677778	8.304	5.0024056	2.225	3.647541	5.7759035	2.602796
2	51.725	53.3247423	57.217	48.9034188	33.379	38.8129707	47.01365	7.438253	5.623	7.8097222	7.746	4.6662651	3.109	5.0967213	5.8575695	1.704259
3	46.956	48.4082474	51.224	43.79487179	32.435	37.71511628	43.30608	5.363297	3.834	5.325	7.424	4.4722892	2.252	3.6918039	4.4963641	0.816864
4	25.399	26.1226804	28.511	24.36837607	18.408	21.40465116	23.96524	2.38471	2.016	2.8	2.976	1.7927711	2.307	3.7819672	2.7915794	0.994625
5	37.709	38.8752577	56.853	48.59230769	28.018	32.57906977	40.01555	8.067288	2.608	3.6222222	6.632	3.9951807	1.407	2.3065574	3.3079868	0.887085
6	34.71	35.7835052	47.029	40.1957265	35.397	41.15990233	39.04618	2.866338	3.282	4.5583393	8.777	5.2873494	2.493	4.0868852	4.6441893	0.60482
7	34.684	35.756701	46.015	39.32905983	27.908	32.45116279	35.84564	3.439811	6.163	8.5997222	7.912	4.7662651	1.51	2.4754098	5.2671324	3.072925
8	36.734	37.8701031	69.512	59.41196581	34.056	39.6	45.62736	11.96912	1.749	2.4291667	2.308	1.3903614	3.435	5.6311475	3.1502252	2.210432
9	48.097	49.5845361	60.545	51.74786325	33.788	39.28837209	46.87359	6.657451	2.238	3.1083333	7.19	4.3313253	0.815	1.3360656	2.9252414	1.506
10	60.753	62.6319588	57.625	49.25213675	62.013	72.10813953	61.33075	11.48343	2.01	2.7916667	6.619	3.9673494	2.694	4.4163934	3.7318032	0.841969
11	65.071	67.0835052	63.448	54.22905983	65.942	76.87674419	65.99644	11.26326	4.439	6.1652778	6.878	4.1439735	2.162	3.5442623	4.6176379	1.373963
12	35.448	36.5443299	28.247	24.14273504	19.939	23.18488872	27.95732	7.451978	2.831	3.9319444	2.557	1.5403614	1.945	3.1885246	2.8869435	1.223981
13	36.516	37.6453608	34.302	29.31794872	27.243	31.67790698	32.88041	4.291963	2.367	3.2875	4.367	2.6307229	3.048	4.9967213	3.6383147	1.221389
14	31.249	32.2154639	35.053	29.95962906	26.77	31.12790698	31.01017	1.128057	2.242	3.1138889	4.757	2.8656627	1.536	2.5180328	2.8325281	0.299307
15	37.829	38.9989691	51.281	43.82991453	40.527	47.1244186	43.31777	4.086864	1.342	1.8638889	6.474	3.9	1.191	1.952459	2.572116	1.150894

Soleus

Cell #	Type I		Azide-S2	Adjusted	Azide-S3	Adjusted	Average Azide	NBTx-S1	Adjusted	NBTx-S2	Adjusted	NBTx-S3	Adjusted	Average NBTx		
	Azide-S1	Adjusted														
1	137.759	142.019588	163.596	139.825641	112.439	130.7430233	137.5294	5.978688	15.19	21.097222	33.259	20.035542	10.034	16.44918	19.193982	2.435619
2	147.419	151.978351	165.757	141.6726496	135.589	157.6616279	150.4375	8.105806	6.736	9.3555556	33.378	20.107229	7.88	12.918039	14.126939	5.476834
3	142.525	146.93299	161.936	138.4068976	131.884	153.3534884	146.2311	7.498005	11.471	15.931944	34.804	20.966265	7.304	11.97377	16.29066	4.506967
4	142.303	146.704124	155.145	132.6025641	121.11	140.8255814	140.0441	7.083187	12.726	17.675	33.173	19.983735	6.539	10.709836	16.122857	4.827859
5	154.272	159.043299	167.89	143.4957265	131.077	152.4151169	151.6514	7.801873	20.549	28.540278	43.792	26.380723	17.55	28.770492	27.897164	1.318911
6	161.588	166.585567	162.237	138.6641026	126.617	147.2290698	150.8262	14.30408	14.483	20.115278	36.282	21.856627	11.165	18.303279	20.091728	1.776791
7	140.427	144.770103	181.096	154.782906	140.021	162.8151163	154.1227	9.040604	27.984	38.866667	53.934	32.490361	20.561	33.706557	35.021195	3.385399
8	152.47	157.185567	169.819	145.1444444	144.516	168.0418605	156.7906	11.45382	17.228	23.927778	40.168	24.19759	11.709	19.195082	22.44015	2.813548
9	172.256	177.583505	187.088	159.9042735	145.088	168.7069767	168.7316	8.839642	8.438	11.719444	43.806	26.389157	8.464	13.87541	17.328004	7.920885
10	151.181	155.856701	175.577	150.065812	118.453	137.7360465	147.8862	9.254869	11.057	15.356944	35.457	21.359639	11.972	15.62623	18.780938	3.089332
11	132.974	137.086598	169.078	144.5111111	112.886	131.2627907	137.6202	6.640258	17.576	24.411111	42.419	25.53614	18.895	30.97541	26.980045	3.506926
12	139.923	144.250515	171.741	146.7871795	98.062	114.0255814	135.0211	18.22693	20.596	28.605556	53.106	31.991566	13.573	22.25082	27.61598	4.945198
13	100.722	103.837113	135.659	115.9478632	94.102	109.4209902	109.7353	6.061492	11.387	15.815278	36.161	21.783735	6.781	11.116399	16.238469	5.346247
14	129.765	133.778351	154.241	131.8299145	136.75	159.0116279	141.54	15.16224	12.299	17.081944	33.034	19.9	10.048	16.472131	17.818025	1.828642
15	139.85	144.175258	161.918	138.391453	141.828	164.9162791	149.161	13.94757	11.838	16.441667	30.99	18.666675	4.388	7.1934426	14.101261	6.085093

mtDNA mutator (#21-4336): SDH and NBTx

Adjustment Factor

	AzIde	AF	NBTx	AF	
S1	86.368	0.864706	29.114		1.06
S2	109.16	1.092897	25.683	0.937387083	
S3	104.116	1.042397			
	99.88133		27.3985		

GA

Cell #	Type II (ox)										Average NBTx			
	AzIde-S1	Adjusted	AzIde-S2	Adjusted	AzIde-S3	Adjusted	Average Azide	NBTx-S1	Adjusted	NBTx-S2	Adjusted	NBTx-S3	Adjusted	Average NBTx
1	218.49	254.0581	236.834	217.2788991	222.554	213.9942	228.4438	22.24342	135.489	127.8198	114.139	121.4245	124.6221	4.522191
2	200.719	233.3942	233.975	214.6559633	214.499	206.249	218.0997	13.89638	61.725	58.23113	73.068	77.73191	67.98152	13.78914
3	162.974	189.5047	181.477	166.4926606	165.934	159.5519	171.8497	15.6785	41.503	39.15377	26.799	28.50957	33.83167	7.526585
4	196.74	228.7674	233.625	214.3348624	215.721	207.424	216.8421	10.89036	87.267	82.32736	44.748	47.60426	64.96581	24.55294
5	208.234	242.1326	240.582	221.0844037	185.788	178.6423	213.9531	32.3403	84.56	79.77358	40.682	43.27872	61.52615	25.80576
6	196.999	229.0686	230.2	211.1926606	215.616	207.3231	215.8614	11.60022	51.658	48.73396	38.323	40.76915	44.75156	5.631974
7	229.211	266.5244	233.997	214.6761468	235.089	226.0471	235.7492	27.25177	84.231	79.46321	79.091	84.13936	81.80128	3.30654
8	226.325	263.1686	231.809	212.6688073	242.432	233.1077	236.315	25.40222	72.849	68.72547	67.83	72.15957	70.44252	2.428277
9	215.454	250.5279	236.716	217.1706422	226.938	218.2096	228.6361	18.96602	97.542	92.02075	56.938	60.57234	76.29655	22.23739
10	201.365	234.1453	230.646	211.6018349	221.388	212.8731	219.5401	12.66449	61.471	57.99151	52.672	56.03404	57.01278	1.384138
11	191.662	222.8628	225.323	206.7183486	199.684	192.0038	207.195	15.43499	74.788	70.55472	50.816	54.05957	62.30715	11.66938
12	205.687	239.1709	231.49	212.3761468	234.754	225.725	225.7574	13.39742	64.176	60.5434	66.029	70.24362	65.39351	6.859092
13	189.91	220.8256	226.364	207.6733945	224.576	215.9385	214.8125	6.647998	68.442	64.98887	59.977	63.80532	64.18709	0.599911
14	193.389	224.8709	226.13	207.4587156	224.695	216.0529	216.1275	8.706347	55.415	52.2783	50.153	53.25426	52.81628	0.760814
15	193.913	225.4802	207.826	190.666055			208.0731	24.61734	27.412	25.86038	23.316	24.80426	25.33232	0.746791

Cell #	Type II (gly)										Average NBTx			
	AzIde-S1	Adjusted	AzIde-S2	Adjusted	AzIde-S3	Adjusted	Average Azide	NBTx-S1	Adjusted	NBTx-S2	Adjusted	NBTx-S3	Adjusted	Average NBTx
1	67.043	77.95698	94.159	86.38440367	81.184	78.06154	80.80097	4.835675	18.468	17.42264	7.068	7.519149	12.4709	7.002827
2	68.638	79.81163	96.267	88.31834862	68.411	65.77981	77.96993	11.38158	14.914	14.06981	11.406	12.13404	13.10193	1.368795
3	31.259	36.34767	44.087	40.44678899	38.674	38.14803	38.31418	2.054599	3.275	3.089623	1.816	1.921915	2.510769	0.818623
4	45.61	53.03488	62.815	57.62844037	49.046	47.15962	52.60765	5.247473	4.125	3.891509	4.364	4.642553	4.267031	0.531068
5	33.314	38.73721	42.038	38.56697248	39.84	38.30769	38.53729	0.216291	5.129	4.838679	3.35	3.56383	4.201255	0.901455
6	50.333	58.52674	82.907	76.06146789	77.814	74.82115	69.80312	9.785301	5.917	5.582075	6.198	6.59617	6.087846	0.715268
7	35.09	40.80233	53.991	49.53302752	44.342	42.63654	44.32396	4.60346	6.038	5.696226	4.777	5.081915	5.389071	0.434384
8	50.967	59.26395	81.692	74.94678899	69.743	67.06058	67.09044	7.84146	7.141	6.736792	5.361	5.703191	6.219992	0.738066
9	46.284	53.81186	58.951	54.08348624	61.071	58.72212	55.5414	2.757761	5.459	5.15	8.532	9.076596	7.113288	2.776522
10	24.102	28.02558	31.951	29.31284404	38.127	36.66058	31.333	4.658494	1.426	1.345283	1.81	1.925532	1.635407	0.410298
11	78.011	90.71047	111.733	102.5073394	98.64	94.84615	96.02132	5.985593	14.434	13.61698	15.262	16.23617	14.92658	1.852046
12	42.342	49.23488	64.302	58.99266055	68.616	65.97692	58.06816	8.409221	5.988	5.649057	7.723	8.215957	6.932507	1.815073
13	38.457	44.71744	30.069	27.58623853	45.858	44.09423	38.7993	9.715798	3.82	3.603774	5.251	5.58617	4.594972	1.401766
14	47.514	55.24884	61.513	56.43394495	76.708	73.75769	61.81349	10.36094	4.237	3.99717	4.107	4.369149	4.183159	0.263029
15	38.584	44.86512	49.68	45.57798165	63.753	61.30096	50.58135	9.290293	5.721	5.39717	6.771	7.203191	6.300181	1.27705

Solcus

Cell #	Type I										Average NBTx			
	AzIde-S1	Adjusted	AzIde-S2	Adjusted	AzIde-S3	Adjusted	Average Azide	NBTx-S1	Adjusted	NBTx-S2	Adjusted	NBTx-S3	Adjusted	Average NBTx
1	134.321	156.1872			150.283	144.5029	150.345	8.262065	42.018	39.63962	59.39	63.18085	51.41024	16.64616
2	139.955	162.7384			143.306	137.7942	150.2663	17.63817	59.084	55.73862	67.47	71.7766	63.75811	11.33985
3	165.782	192.7698			196.317	188.7693	190.7881	2.830846	47.211	44.53898	68.945	73.34574	58.94221	20.36967
4	158.734	184.5744			178.716	171.8423	178.2084	9.002962			59.012	62.77872	62.77872	#DIV/0!
5	157.841	183.536			156.128	150.1231	166.8296	23.62654			30.614	32.96809	32.96809	#DIV/0!
6	159.239	185.1616			166.78	160.3654	172.7635	17.53359	40.526	38.23208	45.768	48.68936	43.46072	7.394418
7	154.693	179.8756			148.912	143.1846	161.5301	25.94443	47.721	45.01981	66.212	70.4383	57.72905	17.97358
8	146.149	169.9407			167.508	161.0654	165.503	6.275794	61.27	57.80189	86.936	92.48511	75.1435	24.52474
9	148.502	172.6767			146.204	140.5808	156.6288	22.69528	59.69	56.31132	77.728	82.68936	69.50034	18.65209
10	168.813	196.2942			157.035	150.9952	173.6447	32.03123	42.347	39.95	58.039	61.74362	50.84681	15.41041
11	141.461	164.4895			167.49	161.0481	162.7688	2.433478	38.564	36.38113	51.917	55.23085	45.80599	13.32876
12	142.251	165.4081			173.682	167.0019	166.205	1.126975	36.677	34.60094	43.111	45.86277	40.23185	7.963311
13	154.946	180.1698			177.432	170.6077	175.3887	6.761408	26.241	24.75566	44.156	46.97447	35.85506	15.71107
14	143.906	167.3326			163.793	157.4933	162.4129	6.957428	19.753	18.63491	32.788	34.88085	26.75788	11.48762
15	141.075	164.0407			159.801	153.6548	158.8478	7.343933	26.751	25.23679	21.328	22.68936	23.96308	1.801306

Value of Azide ROD: Comparing Wild-Type versus Mutator

	Type IIc			Type I			Type IIb		
	Sneu26	Sneu27	Sneu28	Sneu26	Sneu27	Sneu28	Sneu26	Sneu27	Sneu28
	201.06	195.69	164.04	149.66	176.05	173.49	49.64	116.14	39.83
	197.60	202.37	179.61	133.54	147.47	136.79	63.87	91.90	46.91
	212.55	202.33	152.03	149.63	171.95	163.17	55.32	83.21	38.88
	194.07	213.52	183.61	165.28	169.34	150.22	74.96	80.52	43.68
	204.88	206.20	161.09	141.65	150.43	111.97	53.92	86.34	64.56
	198.71	192.44	165.31	135.74	191.66	112.83	70.91	117.71	56.99
	197.71	203.68	178.39	131.58	169.85	126.77	75.69	130.51	48.21
	199.06	210.94	213.75	141.67	187.73	131.26	68.77	117.73	59.94
	188.59	201.59	205.03	143.72	172.22	143.74	57.41	89.02	55.73
	188.38	205.87	218.05	154.35	173.64	124.66	70.35	113.21	92.63
	196.07	216.60	212.21	150.47	158.67	150.45	58.48	81.20	64.12
	201.68	191.80	191.98	134.44	168.35	136.51	66.37	102.99	50.17
Average	198.36	203.59	185.42	144.31	169.78	138.49	63.81	100.87	55.14

	Type IIc		Type I			Type IIb			
	4335	4410	4336	4335	4410	4336	4335	4410	4336
	216.65	191.95	228.44	137.53	154.18	150.35	43.77	28.75	80.80
	213.51	193.27	218.10	150.44	183.29	150.27	45.64	71.01	77.97
	222.67	179.28	171.85	146.23	157.75	190.77	42.03	23.18	38.31
	224.07	200.51	216.84	140.04	180.35	178.21	23.26	23.68	52.61
	210.07	193.50	213.95	151.65	163.29	166.83	38.86	65.08	38.54
	208.17	190.00	215.86	150.83	154.44	172.76	37.89	29.47	69.80
	215.25	168.00	235.75	154.12	169.04	161.53	34.80	26.70	44.32
	218.01	218.06	236.32	156.79	153.70	165.50	44.31	51.47	67.09
	212.08	190.96	228.64	168.73	181.95	156.63	45.51	65.79	55.54
	215.25	192.73	219.54	147.89	153.98	173.64	59.48	48.25	31.33
	205.76	215.12	207.19	137.62	168.35	162.77	64.01	82.19	96.02
	199.41	205.48	225.76	135.02	199.28	166.21	27.13	85.23	58.07
Average	213.41	194.90	218.19	148.07	168.30	166.29	42.22	50.07	59.20

Appendix C | NBTx Protocol

NBTx Protocol

Marie-Lune Simard

Research Group Stewart, Genome Evolution and Aging

Created on June 2017

Material

1. Sodium succinate dibasic hexahydrate (Sigma S2378, 100 g)
2. Phenazine methosulfate (Sigma P9625, 500 mg)
3. Nitrotetrazolium Blue chloride (Sigma N6876, 500 mg)
4. Sodium azide (Sigma 71289, 50 g)
5. Sodium dihydrogen orthophosphate monohydrate (VWR 102454R)
6. Disodium hydrogen phosphate anhydrous(VWR 444423K)
7. 96 % Ethanol denatured with 1 % MEK(Appli-Chem A2551, 5 L)
8. 99 % Ethanol denatured with 1 % MEK (Appli-Chem A5007, 5 L)
9. Superfrost Plus microscope slides from Menzel (24x60 mm, 1.5, VWR 631-0853)
10. Xylene (Appli-Chem A2476, 5 L)
11. Cytoseal (Thermo Scientific 8312-4)
12. Cooling and heating incubator

Reagents Preparation and Storage

Phosphate Buffer 0.1M pH 7.0

1. Solution A: dissolve 15.6 g sodium dihydrogen orthophosphate in 500 ml deionized water
2. Solution B: dissolve 28.3 g disodium hydrogen phosphate in 1 L deionized water
3. Mix 390 ml solution A to 610 ml solution B
4. Adjust to pH 7.0
5. Make up to 2 L with deionized water

6. Aliquot into 50 ml Falcon tubes
7. Store at -20 °C

Phenazine methosulfate (PMS, 2.0 mM)

PMS solutions should be prepared in deionized water. Solutions in water are stable and decomposition of solutions with formation of pyocyanine and other products can be avoided. PMS is also very sensitive to light exposure and as such should be stored in a dark area.

1. Dissolve 6.12 mg PMS in 10 ml deionized water
2. Aliquot 410 µl into 0.5 ml tubes
3. Store at -20 °C in a light protected area

Nitroblue tetrazolium chloride (NBT)

NBT solution is prepared fresh. Non-enzymatic formation of formazan crystals can form over time in solution. To avoid this, we prepare aliquots of 5 mg of NBT powder in Eppendorf tubes which we dilute in PBS when needed. 3.2ml of 0.1 M PBS is added to 5 mg NBT (1.875 mM final concentration).

Sodium succinate (1.3 M)

1. Dissolve 3.5 g in 10 ml 0.1 M phosphate buffer, pH 7.0.
2. Aliquot 410 µl into 0.5 ml microtubes.
3. Store at -20 °C.

Sodium azide (100 mM)

1. Dissolve 32.5 mg sodium azide in 5 ml 0.1 M phosphate buffer, pH 7.0.
2. Aliquot 100 µl into 0.2 ml microtubes
3. Store at -20 °C.

Establishing Staining Conditions

Before getting started, determining proper staining conditions is essential. Ideally, temperature and incubation time are optimized to obtain both colorless tissues from wild-type animals AND a strong and rapid deposition of blue formazan crystals when blocking complex IV with either sodium azide or potassium cyanide. When these two conditions are met, unspecific staining in healthy mitochondria is avoided and sensitive detection of low levels of complex IV deficiency is possible. Because mitochondrial enzymatic activity varies between species and organs, it is important to set up staining conditions that are valid for the tissue which is to be evaluated.

1. Choose incubation temperature (see Table 1 for guidelines)

Caution: dissolved oxygen in the incubation solution is limited and quickly depleted when mitochondrial activity is increased at high temperatures. Lack of oxygen will cause the reduction of NBT in healthy tissues.

2. Incubate healthy tissues from young animals (e.g. 12 weeks' old mice) for 15, 30, 45 and 60 minutes in NBTx solution (see *Basic Protocol* below). Note if or when tissue appears blue.

3. Adjust temperature so that tissue remains clear, preferentially even after 60 minutes.

Troubleshooting: If tissue does not remain clear, consider the following aspects: Tissue thickness (7 to 12 μm are recommended), relative humidity in incubation chamber (below 50%), slide should not be covered (remove lid), temperature.

4. Test formazan deposition with 1 mM sodium azide (or potassium cyanide). Add 10 μl of sodium azide stock solution (see section: *Reagents Preparation and Storage*) to 1 ml NBTx solution. Incubate for 30 minutes at desired temperature.

Note: If, in the presence of 1 mM sodium azide, formazan deposition after 30 minutes is weak, small changes in complex IV oxidative activity in affected tissues might not be detectable. Consider changing parameters.

Basic Protocol

1. Cut frozen tissue onto Superfrost plus microscope slides. Let sections thaw briefly to stick to the slide then store at -20 °C or -80 °C for long term storage. Section thickness can be adjusted to fit the tissue at hand (see section: *Establishing Staining Conditions*).

Caution: storing tissue sections will reduce mitochondrial enzymatic activity over time.

2. Preincubate sections 10 minutes in 0.1 M PBS at the desired temperature.

Note: see *Establishing Staining Conditions* section to determine temperature.

3. Prepare fresh NBT solution by adding 3.2 ml PBS to 5 mg NBT powder. Calculate 1 ml NBTx solution per slide.

Caution: reducing the volume of solution covering tissue sections might increase unspecific formazan catalysis.

4. Rapidly thaw 0.4 ml 1.3 M sodium succinate and 0.4 ml 2.0 mM phenazine methosulphate. Mix to 3.2 ml NBT solution.
5. Remove PBS by tipping slides on a piece of paper and add 1 ml NBTx solution to each slide.
6. Incubate for 30 minutes or according to your established staining conditions.
7. Wash in purified water for 2 to 5 minutes.
8. Dehydrate tissue through a series of increasing concentrations of ethanol (e.g. 50 %, 70 %, 96 %, 100 %, 100 %), allowing at least 5 minutes in the final 100 % ethanol.

Note: A reddish color, which is attributed to a semi-reduced form of NBT, is ethanol soluble and should be washed away easily in the final ethanol steps. Blue formazan is ethanol insoluble(Itoh et al. 1996; Bertoni-Freddari et al. 2004; Navarro et al. 2002).

9. Proceed to two changes, 5 minutes each, in 100 % xylene.
10. Mount with Cytoseal.

Figures and Tables

Table 1: Staining Guidelines

	Section Thickness (μm)	Temperature (°C)	Time (minutes)
Human			
Heart	7 to 10	37	20-30
Skeletal muscle	7 to 10	37	30-45
Colon	7 to 10	37	30-45
Mus musculus (C57BL/6N)			
Heart	7 to 12	18 to 25	30
Brain	10 to 16	25	30
Skeletal muscle	10 to 16	18 to 25	30
Testis	10 to 16	25	30
Drosophila melanogaster			
Thorax muscle	7 to 10	18 to 25	10

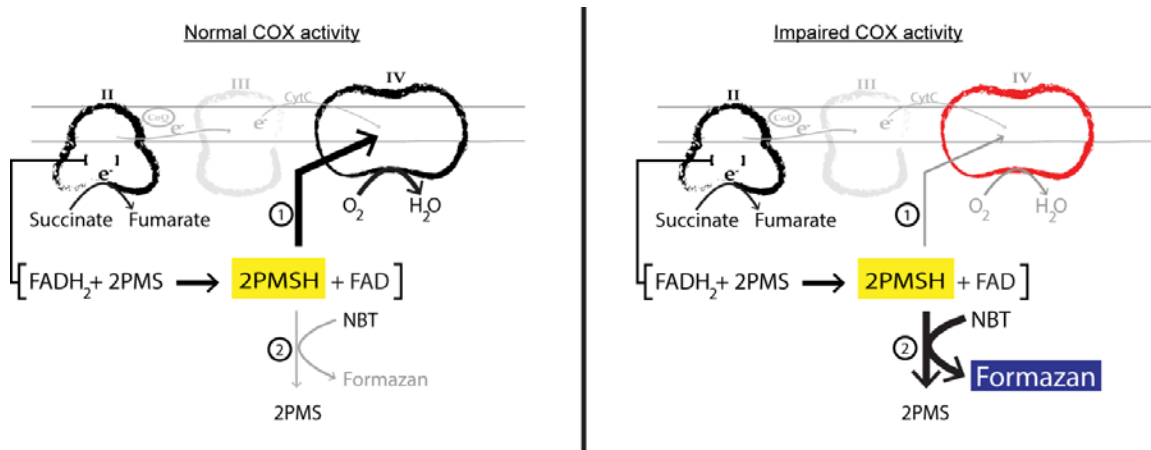


Figure 1: Schema of the NBTx's biochemical reactions. Succinate is used to engage the activity of Complex II. Phenazine methosulfate (PMS) acts as an intermediate electron carrier between Complex II and either Complex IV or tetrazolium salts (NBT).

Erklärung

Ich versichere, dass ich die von mir vorgelegte Dissertation selbständig angefertigt, die benutzten Quellen und Hilfsmittel vollständig angegeben und die Stellen der Arbeit – einschließlich Tabellen, Karten und Abbildungen –, die anderen Werken im Wortlaut oder dem Sinn nach entnommen sind, in jedem Einzelfall als Entlehnung kenntlich gemacht habe; dass diese Dissertation noch keiner anderen Fakultät oder Universität zur Prüfung vorgelegen hat; dass sie – abgesehen von unten angegebenen Teilpublikationen – noch nicht veröffentlicht worden ist sowie, dass ich eine solche Veröffentlichung vor Abschluss des Promotionsverfahrens nicht vornehmen werde. Die Bestimmungen der Promotionsordnung sind mir bekannt. Die von mir vorgelegte Dissertation ist von Prof. Dr. Jan Riemer betreut worden.

Marie-Lune Simard
Köln, Sept. 2018

